Nanodiamond Imaging: a New Molecular Imaging Approach

Alex Hegyi

Electrical Engineering and Computer Sciences
University of California at Berkeley

Technical Report No. UCB/EECS-2013-84
http://www.eecs.berkeley.edu/Pubs/TechRpts/2013/EECS-2013-84.html

May 16, 2013

Nanodiamond Imaging: a New Molecular Imaging Approach

by

Alex Nathan Hegyi

A dissertation submitted in partial satisfaction of the

requirements for the degree of

Doctor of Philosophy

in

Engineering – Electrical Engineering and Computer Sciences

in the

Graduate Division

of the

University of California, Berkeley

Committee in charge:

Professor Eli Yablonovitch, Chair
Professor Steven Conolly
Professor Michael Lustig
Professor Dmitry Budker

Spring 2013

Nanodiamond Imaging: a New Molecular Imaging Approach

by

Alex Nathan Hegyi

Abstract

Nanodiamond Imaging: a New Molecular Imaging Approach

by

Alex Nathan Hegyi

Doctor of Philosophy in Engineering – Electrical Engineering and Computer Sciences

University of California, Berkeley

Professor Eli Yablonovitch, Chair

Nanodiamond imaging is a novel biomedical imaging technique that non-invasively records the distribution of biologically-tagged nanodiamonds in vivo, in two or three dimensions. A nanodiamond imaging system optically detects electron spin resonance of nitrogen-vacancy centers in nanodiamonds, a non-toxic nanomaterial that is easily biologically functionalized. Two systems were built to demonstrate the feasibility of the technique. Using the first system, we imaged 2D projections of multiple nanodiamond targets within pieces of chicken breast; it is the first demonstration of imaging within scattering tissue by optically-detected magnetic resonance. The first system achieves a sensitivity equivalent to 740 pg of nanodiamond in 100 s of measurement time with a spatial resolution of 800 μm over a 1 cm^2 field of view. The second system was built with a field of view large enough to image a mouse, and with the capability to acquire multiple 2D projections of the subject for 3D reconstruction of the nanodiamond distribution.

In this thesis, we briefly review existing imaging modalities. We show how nanodiamond imaging has the potential to image with both high sensitivity AND high spatial resolution over organism-scale fields of view, features which are mutually exclusive in existing modalities (except at the shallowest imaging depths). Nanodiamond imaging's combination of high sensitivity and high resolution is potentially one of its greatest advantages. With reasonable sensitivity increases we expect to achieve a sensitivity of 100 fg and potentially as low as 25 ag; spatial resolution could reasonably be extended to <100 μm and is only limited by the strength of the magnetic gradient. We discuss practical ways to achieve these sensitivity increases, including various different modulation schemes.

We also review the nitrogen-vacancy center and its optically-induced spin polarization and optical spin detection mechanisms starting from a group-theoretic understanding of its energy levels. We build upon knowledge of the nitrogen-vacancy center, starting from its spin Hamiltonian, to present a model of the optically-detected magnetic resonance lineshape of nitrogen-vacancy centers in nanodiamond powder. This model is compared to measurements. We explore the

imaging point-spread function and show how imaging at just above the NV zero-field frequency—2.872 GHz, rather than 2.869 GHz—improves the contrast.

Details of the imaging systems are discussed, including the stable source of optical excitation provided by band-pass–filtered LEDs, and the sensitive optical detection provided by custom-built photodiode amplifiers that were shielded to reject microwave interference. Other detailed subsystems designed and constructed for these imaging systems include electromagnet coils and multichannel bipolar magnet power supplies, and software for experiment control and signal processing.

"So, the thing I would say is, when you grow up, you tend to get told that the world is the way it is and your, your life is just to live your life inside the world, try not to bash into the walls too much, try to have a nice family life, have fun, save a little money… but life, that's a very limited life. Life can be much broader, once you discover one simple fact, and that is everything around you that you call life was made up by people that were no smarter than you. And you can change it, you can influence it, you can, you can build your own things that other people can use. And the minute that you understand that you can poke life and actually something will, you know if you push in, something will pop out the other side, that you can, you can change it, you can mold it, that's maybe the most important thing… is to shake off this erroneous notion that life is there and you're just gonna live in it, versus embrace it, change it, improve it, make your mark upon it.

I think that's very important and however you learn that, once you learn it, you'll want to change life and make it better, cause it's kind of messed up, in a lot of ways.

Once you learn that, you'll never be the same again."

—Steve Jobs, NeXT Computer, 1995

Table of Contents

List of Figures

List of Tables

List of Symbols

c	speed of light (m s^{-1})
g	Landé g-factor (dimensionless)
$\hbar$	Planck's constant/2π (J s)
k	Boltzmann's constant (J K^{-1})
m_s	$\hat{z}$-axis spin projection of NV
γ	gyromagnetic ratio (rad s^{-1} T^{-1})
λ	optical wavelength (m)
μ_B	Bohr magneton (J T^{-1})
σ	optical absorption cross-section (m^2)
$\sigma_{1,2,3,N}$	basis orbitals of NV
$\sigma_{d,e,f}$	reflection operators in C_{3v}
$\chi^{\mu}(\boldsymbol{R})$	character of the operation $\boldsymbol{R}$ in the representation μ
ω	microwave frequency (rad s^{-1})
ω_0, ω_i	microwave transition frequencies (rad s^{-1})
${}^3A_2$	NV triplet ground state
$\boldsymbol{B}$	magnetic field (T)
$\boldsymbol{B}_0$	static magnetic field (T)
$\boldsymbol{B}_1$	microwave magnetic field (T)
$C_3^{\pm}$	rotation operators in C_{3v} (±120°)
D	zero-field splitting (J)
${}^3E$	NV triplet excited state
E	zero-field strain splitting (J)
E	identity operator in C_{3v}
G	magnetic field gradient (T m^{-1})
$\boldsymbol{H}$	Hamiltonian (J)
I	optical intensity (W m^{-2})
$\boldsymbol{O}_{\boldsymbol{R}}$	group operation $\boldsymbol{R}$ with respect to a particular basis
$\boldsymbol{P}^{\mu}$	projection operator onto representation μ
T	absolute temperature (K)
T_1	spin-lattice relaxation time (s)
T_2	spin-spin relaxation time (s)
$\boldsymbol{R}$	arbitrary group operation
$\boldsymbol{S}$	vector of Pauli spin operators (dimensionless)
Γ	linewidth (rad s^{-1})
Φ	magnetic scalar potential (T m)
Ω, Ω_i	Rabi frequency (rad s^{-1})

Preface

In academic work, it is rare that one comes across a description of how an idea took shape; rather, only the polished results are shown. When I first started out in research and in the technical world, it was overwhelming to be shown so many "finished" results without seeing the far larger numbers of false starts and failed ideas that accrued along the way to obtaining significant results. This bias toward only sharing finished results built an expectation within me that there should be a linear trajectory between initiating a research project and producing results. Without an appreciation of what actually takes place in between, the cognitive dissonance between your lived experience and the expectation of such a linear trajectory can be highly discouraging. Thus, to my potential readers, especially if you are just starting out, know that every idea goes through many changes as it takes shape, and most of these changes are prompted by what seem like failures in the moment but are actually valuable learning experiences. You learn about what does *not* work simply by trying it. To elucidate my own path from the start of graduate school to the completion of my thesis, and because I often get asked about how I came up with the idea, I would like to preface my thesis with a description of the genesis of nanodiamond imaging.

Nanodiamond imaging started out when I was first introduced to the nitrogen-vacancy center (NV) through work I was doing in quantum computation/communication. My advisor's idea was to communicate quantum information over electrical wires from NV to NV by using a transmission line resonator. After going through many rounds of calculation it became clear that even with a resonator that was optimized for magnetic coupling by lowering its ratio of inductance to capacitance, this idea would not work. The reason was the magnetic coupling between the resonator and the NV was too weak. (Note, however, that it would work for coupling to qubits with a sizeable electric dipole moment, assuming the resonator was optimized for electric coupling by increasing its inductance to capacitance ratio.)

Around that time, there was much interest in using the NV as a nanoscale, high sensitivity and high resolution magnetometer, and several papers, notably [1] and [2], proposed the idea. These papers suggested using the NV to perform nanoscale MRI of protein molecules *in vivo*. I was immediately hooked by the prospect of imaging and understanding protein structure within a living environment rather than within the artificial environment of a cryogenically frozen crystal. Not knowing where to start, I purchased lab equipment to build a confocal microscope and perform optically-detected magnetic resonance experiments on single NV centers. This occurred during the summer of my first year and into my second year as a PhD student.

During my second year, I attended the 2010 American Society of Mechanical Engineers' NanoEngineering in Medicine and Biology conference. A central theme of the conference was the use of detonation nanodiamond particles as a drug delivery platform, but people at the conference did not seem to be aware of NVs. I realized I could both differentiate myself from existing work with NVs and also leverage the work being done with nanodiamond in a medical context by doing something medically oriented with macroscopic ensembles of NV-containing nanodiamonds. At this point, though, I still had no specific ideas in terms of a thesis project.

In the spring of 2010, I took a graduate-level course on the Fundamentals of Magnetic Resonance Imaging. It was through this course, taught by Prof. Lustig, that I finally understood the details of how magnetic resonance is used to image in a medical context. What especially fascinated me was how MRI performs a multiplexed measurement that takes place in Fourier space (rather than position space) by clever application of magnetic gradients. My fundamental insight for nanodiamond imaging came in the summer of 2010 when I realized I could perform an optically-detected version of (functional) MRI by incorporating NVs into nanodiamonds and using the nanodiamonds as a tracer.

At first, I focused on small fields of view for high resolution imaging within a cell, before realizing that I should not be competing with super-resolution imaging and other forms of optical microscopy. With small fields of view the microwave power could be made high enough to perform the same kinds of coherent pulse sequences used in MRI, but as will be explained in this thesis, the move to organism-scale imaging and the lower microwave intensities meant that new imaging schemes needed to be developed that used only incoherent microwave pulsing. During the summer of 2010, I wrote up and submitted an invention disclosure based on this initial conception of nanodiamond imaging, which at the time I called optical magnetic resonance imaging. My advisor and I also started talking with GE Global Research in hopes of collaboration, given GE's expertise with diamond and with MRI.

What came next was rather misguided, but is a perfect example of how easy it is to go down a less than optimal path, something that becomes clear only in hindsight. I thought it would be instructive to develop a miniature version of optical MRI with a field of view big enough to image a single cell. I started to dream up how I could build such a device, complete with microfabricated magnetic gradient coils, in Berkeley's NanoLab. Thus, I had to become trained in the cleanroom, and while being trained I started generating different designs. It quickly became clear that I needed to start with the simplest device possible, so I stripped the gradient coils from the design and fabricated a coplanar stripline, a kind of waveguide I could integrate with my existing confocal microscopy setup to perform optically-detected magnetic resonance (ODMR) experiments on NV-containing nanodiamonds.

One problem was that I did not have any NV-containing nanodiamonds. My plan to remedy this, which I spent several months on, was to apply a drop of

nanodiamonds onto the chip containing the coplanar stripline, and then bring the chip to LBL for assistance in ion implantation and annealing of the nanodiamonds to form NVs. However, the chip was made out of titanium on silicon, and at the time I was not aware that the nanodiamonds could dissolve in the titanium and form titanium carbide. So, I made new coplanar striplines, this time out of tungsten on quartz. Even with these new striplines, we were never able to find signs of NVs in the nanodiamonds that we implanted. Finally fed up with frustration, I looked around for other sources of NV-containing nanodiamonds and was able to obtain them from Prof. Huan-Cheng Chang of the Academia Sinica in Taiwan.

One of the things I hoped to use the coplanar stripline for was to understand what the ODMR lineshape of NVs in nanodiamond powder looked like. This was something I potentially could have calculated in advance, although it became much clearer how to calculate it once I saw the data. Had I had a source of NV-containing nanodiamonds to begin with, I would have never had to spend several months doing cleanroom work—part of the reason to fabricate a chip was to have something that could act as a support for the nanodiamonds while they were implanted and annealed. I ended up simply depositing a drop of the nanodiamonds onto a bond wire and mounting the wire in front of the objective of my confocal microscope. From this I learned that one should try to buy as much stuff as possible, and simplify the experiment as much as possible from the start, potentially calculating beforehand any expected results.

In the spring of 2011, armed with my data, I went through some calculations and realized that an imaging technique using NV-containing nanodiamonds had enough sensitivity to be on the verge of working. My advisor told me it was not enough to invent a new imaging technique and claim it would work; you actually have to build and demonstrate a system! My feeling of being overwhelmed was quickly superseded by excitement over finally being able to build something! Most of the time spent building was directed toward the magnetics, both winding my own coils and developing many iterations of my own control circuitry. I learned a lot from this experience, but if I had to repeat it (as I did when building my second imaging system), I would definitely have looked for off-the-shelf solutions (or contracted it out, as I did for the coils) from the start.

A final word of advice: since I was effectively building a tool, I would have gotten the potential users (researchers, clinicians) involved from the beginning.

Acknowledgements

There are many people I would like to thank for their support of my education and of my thesis project—without them my graduate work would not have been possible. First and foremost, I am indebted with gratitude to the Fannie and John Hertz Foundation, both for funding and support. I held a P. Michael Farmwald Fannie and John Hertz Foundation Fellowship which provided me with my tuition and stipend during the tenure of my graduate studies, and which enabled me to carry out a research project independent of existing research programs. I would therefore also like to express my gratitude to Mike Farmwald, whose generosity was an enabling factor in this particular Fellowship.

My gratitude for the support received from the Hertz Foundation simply cannot be overstated, and I know my membership within the Hertz community will reap dividends for years to come. I would therefore like to give thanks to all the other Hertz fellows, current and former, all the board members, and all the extraordinarily helpful and supportive staff at the Hertz Foundation, for facilitating such an amazing community (especially Tom Weaver, whose yearly check-ins provided a welcome source of encouragement). I hope I will be able to contribute to this community in increasingly substantial ways. I would especially like to thank one member of the Hertz community, Louis Lerman, for his tireless efforts in community-building among Hertzies and for his personal and direct involvement in maximizing my potential and my professional well-being.

Next, I would like to thank my advisor, Prof. Eli Yablonovitch, for being a strong ally from the beginning, believing in me unfailingly, providing me with encouragement when I doubted myself, and aligning with the mission of the Hertz Fellowship to provide me unrestricted freedom in my research. Eli is someone who "gets" me in the sense of my desire to work on applied problems without regard to using specific methods. He has a broad, interdisciplinary background predicated on a solid physical understanding; he is also a firmly independent thinker. He has been a great guide in terms of helping me think strategically and helping me take charge of my own destiny.

Then, there are those that prepared me for graduate school. These include my former teachers and professors as well as other mentors and recommendation writers. Daniel Abrams has been a great mentor and friend over the years from the time I first got to know him while working at Luminescent (incidentally co-founded by Daniel and Eli). The scientists I worked with at PARC, who all contributed to my recommendation letters—Michael Bassler, Peter Kiesel, and Noble Johnson—showed me how much fun it can be and how productive one can be when working with a team of positive, supportive people. It is because of my experience at PARC that I considered pursuing a PhD. I would like to thank Prof. Aharon Kapitulnik,

who was one of my professors and recommendation writers. I would also like to thank Prof. Yoshihisa Yamamoto, who hosted me in his lab as an undergraduate researcher and wrote one of my recommendations. Many thanks to David Press, who was my graduate student mentor in Prof. Yamamoto's lab, and who introduced me to experimental optics and cryogenics. Also, Prof. Brad Orr hosted me for a summer at the University of Michigan, so I'd like to thank him (and Bonnie Ludwig) for the opportunity. Bonnie Ludwig was my graduate student mentor at that time and taught me about professionalism within the sciences. Finally, I'd like to thank Prof. Jelena Vuckovic, whose class at Stanford on Nanophotonics and Nanostructures inspired me down my academic path (and also introduced me to Eli's work on photonic crystals, a subject which instantly captured my imagination).

There are those who offered invaluable scientific support during graduate school as well, such as the other members of my qualifying exam and thesis committee—Profs. Steven Conolly, Michael Lustig, and Dmitry Budker. I would especially like to thank Steven and Miki for regular stimulating discussions and for their friendship and support. I learned a lot and was inspired by discussions with Patrick Goodwill, a research staff member in Prof. Conolly's group. Victor Acosta, a former graduate student of Prof. Budker's, was very helpful to me when I was first setting up a lab to investigate nitrogen-vacancy centers, and he assisted me in determining what kind of equipment to buy. Thomas Schenkel at LBNL was very generous in offering his and his students' time in helping me try to implant nitrogen-vacancy centers into nanodiamonds, and while we never could get it to work, I'd like to thank Julian Schwartz for the effort. I'd also like to thank Christoph Weis for generally helping me out with stuff related to diamond and nitrogen-vacancy centers. I ended up obtaining fluorescent nanodiamond from Prof. Huan-Cheng Chang, so I'd like to thank him for his collegiality in providing me the nanodiamonds and also corresponding with me in regard to how to functionalize nanodiamonds. I'd like to thank Prof. Jeronimo Maze, whose work (and brief correspondence with me) helped me to understand the group theoretical description of the nitrogen-vacancy center. I'd like to thank Ed Marti, a student in Physics and also a Hertz Fellow, for many enjoyable discussions regarding theoretical and experimental AMO physics that proved fruitful in building my electromagnet amplifiers. I'd like to thank the other members of the Yablonovitch group with whom I overlapped, and whose curiosity and questions about my project always provided me with new things to think about. Each member brought their own unique perspectives and insights to the group, and it was fascinating to see how everyone's individual projects have developed over the years. Finally, I'd like to thank everyone who has mentored or inspired me over the years, and I'm sorry if I've accidentally left anyone out.

In closing, none of this would have been possible without the love and support of family and friends. I dedicate this thesis to my parents, Michelle and Dennis, for their unconditional love, support, and guidance; I would also like to thank my brother, Aron, for being supportive of me. I have the added bonus of my

father being a Professor Emeritus in Physics, and I can trace my interest in physics back to him coaxing my curiosity at a young age. He would patiently answer my questions about the world in terms that I could understand, at just the appropriate level, without overwhelming me with too much information such that I turned away from the sciences. His breadth of knowledge in experimental physics was a great resource for me during my PhD, but more often than not it was his ability to get me to slow down and approach problems one step at a time that would allow me to get unstuck at critical points. He also provided invaluable guidance in reviewing my writing and helping me to communicate in the clearest, most succinct way possible.

Chapter 1: Introduction

Chapter Summary

In this first chapter, we start by describing existing biomedical imaging techniques as a way to provide a context for nanodiamond imaging. Next, we introduce the features that make nanodiamonds and the nitrogen-vacancy center (NV) special, and we discuss the existing state of the art in terms of biological applications of NVs in diamond. We then introduce nanodiamond imaging. We wrap up the chapter with a discussion of the original contributions described in this thesis and an outline of the rest of the thesis.

Molecular Imaging

For the purposes of this thesis, existing biomedical imaging techniques can be broken down according to two different classes: *anatomical* techniques, such as magnetic resonance imaging, X-ray/X-ray computed tomography (CT), and ultrasound, and *molecular* techniques, such as positron emission tomography (PET), single-photon emission computed tomography (SPECT), and fluorescence optical imaging. The chief difference between anatomical and molecular techniques is anatomical techniques have higher spatial resolution than molecular techniques, while molecular techniques have much higher sensitivity and specificity to image subtle biochemical variations within an organism, though at significantly lower spatial resolutions. (For a good comparison of existing imaging techniques, consult Table 1 of Ref. [3].)

A prototypical example of the difference between the two classes of techniques is illustrated in Fig. 1.1. Here, the top row (A and D) illustrates one of the most well known anatomical imaging techniques, that of the X-ray photograph. High-energy photons, in the form of X-rays, are passed through an organism and preferentially absorbed in areas with higher electron density. The X-rays that make it through the organism strike a photographic plate; thus, an image is formed with variations in contrast dependendent on a two-dimensional projection of tissue density. Given that there is not much scattering and that the X-ray wavelength is very short relative to the size of the features involved, the resolution can be very high. However, X-ray imaging is not sensitive to subtle biochemical variations.

The middle row of Fig. 1.1 is a near-infrared (NIR) fluorescence image taken of the same mouse after injection with an NIR dye. It is easy to detect small quantities of dye, so this kind of fluorescence imaging is very sensitive. By attaching antibodies or other bioactive molecules to the dye, it is possible to perform "functional" imaging, i.e., imaging of the biochemical variations that provide insight into some physiological function. However, because tissue is typically highly scattering, the NIR photons scatter as they leave the organism, dissipating

information about their origin as they reach the detector. This scattering causes fluorescence molecular imaging to have poor spatial resolution.

In the bottom row of Fig. 1.1, the anatomical and molecular images of the top two rows are co-registered and overlaid. The anatomical image provides the viewer with enough anatomical context to understand that the dye has concentrated in the mouse's bladder and kidneys.

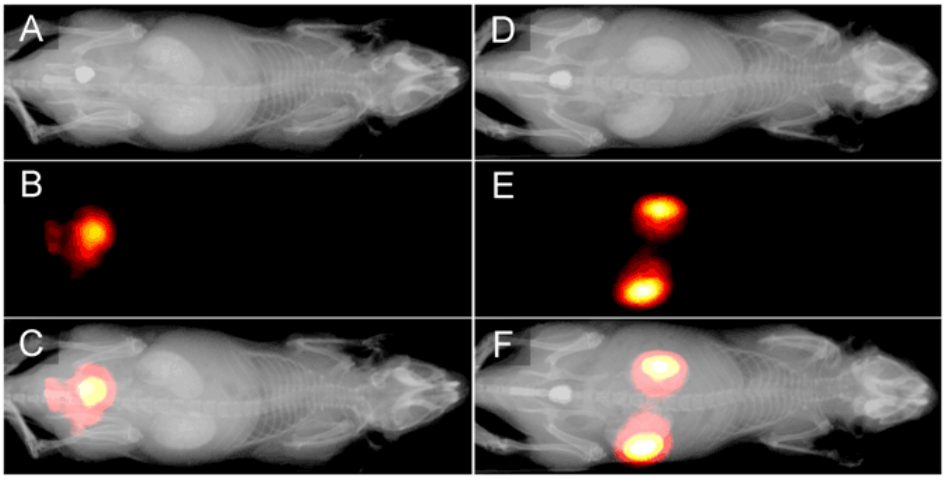

Figure 1.1: Comparison of anatomical and molecular imaging. Top row: X-ray photograph of mouse. Middle row: near-infrared fluorescence image. Bottom row: top two rows co-registered in software. Note that the dye has migrated to the kidneys and bladder. Image taken from [4].

Molecular imaging in particular refers to a class of noninvasive biomedical imaging techniques with the sensitivity and specificity to image biochemical variations *in vivo* [3]. Molecular imaging modalities typically rely on the use of a contrast agent that highlights a particular biochemical variation and is sensitively detected by an imaging system. Even those imaging techniques that fall into the "anatomical" category can perform molecular imaging, though at reduced sensitivity compared to the "molecular" techniques, with the use of an imaging agent: for example, iodine in CT, and gadolinium in MRI.

We now briefly review qualitative features of the different kinds of biomedical imaging techniques mentioned here. A comparison of the more established techniques to nanodiamond imaging in terms of resolution, sensitivity, and cost is presented in Chapter 5: Discussion. Quantitative information pertaining to these and other factors is available in the references (and the references therein) following Fig. 5.7, under the heading "Comparing to existing techniques".

X-ray Computed Tomography

X-ray computed tomography, or CT, refers to the process of taking multiple X-ray photographs around a sample, and reconstructing the photographs into a 3D model of the density of the sample using a tomographic reconstruction algorithm. The upsides of the technique include the high spatial resolution and the ability to scale the resolution down for small sample sizes, in what is known as micro-CT. The penetration depth is also reasonably high. Unfortunately, CT-based imaging exams impart a large radiation dosage to the subject. They also suffer from lower sensitivity.

Magnetic Resonance Imaging

Magnetic resonance imaging, or MRI, takes advantage of the slight magnetization of nuclear spins that occurs when a subject is placed inside a strong magnetic field. These nuclear spins can be excited with radio-frequency energy, and they precess about the strong magnetic field, inducing a voltage in a nearby pickup coil that is proportional to the net sample magnetization (typically, the receiver is tuned to the proton precession frequency). By placing the subject in a magnetic field gradient, protons at one side of the sample rotate faster relative to protons on the other side, introducing a spatially-varying periodic phase in the magnetization. This is equivalent to measuring the proton density at different points in reciprocal, or Fourier, space. One can thus image the proton density in real space by manipulating magnetic gradients and obtaining data in Fourier space, and then performing an inverse Fourier transform on the data.

One of the upsides of MRI is that it is possible to generate contrast based on many different mechanisms. For example, rather than just proton (or nuclear spin) density, it is possible to come up with pulse sequences that measure spin relaxation and spin coherence lifetimes, and even ones that are velocity-selective and that can locally measure the diffusion tensor (for example to map out connectivity networks in the brain). It is also possible to obtain spectroscopic information due to the presence of nuclei with different gyromagnetic ratios. Other advantages of MRI include its high spatial resolution and penetration depth—DC and RF magnetic fields easily penetrate tissue. Unfortunately, MRI scanners are very large and expensive, primarily due to the always-on superconducting magnet that is required to generate the 1.5 T (or higher) magnetic fields with part per million field homogeneity. Also, MRI is not very sensitive to detecting biochemical differences with contrast agents.

Ultrasound Imaging

Ultrasound imaging is a fairly straightforward imaging technique that takes advantage of the reflection of sound waves at acoustic impedance boundaries. An ultrasonic pulse is sent into a sample, and an array of detectors observes the reflections that propagate from the various impedance boundaries (presumably corresponding to physical or anatomical structures under investigation). Ultrasound is simple to use; it is low cost, and it acquires images quickly. It is fairly

high resolution, although the depth penetration is not as good as MRI or CT, due to the attenuation of sound within the tissue. It is also not easy to generate contrast with ultrasound except with microbubbles or similar structures that provide a sharp acoustic boundary.

Positron Emission Tomography

Positron emission tomography, or PET, relies on positron-emitting contrast agents to generate a signal. Positrons generated by these contrast agents travel a short distance and then are annihilated upon contact with electrons. Each positron/electron annihilation event creates two oppositely-directed gamma rays at 511 keV, and coincident (simultaneous) detection events are recorded by a ring of gamma ray detectors around the subject. By drawing lines between the coincident detection events and looking at where they intersect, it is possible to build up an estimate of the distribution of contrast agent within the subject. Since it is possible to detect single gamma rays, and since tissue is almost transparent to gamma rays, PET is a very high sensitivity imaging technique with significant depth penetration.

Unfortunately, the resolution of PET is limited by many factors. For example, the limited allowable dose of radioactivity to the patient necessitates large area detectors to maintain SNR, thereby introducing uncertainty into the location of the positron annihilation events. A larger number of smaller detectors could be employed to maintain detector area while increasing spatial precision, but this approach quickly becomes cost prohibitive as the cost scales with the number of detectors. Also, the chemistry of working with positron emitters is difficult. The most typical compound is a fluorinated version of glucose, made with the positron emitter ^{18}F (i.e., ^{18}F-fluorodeoxyglucose). Positron emitters are relatively short-lived, so the ability to perform longitudinal imaging studies is strictly constrained. The short half-life also contributes to the high cost, because a cyclotron is required next to the imaging facility to produce the compounds. Also, the radiation dose is significant.

Single Photon Emission Computed Tomography

Single photon emission computed tomography, or SPECT, is another very sensitive imaging technique that relies on the detection of individual gamma rays. Rather than using positron emitters, SPECT detects gamma rays directly from gamma-ray-emitting compounds. The gamma rays are detected by gamma cameras that rotate around the sample; a reconstruction can be built similar to how it is done with X-ray CT. Since direct gamma ray emitters have longer half-lives than positron emitters, SPECT is generally cheaper than PET because local production of the contrast agent is not required. However, the resolution is still poor, longitudinal imaging studies are constrained by radioactive decay times, and there is still an issue with radiation dose.

Fluorescence-based molecular imaging

Fluorescence-based molecular imaging has become a popular imaging technique primarily for *in vivo* small animal and preclinical studies. The stable nature of fluorescent dyes (relative to radioisotopes) allows longitudinal imaging. Fundamentally, the technology of this kind of imaging is simple; it requires a light source, a sensitive CCD camera, various optical filters to select excitation and emission wavelengths, and a light-tight enclosure. High sensitivity is achieved because it is possible to detect single photons; however, sensitivity is limited by tissue autofluorescence and by the shot noise of the autofluorescence. To overcome the issue of tissue autofluorescence background, bioluminescence imaging was developed. Bioluminescence imaging does not rely on an optical excitation source, so no autofluorescence is generated. Rather, it forms images of bioluminescence within an organism, generated by the expression of DNA incorporated into the subject that encodes a luminescent protein (such as firefly luciferase). Without the autofluorescence, bioluminescence imaging is even more sensitive than fluorescence imaging, but the drawback is necessary genetic engineering of the subject. For fluorescence and bioluminescence imaging, photon scatter causes poor depth penetration and poor spatial resolution. One can show that spatial resolution is on the order of the imaging depth, so imaging at 1 cm deep in tissue can be done at best with a lateral resolution of 1 cm. Furthermore, it is difficult to quantitate the amount of imaging agent present due to the unknown depth in tissue and the variable scattering and absorption coefficients of the tissue. An advantage of these techniques is their comparatively low cost and non-radioactive contrast agents.

Other techniques/Experimental

There are other experimental techniques that are emerging that attempt to combine high sensitivity with high spatial resolution. One of them is photoacoustic imaging (PAI) or photoacoustic computed tomography. PAI relies on the photoacoustic effect, which works by exciting the sample with a light source (such as a pulsed laser) and looking at the resultant thermoelastic expansion of the tissue with an ultrasonic detector. The amount of light absorption, and hence ultrasonic signal, varies locally with tissue characteristics such as the concentration of hemoglobin. PAI can thus form an image from these local tissue variations without the use of exogenous contrast agents.

Another emerging approach is X-ray luminescence computed tomography (XLCT) [5]. XLCT relies on nanoparticle phosphors as a contrast agent; these phosphors absorb X-rays and emit near-infrared light—both wavelengths of electromagnetic radiation that penetrate relatively deeply into tissue. By exciting the subject with a scanned X-ray pencil beam (a narrow beam for high resolution) and detecting the near-infrared luminescence (including the scattered photons, for high sensitivity), a three-dimensional picture of the nanoparticle phosphors can be built tomographically. In addition, anatomical information can be captured simultaneously with the use of a standard X-ray detector.

As seen from the discussion of existing and emerging molecular imaging modalities, each technique has particular strengths and weaknesses. An ideal molecular imaging technique would visualize a biochemical target according to a range of criteria, including high spatial and temporal resolution, high contrast relative to non-targeted tissues, depth-independent penetration into tissue, lack of harm to the organism under study, low cost, use of primarily endogenously-derived (naturally present) contrast mechanisms, and ability to multiplex signal sources into one image. Because no existing molecular imaging modality is ideal for all purposes, new imaging approaches are needed. Thus, in this thesis we propose a novel molecular imaging approach, called nanodiamond imaging, that uses nanodiamonds containing nitrogen-vacancy centers [6–8] as an imaging agent. As will be seen, nanodiamond imaging is somewhat of a cross between MRI and fluorescence imaging. This is because it takes advantage of optically-detected magnetic resonance of the NVs to combine the sensitivity advantage of optical detection with the spatial resolving power of magnetic resonance imaging techniques.

Nanodiamonds and the nitrogen-vacancy center

Diamond stands in a class on its own as an outstanding material. Among its most valued properties are its exceptional hardness, transparency, and high index of refraction; incidentally, these are all properties that contribute to its value as a gemstone. In addition, diamond is an excellent thermal conductor and a wide-bandgap semiconductor. Diamond is useful as an industrial material, especially in microparticle or nanoparticle form (for polishing, in cutting tools, as a lubricant, etc.) and nanodiamond can be readily obtained via a variety of synthesis techniques.

Different nanodiamond types are illustrated in Fig. 1.2. The top row of Fig. 1.2a shows a monocrystalline nanodiamond made by high-pressure-high-temperature synthesis, whereby a carbon precursor is compressed in a high-pressure chamber and heated to a high temperature. The bottom row shows a polycrystalline nanodiamond made by shock wave compression of graphite. Both particles are typically between 10 nm and 100 nm in size. In Fig. 1.2b, we see a single particle (top row) and agglomerated particles (bottom row) of detonation nanodiamond, synthesized by detonation of TNT and other explosives in a controlled atmosphere. Detonation synthesis of nanodiamond is a highly scalable approach to nanodiamond synthesis. Finally, the smallest known diamond-like carbon structures are called diamondoids, shown in Fig. 1.2c. Currently, there is no known synthesis route to making diamondoids; rather, they are fractionated from petroleum.

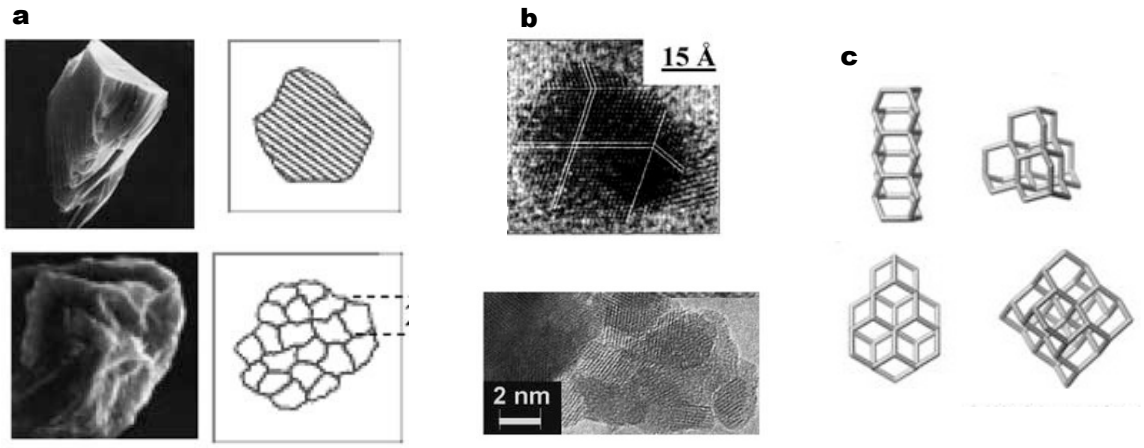

Figure 1.2: Nanodiamond particle types ordered from largest to smallest according to size of primary (*i.e.*, non-agglomerated) particle. **a**, Monocrystalline (top row) and polycrystalline (bottom row) nanodiamonds; sizes 10-100 nm. **b,** ultrananocrystalline diamond, <10 nm; single particle (top row), agglomerate (bottom row). **c,** diamondoid molecules. Adapted from [9].

Nanodiamonds have several promising features that could prove useful one day as a nanomaterial for biomedicine, and specifically as a contrast agent for biomedical imaging. Synthetic nanodiamond is low in cost, can be fabricated by several different methods including the ones described above, is non-toxic, and nanodiamond surfaces can be easily modified to attach to various biomolecules [9–13], providing a robust method of generating biological specificity. One possible method for biologically functionalizing nanodiamonds is shown below in Fig. 1.3. If a nanodiamond surface is carboxylated, which would occur for example after an oxidative acid treatment to remove outer graphitic layers, a nanodiamond-NHS ester can be formed by mixing with NHS (*N*-hydroxysuccinimide) in the presence of EDC (ethylcarbodiimide) [14].

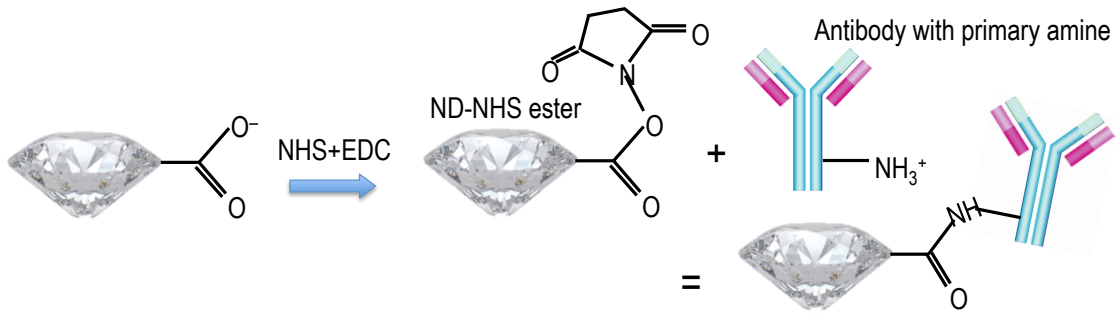

Figure 1.3: Bioconjugation of nanodiamond by carbodiimide chemistry. A nanodiamond that is functionalized with carboxyl groups (for example by oxidative acid treatment) can be attached to biological molecules containing primary amine groups such as in the amino acid lysine found in many proteins. The resulting amide bond is strong and stable.

Diamonds exhibit a variety of colors based on the inclusion of defects within the diamond lattice. The NV, a point defect consisting of a substitutional nitrogen with an adjacent vacancy, contributes to the pink color of some diamonds. The inclusion of NVs transforms our already useful nanodiamonds into sensitive optical and magnetic probes. By themselves, the optical properties of the NV are amenable to biological imaging. The fluorescence spectrum of the NV extends from ~630 nm to ~800 nm, peaking around 700 nm, and roughly matching the near-infrared window in biological tissue [15], as shown below in Fig. 1.4. The fluorescence has a high quantum yield, it is stable (i.e., doesn't bleach or blink), and occurs with a timescale ($\tau \approx 17$ ns, in nanodiamond [14]) significantly longer than biological autofluorescence lifetimes such that time-gating enhances the signal-to-noise ratio [16]. These characteristics have created interest in using NV-containing nanodiamonds as fluorescent probes for biology [14], [17], as a replacement for toxic quantum dots and bleachable organic dyes.

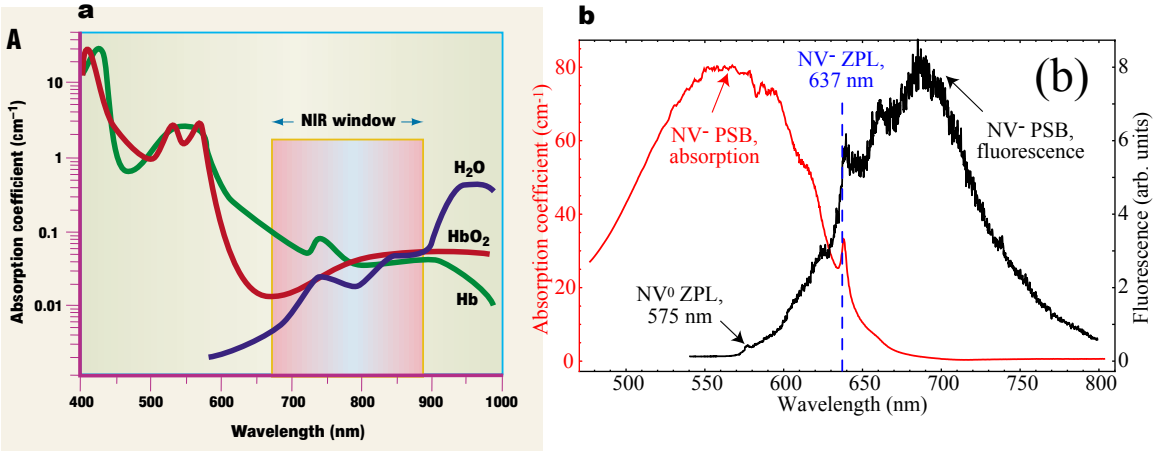

Figure 1.4: Near-infrared window and NV fluorescence spectrum. **a,** The near-infrared window in biological tissue spans from roughly 650 nm, where it is limited below by hemoglobin absorption, to 900 nm, where it is limited above by water absorption. **b,** The NV fluorescence spectrum (black) roughly overlaps with the near-infrared window. Panel **a** adapted from [18]; Panel **b** adapted from [19].

The high magnetic sensitivity of the NV is due to the diamond host. The NV's energy levels exist in the diamond bandgap, so the NV acts like an isolated atom, with a long spin relaxation and coherence time. Its unpaired electrons give rise to a triplet ground state, and because this state is weakly coupled to the diamond lattice, it has long spin relaxation (T_1) and spin coherence (T_2) lifetimes, leading to a narrow electron spin resonance (ESR) linewidth, even at room temperature (typical values for NV in nanodiamond might be T_1 = 1 ms and T_2 = 1 μs [20]). However, the significance of the NV is due to the interaction of its optical and magnetic properties: the spin state can be polarized and detected optically, even for a single NV at room temperature (notably, these features make the NV a prime qubit candidate for quantum computation [21], [22]). These properties arise because of an asymmetric intersystem crossing that causes a buildup of spin population within one spin sublevel upon optical cycling.

The narrow ESR linewidth provides high spatial resolution in a magnetic gradient, while the optical detection provides high measurement sensitivity; many have recognized the significance of this combination for biological applications. NV-based optically-detected ESR has high enough spatial resolution and sensitivity that nanodiamond magnetometers [1], [2] based on this principle have been proposed as detectors to perform nanoscale magnetic resonance imaging of biological molecules or probing of biologically relevant spins; recently, imaging the nanoscale magnetic field of a single electronic spin was demonstrated using an NV-based probe in ambient conditions [23]. In combination with the stable fluorescence, the spin properties of the NV allow high resolution localization and tracking of NV-nanodiamonds in live cells [24], [25]. Nanodiamond position can also be controlled

with nanometer precision in an aqueous environment using optical tweezers while ESR experiments are performed [26]. NVs show promise as monitors of real-time ion channel activity with millisecond time resolution by observing the NV decoherence [27], as well as sensitive, high spatial resolution wide-field imagers of both magnetic spin labels [28] and of high-speed neural function [29], [30]. When NV-nanodiamonds are used as fluorescent markers for microscopy, their fluorescence signal can be modulated via ESR for isolation from background autofluorescence [31].

However, what we are proposing with nanodiamond imaging—that is, imaging the nanodiamond concentration within the scattering tissue of macroscopic organisms via optically-detected magnetic resonance—differs significantly from existing work. The existing work has relied on microscopic fields of view to get high optical intensity in a focused laser spot and clear optical access to the NVs, and high intensity microwaves for coherent microwave pulses (i.e., Rabi nutation rate greater than the decoherence rate). Because we aim to illuminate a substantial fraction of an organism, we use much lower (by up to five orders of magnitude) optical intensity, and in addition use incoherent microwave excitation (i.e., at much lower excitation powers). To our knowledge, this is the first work that combines optical detection with magnetic resonance for imaging within scattering tissue, though a similar technique utilizing a non-resonant magnetic field effect, magnetofluorescence imaging [32], has been proposed.

Introduction to Nanodiamond Imaging

Many molecular imaging techniques make use of an imaging agent, or combination of a biological molecule that interacts with a particular target and a marker that is sensed by an imaging system. Nanodiamond imaging operates in this way, and it exploits a serendipitous combination of many physical properties of its NV-nanodiamond imaging agent that give it the best aspects of both imaging classes: the high specificity and sensitivity of molecular imaging, yet at the high spatial resolutions achievable with anatomical imaging.

An overview of nanodiamond imaging can be seen in Fig. 1.5. We start with a mouse that contains NV-nanodiamonds that have distributed themselves according to some physiological mechanism, and we wish to quantify that distribution *in vivo*. Because we are using spin-resonance and exploiting the narrow resonance linewidth of the NVs, we form an image with a magnetic field gradient. In particular, we make use of a field-free point (shown in Fig. 1.5a) for reasons that will be explained in Chapter 3: Imaging Method and Apparatus. A field-free point can be created, for example, between two permanent magnets with north poles facing each other.

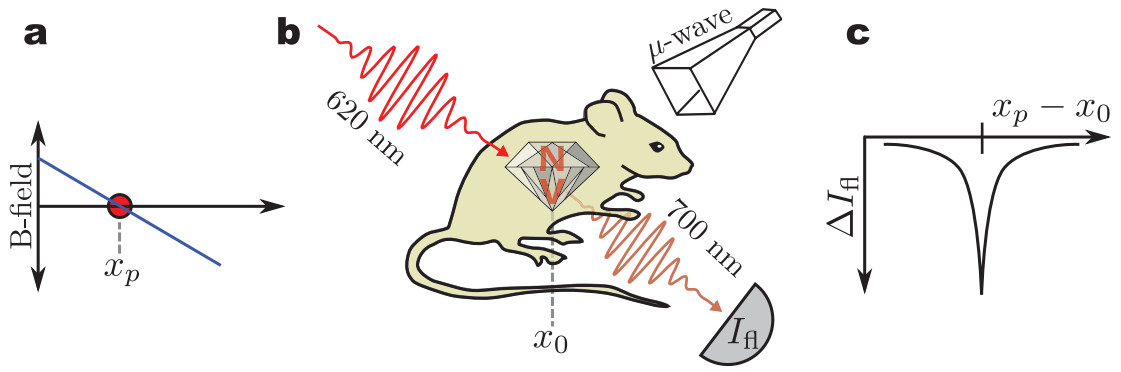

Figure 1.5: Overview of nanodiamond imaging. **a,** A magnetic field-free point is generated, such as exists between the north poles of two oppositely-directed magnets. **b,** An organism to be imaged has an arrangement of nanodiamonds within it, presumably arranged according to some physiological mechanism, and we would like to image the distribution of nanodiamonds. The organism is illuminated with red light and microwaves at the NV zero-magnetic-field resonance frequency and the fluorescence is recorded. **c,** As the field-free point sweeps across pockets of nanodiamonds, decreases in fluorescence are observed. The amount of decrease corresponds to the quantity of nanodiamond at the location of the field-free point.

Because we are performing magnetic resonance, we must introduce an oscillating magnetic field at the resonance frequency of the NVs; this is shown in Fig. 1.5b as "μ-wave", or microwaves. All the NVs near the field-free point x_p are resonant with applied microwaves. We detect the resonance optically by sending in red light and observing changes in the near-infrared fluorescence. As the field-free point moves over a point of NV-containing nanodiamonds, for example at x_0, the fluorescence decreases as in Fig. 1.5c. The amount of decrease of fluorescence is indicative of the quantity of nanodiamonds at the field-free point, and in actuality the raw image data consists of the convolution of the nanodiamond distribution with a point-spread function similar to what is shown in Fig. 1.5c. It is possible to deconvolve the raw image data with the point-spread function as a way of estimating the original nanodiamond distribution, but even without any analysis there is a strong visual correspondence between the raw image data and the actual nanodiamond distribution, such that the imaging process is not dependent on deconvolution.

My original contributions

I have proposed a new molecular imaging technique based on optically-detected functional electron spin resonance imaging (OD-*f*-ESRI). This contribution is a conceptual advancement of how to perform organism-scale imaging with NV-nanodiamond as contrast agent, at greatly reduced optical, microwave, and magnetic field intensities relative to the existing state of the art imaging with NVs,

while still taking advantage of the benefits that the NV confers in terms of sensitivity and resolution. I have designed and built a scanning system that I used to demonstrate imaging nanodiamonds in chicken breast with this approach, and I have designed and built a second scanner with a field of view large enough to image a live mouse. I've shown how the work I have done can be extended to true functional/molecular imaging, and I've included a discussion of the potential scaling of the technique's sensitivity and resolution, and placed it into a context of combining the best features of both molecular and anatomical imaging. Finally, I've introduced the concept of NV-based imaging to the field of molecular imaging.

Other contributions to the thesis include a walkthrough of the calculation of the NV energy levels based on group theory and symmetry, a calculation of NV spin polarization as a function of optical intensity, and modeling of the NV powder ODMR lineshape.

Some of my work presented here also appeared in a paper that I published (with my advisor, Prof. Eli Yablonovitch, as co-author) on this technique in the ACS journal *Nano Letters* [33], as well as from that paper's Supporting Information.

Overview of rest of thesis

Chapter 2: Theoretical Background begins with a discussion of the energy levels of the NV center and an explanation of how the singlet-triplet intersystem crossing arises based on symmetry and first principles. We describe a formula for the NV spin polarization as a function of optical intensity that is useful for estimating the signal amplitude. We then model the expected ODMR NV "powder" lineshape as a function of magnetic field and microwave frequency and we compare the model to measured data. This model takes into account the NV spin Hamiltonian and the interaction of the NVs with the light and microwaves, and it aids in understanding the behavior of the point-spread function. Chapter 3: Imaging describes the imaging method and the first two nanodiamond imaging systems in detail. Chapter 4: Experiments and Results details the sample preparation, shows the experimental results of imaging in chicken breast with the first system, and shows images with a large field of view from the second system. It also talks about how the point-spread function was obtained for the imaging systems, and it explains the deconvolution and image processing steps. Chapter 5: Discussion starts with a discussion of the point-spread function and provides a simple method for understanding it. We present a discussion of the possible ways to improve the technique, both in terms of sensitivity and resolution, including details of different optical and microwave pulse sequences. A comparison to other techniques is performed on the basis of sensitivity (in terms of mass of imaging agent) and resolution.

Chapter 2: Theoretical Background

Chapter Summary

We begin this chapter with an ab-initio discussion of the electronic energy levels of the nitrogen-vacancy center (NV) based on symmetry considerations (this section can be skipped without affecting the flow of the thesis, and the reader can continue with "Optically-induced spin polarization and optical spin detection"). The symmetry group of the NV, C_{3v}, is introduced, and a set of single-electron basis orbitals is constructed and projected onto irreducible representations of the group. By taking products of these states with their associated spin states, the full spin-orbit coupled states can be described, and it is evident that the intersystem crossing between the NV's triplet and singlet states arises due to spin orbit coupling.

Next, as is typical in the field when working with NVs at room temperature, a simplified five-level model of the NV is introduced. This model abstracts the details of the group-theoretic derivation yet contains enough detail to describe the optically-induced spin polarization and optical pumping, phenomena which are critical to understanding nanodiamond imaging. It is used to estimate the degree of spin polarization as a function of optical excitation intensity.

We then introduce the NV spin Hamiltonian, and use it to calculate the NV energy levels as a function of magnetic field. The Bloch equations for the interaction of a two-level system with an oscillating electromagnetic field are introduced as well. These are used to calculate the optically-detected magnetic resonance lineshape of an ensemble of NVs in nanodiamond powder as a function of magnetic field and microwave frequency. The calculation is compared to measurement.

The energy levels of the nitrogen-vacancy center as derived from symmetry considerations

One of the first questions one might consider when working with the NV center is what gives rise to the optically-polarizable and optically-detectable spin states. The answer lies in understanding the energy levels of the NV and the selection rules for various transitions between the energy levels. In particular, spin-orbit coupling is able to mix singlet and triplet states. The selection rules for the different transitions can be identified by considering the symmetry of the problem and using the formal mathematics of group theory. Here we give a build-up of an ab-initio model of the NV that contains enough information to explain the observed intersystem crossing and that loosely follows the treatment in [34], to which we refer the reader for a more complete treatment (also see [35]; for a good introduction to group-theoretic methods, consult [36]).

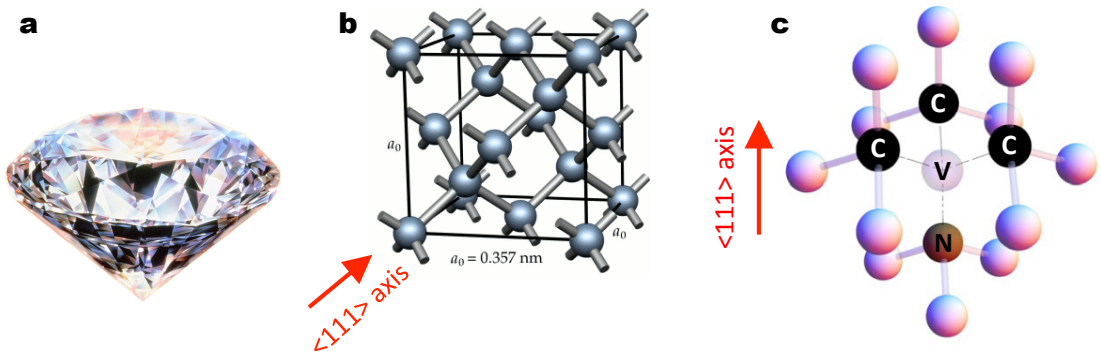

Figure 2.1: The diamond lattice and NV. **a**, A diamond gemstone with the "round brilliant" cut. **b**, The diamond lattice, composed of tetrahedrally arranged, covalently bonded carbon atoms; adapted from [37]. **c**, The NV center, indicating the location of the nitrogen (N), vacancy (V), and three nearest-neighbor carbon atoms (in black); adapted from [35].

We start with the diamond lattice, shown in Fig. 2.1b. The diamond lattice is composed of tetrahedrally arranged, covalently bonded carbon atoms. The atom positions lie on two inter-penetrating face-centered cubic (FCC) lattices. If we have unit cell vectors **a**, **b**, and **c** along the three primary axes, then in this basis, one of the FCC lattices is at the origin (0,0,0) and the other is shifted along all axes by a quarter of a unit cell to (¼, ¼, ¼). To make an NV, as shown in Fig. 2.1c, two carbons along the diamond's <111> axis are knocked out, and one is replaced with a nitrogen. As can be seen from Fig. 2.1b, there are four possible locations for an NV within each unit cell.

Much useful knowledge can be gained about the NV center by examining the symmetry of the NV under rotations and reflections. The NV belongs to a symmetry class called C_{3v}, also known as trigonal pyramidal, because the NV has the same symmetry as a pyramid with an equilateral triangle for a base. There are six different rotations and reflections that can map the NV onto itself: the identity E, (i.e., no operation), rotation by 120° or -120° (C_3^+ and C_3^-) about the <111> axis (which we now call the $\hat{z}$-axis), and reflection about one of the three vertical planes that contain the nitrogen atom and one of the neighboring carbon atoms (σ_d, σ_e and σ_f). Together these six operations constitute the C_{3v} point group. Because electrons have spin-½, we need to consider the double group associated with C_{3v}, which includes 12 operations: those of the original C_{3v}, and those of C_{3v} composed with rotation by 360° (which changes the sign of a spinor).

In order to understand the energy levels more deeply, it is insightful to note that the symmetry operations described above commute with the NV's Hamiltonian $\boldsymbol{H}$ [36]. That is, eigenstates of the Hamiltonian have the same energy even after being transformed by any of the symmetry operations. If an energy level is

associated with *n* linearly-independent, degenerate eigenstates, then applying a symmetry operator to one of these eigenstates can only map it into a linear combination of all the eigenstates associated with that energy level, because doing otherwise would change the energy of the energy level and be equivalent to saying that the symmetry operator does not commute with the Hamiltonian. Each set of degenerate eigenstates thus forms a *basis* for representing the symmetry operations for the point group, which cannot be further reduced and still faithfully represent the symmetry operations. We call such a basis an *irreducible representation*, as opposed to a *reducible representation.* By figuring out these basis functions, we can classify the energy levels according to their irreducible representation and understand qualitatively many behaviors of the NV center.

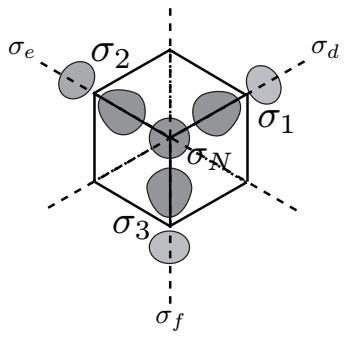

Figure 2.2: Nitrogen-vacancy center basis orbitals. From [34].

We do not know *a priori* what these symmetry-adapted basis orbitals will look like, but we can postulate that they are formed from linear combinations of the NV dangling bonds, as in Fig. 2.2, which looks down the $\hat{z}$-axis: $\{\sigma_1, \sigma_2, \sigma_3, \sigma_N\}$, as this basis is naturally suited to the symmetry of the problem. In this basis the various symmetry operators can be represented as follows:

Table 2.1: C_{3v} operators in the NV dangling bond basis.

$$E: \begin{pmatrix} 1 & 0 & 0 & 0 \\ 0 & 1 & 0 & 0 \\ 0 & 0 & 1 & 0 \\ 0 & 0 & 0 & 1 \end{pmatrix} \qquad C_3^+: \begin{pmatrix} 0 & 0 & 1 & 0 \\ 1 & 0 & 0 & 0 \\ 0 & 1 & 0 & 0 \\ 0 & 0 & 0 & 1 \end{pmatrix} \qquad C_3^-: \begin{pmatrix} 0 & 1 & 0 & 0 \\ 0 & 0 & 1 & 0 \\ 1 & 0 & 0 & 0 \\ 0 & 0 & 0 & 1 \end{pmatrix}$$

$$\sigma_d: \begin{pmatrix} 1 & 0 & 0 & 0 \\ 0 & 0 & 1 & 0 \\ 0 & 1 & 0 & 0 \\ 0 & 0 & 0 & 1 \end{pmatrix} \qquad \sigma_e: \begin{pmatrix} 0 & 0 & 1 & 0 \\ 0 & 1 & 0 & 0 \\ 1 & 0 & 0 & 0 \\ 0 & 0 & 0 & 1 \end{pmatrix} \qquad \sigma_f: \begin{pmatrix} 0 & 1 & 0 & 0 \\ 1 & 0 & 0 & 0 \\ 0 & 0 & 1 & 0 \\ 0 & 0 & 0 & 1 \end{pmatrix}$$

We say that these matrices form a reducible representation of C_{3v}, because although it is not yet obvious, there exists a transformation that will simultaneously block diagonalize all six matrices. We wish to find the new basis, in terms of linear combinations of the old basis, in which each operator has the same block diagonal form. Then, each block on the diagonal of one matrix will only multiply with a block in the same position of another matrix. The (transformed) basis functions belonging to a particular block will correspond to an irreducible representation of C_{3v}, and they will have the same energy.

A useful result of group theory is the *projection operator* [36], shown below:

$$\boldsymbol{P}^{\mu} = \sum_{\boldsymbol{R}} \overline{\chi^{\mu}(\boldsymbol{R})} \boldsymbol{O}_{\boldsymbol{R}}. \tag{2.1}$$

Given a reducible representation, one basis vector from that representation, and a row of the C_{3v} character table corresponding to a particular irreducible representation, the projection operator "projects out" the components of the reducible representation that belong to each irreducible representation. That is, it forms the linear transformations of the original basis vectors that block diagonalize the matrices of Table 2.1. Here, μ is the irreducible representation being projected onto, $\boldsymbol{R}$ represents an operation from the group, $\boldsymbol{O}_{\boldsymbol{R}}$ is the group operator for the operation $\boldsymbol{R}$ in the current (reducible) representation, and $\chi^{\mu}(\boldsymbol{R})$ is the character of the operation $\boldsymbol{R}$ in the representation μ. The derivation of Eq. 2.1 is beyond the scope of this thesis, but it is nicely presented in [36].

Table 2.2: The character table of the C_{3v} double group, adapted from [34]. Irreducible representations are in the left column; operators are in the top row. Overbars above each operator signify the un-barred operator composed with rotation by 360°. The right column describes functions that transform according to each irreducible representation. x, y, and z are functions of the respective coordinates; R_x, R_y, and R_z are rotation operators along those axes, α is spin-up and β is spin-down.

C_{3v}	E	$2C_3$	$3\sigma_v$	$\bar{E}$	$2\overline{C_3}$	$3\overline{\sigma_v}$	Functions
A_1	1	1	1	1	1	1	z, x^2+y^2, z^2
A_2	1	1	–1	1	1	–1	R_z
E	2	–1	0	2	–1	0	$(x,y), (R_x, R_y), (xy, x^2-y^2), (yz, xz)$
$E_{1/2}$	2	1	0	–2	–1	0	$(\alpha(\uparrow), \beta(\downarrow))$
${}^1E_{3/2}$	1	–1	i	–1	1	–i	$\alpha\alpha\alpha + i\beta\beta\beta$
${}^2E_{3/2}$	1	–1	–i	–1	1	i	$\alpha\alpha\alpha - i\beta\beta\beta$

The single electron orbitals of the NV center can be formed from linear combinations of the dangling bonds by using the projection operator of Eq. 2.1. Here we show explicitly how that works: A_1 is a one-dimensional irreducible representation, so the character is the same as the group element. Reading from the character table (Table 2.2), we have $\chi^{A_1}(E) = \chi^{A_1}(C_3) = \chi^{A_1}(\sigma_v) = 1$, and applying Eq. 2.1 sequentially to each basis orbital, we get (first, for σ_1):

$$\begin{aligned} \boldsymbol{P}^{A_1}\sigma_1 &= (1\cdot E + 1\cdot C_3^+ + 1\cdot C_3^- + 1\cdot\sigma_d + 1\cdot\sigma_e + 1\cdot\sigma_f)\sigma_1 \\ &= \sigma_1 + \sigma_2 + \sigma_3 + \sigma_1 + \sigma_3 + \sigma_2 \end{aligned} \tag{2.2}$$

which, when normalized, becomes $a_C = (\sigma_1 + \sigma_2 + \sigma_3)/\sqrt{3}$. Applying the projection operator $\boldsymbol{P}^{A_1}$ sequentially to the other dangling bond basis functions, we find there is only one more linearly independent basis function in A_1, that of $a_N = \sigma_N$. Projecting onto the A_2 irreducible representation does not yield any basis functions, and projecting onto the E representations yields three basis functions, two of which are linearly independent and can be expressed as follows, after normalization: $e_x = (2\sigma_1 - \sigma_2 - \sigma_3)/\sqrt{6}$, and $e_y = (\sigma_2 - \sigma_3)/\sqrt{2}$. Graphical depictions of the basis functions are shown below in Fig. 2.3:

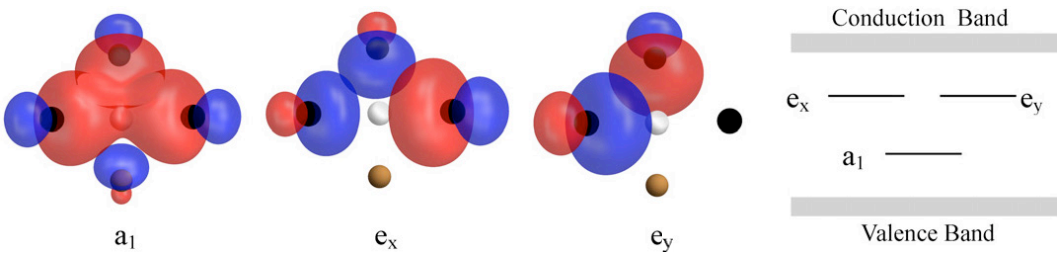

Figure 2.3: Single electron orbitals of the NV center in the C_{3v} point group. From Fig. 2 of [35].

Here, the a_1 orbital is actually a superposition of the a_N and a_C orbitals. Another non-degenerate superposition a_1' exists, but it is most likely within the diamond's valence band. The energy ordering, determined from electron-ion Coulomb interactions, shows that the states within the diamond bandgap are a_1 and the degenerate pair e_x, e_y, with a_1 lying lowest (note that for attractive interactions, the symmetric state generally lies lower in energy) [34], [35].

Ultimately we are interested in the multi-electron wavefunctions, which we get by taking direct products of the single-electron wavefunctions and their spin states, and then projecting out the resultant wavefunctions onto the irreducible representations of C_{3v}. The Kronecker, or tensor, product of the irreducible representations will in general produce a representation that is reducible. To proceed, we start by counting the number of electrons present: one from each of the three carbon dangling bonds, two more from the nitrogen dangling bond, and a sixth (such that the NV is negatively-charged), presumably from a substitutional nitrogen in the diamond lattice [21]. They fill up the lowest energy levels first, such that there are two electrons in a_1', two in a_1, and one each in e_x and e_y. Rather than thinking of the NV center in terms of its six electrons, we can think of it in terms of two "holes", because only two more electrons are needed to form a "closed shell", i.e., to fill the available energy levels. In terms of the hole representation, e^2 is lowest in energy, and ae is the first excited state, whereby an electron from the a energy level has been promoted to the e energy level.

We now attempt to project the product states onto each irreducible representation, this time using the full double group character table because spin is involved. For the state e^2, we can actually use a shortcut to figure out all the possible energy levels, otherwise the matrices to represent the symmetry operators would be 16-dimensional (2x two dimensions for spin, and 2x two dimensions for each E representation). We start by forming the four-dimensional products of *only* the spin states or *only* the spatial states, and projecting these onto the irreducible representations.

For example, let's say that we wanted to find the irreducible representations of the product of two spin-halfs (in this thesis, we refer to the spin-half

representation of C_{3v} as $E_{1/2}$, although it is also referred to as $D_{1/2}$ elsewhere). We start by constructing the matrices for the symmetry operations in this representation by considering the standard rotations for a spin-half in SU(2) (see, for example, [38], Problem 4.56):

$$U(\hat{\boldsymbol{n}}, \theta) = \cos\frac{\theta}{2} - i(\hat{\boldsymbol{n}} \cdot \boldsymbol{\sigma}) \sin\frac{\theta}{2}, \tag{2.3}$$

where θ is the angle of rotation about the axis $\hat{\boldsymbol{n}}$, and $\boldsymbol{\sigma}$ is a vector of the Pauli matrices. Note that reflections can be composed from spatial inversions and proper rotations, where we explicitly choose the gauge that spatial inversion does not change the phase of the spinor (the Pauli gauge, as opposed to the Cartan gauge). The resulting matrices are below (to get the corresponding operator of the double group, multiply by $\bar{E} = -E$):

Table 2.3: C_{3v} operators in the spin-half representation.

$$E: \begin{pmatrix} 1 & 0 \\ 0 & 1 \end{pmatrix} \qquad C_3^+: \begin{pmatrix} e^{-i\frac{\pi}{3}} & 0 \\ 0 & e^{i\frac{\pi}{3}} \end{pmatrix} \qquad C_3^-: \begin{pmatrix} e^{i\frac{\pi}{3}} & 0 \\ 0 & e^{-i\frac{\pi}{3}} \end{pmatrix}$$

$$\sigma_d: \begin{pmatrix} 0 & e^{-i\frac{\pi}{6}} \\ e^{-i\frac{5\pi}{6}} & 0 \end{pmatrix} \qquad \sigma_e: \begin{pmatrix} 0 & e^{-i\frac{5\pi}{6}} \\ e^{-i\frac{\pi}{6}} & 0 \end{pmatrix} \qquad \sigma_f: \begin{pmatrix} 0 & i \\ i & 0 \end{pmatrix}$$

The operators in Table 2.3 were calculated using Eq. 2.3 with $C_3^+ = U(n_z, 2\pi/3)$, $C_3^- = U(n_z, -2\pi/3)$, and $\sigma_\alpha = \mathbb{i}U(\hat{\boldsymbol{n}}_\alpha, \pi)$, with $\mathbb{i}$ representing the spatial inversion operator, and $\alpha \in \{d, e, f\}$, according to Fig. 2.4. As expected, the traces of each matrix agree with the $E_{1/2}$ row of the character table.

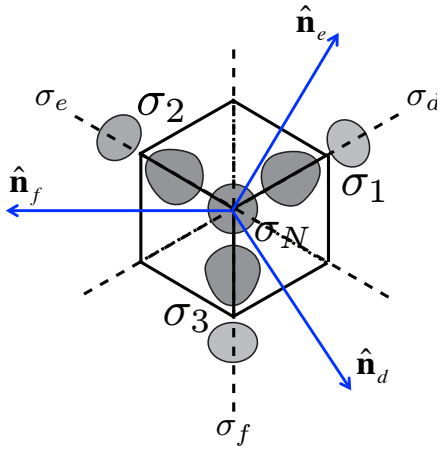

Figure 2.4: Arrows indicating unit vectors for forming C_{3v} reflections out of inversions and proper rotations.

We have two spin-halfs, which in general when added together generate either singlet or triplet states. However, we can find the symmetry-adapted combinations of the spin states by application of the projection operator, Eq. 2.1, on each of the spin-product basis functions, $|\uparrow\uparrow\rangle, |\downarrow\downarrow\rangle, |\uparrow\downarrow\rangle$ and $|\downarrow\uparrow\rangle$. Symmetry operators in this basis are given by the Kronecker products of each of the matrices in Table 2.3 (and the associated double group matrices) with themselves. We find that the (antisymmetric under particle interchange) singlet state $|\uparrow\downarrow - \downarrow\uparrow\rangle$ has symmetry A_1, and the (symmetric under particle interchange) triplet states include $|\uparrow\downarrow + \downarrow\uparrow\rangle$ ($m_s = 0$) with symmetry A_2 and the doublet $|\uparrow\uparrow\rangle, |\downarrow\downarrow\rangle$ ($m_s = \pm 1$) with symmetry E.

We follow an analogous procedure to find the irreducible representations of $E \otimes E$. First, we must find matrices for the symmetry operations in the E representation, which we can do by considering the symmetry operations as they act on basis vectors $\hat{\boldsymbol{x}}$ and $\hat{\boldsymbol{y}}$:

Table 2.4: C_{3v} operators in the doublet (E) representation.

$$E: \begin{pmatrix} 1 & 0 \\ 0 & 1 \end{pmatrix} \qquad C_3^+: \begin{pmatrix} -\frac{1}{2} & -\sqrt{\frac{3}{2}} \\ \sqrt{\frac{3}{2}} & -\frac{1}{2} \end{pmatrix} \qquad C_3^-: \begin{pmatrix} -\frac{1}{2} & \sqrt{\frac{3}{2}} \\ -\sqrt{\frac{3}{2}} & -\frac{1}{2} \end{pmatrix}$$

$$\sigma_d: \begin{pmatrix} \frac{1}{2} & \sqrt{\frac{3}{2}} \\ \sqrt{\frac{3}{2}} & -\frac{1}{2} \end{pmatrix} \qquad \sigma_e: \begin{pmatrix} \frac{1}{2} & -\sqrt{\frac{3}{2}} \\ -\sqrt{\frac{3}{2}} & -\frac{1}{2} \end{pmatrix} \qquad \sigma_f: \begin{pmatrix} -1 & 0 \\ 0 & 1 \end{pmatrix}$$

The traces of these matrices agree with the E row of the character table. There are four possible combinations of e orbitals in our four-dimensional space: $|e_x e_x\rangle$, $|e_x e_y\rangle$, $|e_y e_x\rangle$, and $|e_y e_y\rangle$. Projecting each basis function onto each irreducible representation, we find the following states: $|e_x e_x + e_y e_y\rangle$ with symmetry A_1, $|e_x e_y - e_y e_x\rangle$ with symmetry A_2, and the pair $|e_x e_x - e_y e_y\rangle$ and $|e_x e_y + e_y e_x\rangle$ with symmetry E. Note that only the second state is antisymmetric with respect to particle interchange; thus, only this state can be paired with the spin triplet, whereas all the other states must be paired with the spin singlet.

We now pair together (take products of) the spin and spatial wavefunctions calculated above, making sure that the overall wavefunction is antisymmetric with respect to particle interchange to satisfy the Pauli exclusion principle. (This is the trick that reduces our 16-dimensional problem to a more manageable 6-dimensional problem.) To determine the overall symmetry, it is sufficient to multiply, element by element, a row of the character table (Table 2.2) corresponding to the symmetry of the first part of the product wavefunction with the row corresponding to the symmetry of the second part of the product. The result can be expressed as a linear combination of rows of the character table, and if there is only one row in the linear combination, that row determines the symmetry of the product. To illustrate, the symmetry of the first row in Table 2.5 is A_1 because the first row of the character table multiplied by itself is (1,1,1,1,1,1) × (1,1,1,1,1,1) = (1,1,1,1,1,1), and dotting this with each row of the character table it is a linear combination of (in fact equal to) only the first row.

Table 2.5: Symmetrized states of the energy level e^2, with conventional state name indicated in parenthesis in the last column.

Spatial states	Symmetry	Spin states	Symmetry	Overall symmetry
$\lvert e_x e_x + e_y e_y\rangle$	A_1			A_1 ($^1A_1$)
$\lvert e_x e_x - e_y e_y\rangle$	E	$\lvert\uparrow\downarrow - \downarrow\uparrow\rangle$	A_1	E ($^1E_1$)
$\lvert e_x e_y + e_y e_x\rangle$	E			E ($^1E_2$)
		$\lvert\uparrow\uparrow\rangle$	E	E ($^3A_2$; $m_s = +1$)
$\lvert e_x e_y - e_y e_x\rangle$	A_2	$\lvert\uparrow\downarrow + \downarrow\uparrow\rangle$	A_2	A_1 ($^3A_2$; $m_s = 0$)
		$\lvert\downarrow\downarrow\rangle$	E	E ($^3A_2$; $m_s = -1$)

Now, we would like to generate a similar table for the first excited electronic state, *ae*. We start by finding the reducible 8-dimensional matrices representing the C_{3v} operators in the product basis, given by the Kronecker product of the representations as follows: $\boldsymbol{O}_R^{A\otimes E\otimes E_{1/2}\otimes E_{1/2}} = \boldsymbol{O}_R^A \otimes \boldsymbol{O}_R^E \otimes \boldsymbol{O}_{E_{1/2}} \otimes \boldsymbol{O}_{E_{1/2}}$, and we then use Eq. 2.1 to project each of the 8 elementary basis functions ($\lvert a_1 e_x \uparrow\uparrow\rangle$, $\lvert a_1 e_x \uparrow\downarrow\rangle$ … $\lvert a_1 e_y \downarrow\downarrow\rangle$) onto each of the irreducible representations. This operation yields the following (un-symmetrized) products, with $e_\pm = e_x \pm i e_y$:

Table 2.6: Unsymmetrized states of the energy level *ae*.

Symmetry	State
A_1	$\lvert a_1 e_-\rangle \otimes \lvert\uparrow\uparrow\rangle + \lvert a_1 e_+\rangle \otimes \lvert\downarrow\downarrow\rangle$
A_2	$\lvert a_1 e_-\rangle \otimes \lvert\uparrow\uparrow\rangle - \lvert a_1 e_+\rangle \otimes \lvert\downarrow\downarrow\rangle$
E	$\lvert a_1 e_+\rangle \otimes \lvert\uparrow\uparrow\rangle$
	$\lvert a_1 e_x\rangle \otimes \lvert\uparrow\downarrow\rangle$
	$\lvert a_1 e_x\rangle \otimes \lvert\downarrow\uparrow\rangle$
	$\lvert a_1 e_-\rangle \otimes \lvert\downarrow\downarrow\rangle$
	$\lvert a_1 e_y\rangle \otimes \lvert\uparrow\downarrow\rangle$
	$\lvert a_1 e_y\rangle \otimes \lvert\downarrow\uparrow\rangle$

We must antisymmetrize the states in the above table to make them consistent with the Pauli exclusion principle. State $\lvert a_1 e_\pm\rangle$ thus becomes state $\lvert E_\pm\rangle = \lvert a_1 e_\pm\rangle - \lvert e_\pm a_1\rangle$, and states $\lvert a_1 e_{x,y}\rangle$ become states $\lvert X, Y\rangle = \lvert a_1 e_{x,y}\rangle - \lvert e_{x,y} a_1\rangle$. Finally, we must take superpositions of the spin states $\lvert\uparrow\downarrow\rangle$ and $\lvert\downarrow\uparrow\rangle$ to give them definite triplet or singlet character. Performing the above steps finally gives us the symmetrized states of the first excited electronic level, named as in Table 1 of [34]:

Table 2.7: Symmetrized states of the energy level *ae*. These are very similar to Table 1 of [34] and the states follow the same naming convention.

Symmetry	State	Spin
A_1	$A_1 = \|E_-\rangle \otimes \|\uparrow\uparrow\rangle + \|E_+\rangle \otimes \|\downarrow\downarrow\rangle$	Triplet
A_2	$A_2 = \|E_-\rangle \otimes \|\uparrow\uparrow\rangle - \|E_+\rangle \otimes \|\downarrow\downarrow\rangle$	Triplet
E	$E_1 = \|E_-\rangle \otimes \|\downarrow\downarrow\rangle + \|E_+\rangle \otimes \|\uparrow\uparrow\rangle$	Triplet
	$E_2 = \|E_-\rangle \otimes \|\downarrow\downarrow\rangle - \|E_+\rangle \otimes \|\uparrow\uparrow\rangle$	Triplet
	$E_x = \|X\rangle \otimes \|\uparrow\downarrow + \downarrow\uparrow\rangle$	Triplet
	$E_y = \|Y\rangle \otimes \|\uparrow\downarrow + \downarrow\uparrow\rangle$	Triplet
	${}^1E_x = \|a_1 e_x + e_x a_1\rangle \otimes \|\uparrow\downarrow - \downarrow\uparrow\rangle$	Singlet
	${}^1E_y = \|a_1 e_y + e_y a_1\rangle \otimes \|\uparrow\downarrow - \downarrow\uparrow\rangle$	Singlet

The energy levels shown above in Tables 2.5 and 2.7 are summarized in Fig. 2.5 below. Here, we include (qualitatively) energy splittings due to many different mechanisms that are described in quantitative detail elsewhere [34], [35]. First, electron-electron Coulomb repulsion splits the singlet and triplet levels of the ground state e^2, with the triplet lying lowest in energy, due to Hund's first rule: a symmetric spin state (triplet) results in an anti-symmetric spatial part of the wave-function, which is generally lower in energy because the electrons are further apart. However, there are other processes that lead to further energy splittings. The ground electronic state ${}^3A_2$ splits into $m_s = 0$ and $m_s = \pm 1$ spin substates due to spin-spin coupling. While spin-spin coupling is isotropic in a spherically-symmetric potential and would otherwise average to zero, the anisotropy of the crystal field—that is, the C_{3v} symmetry of the diamond lattice—splits the spin-spin coupling into axial ($m_s = 0$) and transverse ($m_s = \pm 1$) components. The transverse components will split further into X and Y components in the presence of crystal strain, which further distorts the lattice. In the excited state ${}^3E$, there is also spin-spin coupling, as well as spin-orbit coupling, which causes further energy splittings.

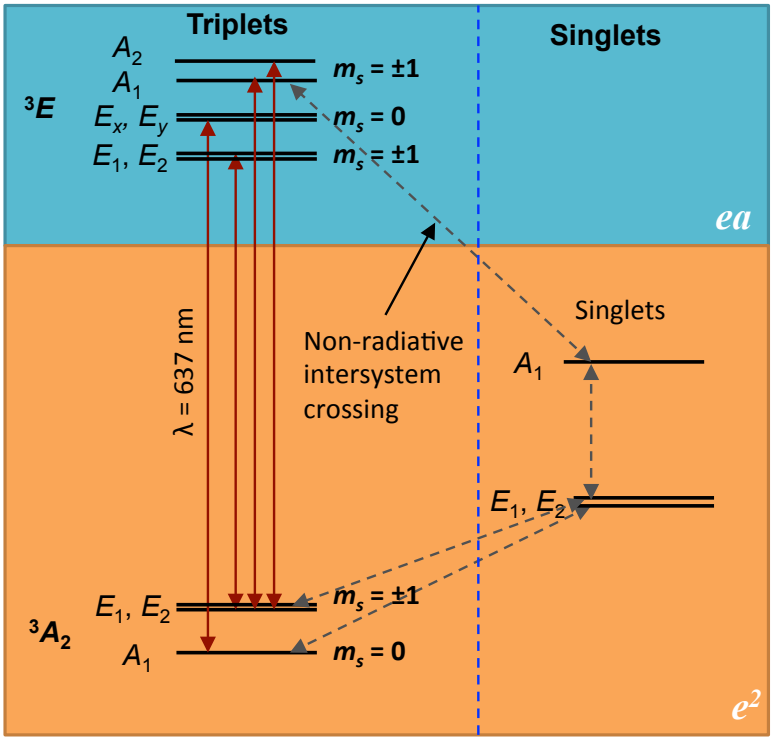

Figure 2.5: The full NV level structure, incorporating (almost) all the energy levels of the group-theoretic model, except for the excited state singlets. Electric dipole transitions are spin-conserving, and the allowed optical electric dipole transitions (for the triplets) are shown in red. Spin-orbit coupling links states of the same irreducible representation; here, we show possible non-radiative intersystem crossing mediated by spin-orbit coupling and symmetric vibrational relaxation, conserving both energy and total angular momentum. For the triplets, the symmetry of each electronic state is indicated in bold, and the spin-orbit coupled symmetry is indicated next to each energy level. For the singlets, since there is no net spin (S = 0) the spin-orbit coupled symmetry and the electronic symmetry are the same, indicated next to each level. See also Figure 1 of [34] and Figures 3 and 4 of [35].

The group-theoretic analysis of the NV's energy levels was not just an academic exercise or even just a way of naming the energy levels and estimating their splitting. Rather, by understanding the symmetry of each energy level, we have a direct way to evaluate whether or not certain transitions will occur, by use of selection rules. For example, let us consider the optical electric dipole transition between $^3A_2$ and ^3E. Electric dipole transitions are spin-conserving, meaning the spin must not flip when the NV absorbs a photon and transitions to its excited state. To determine if an optical transition is possible, we need to determine if transition dipole matrix elements are non-zero. These matrix elements are of the form $\langle 1|\vec{r}|2\rangle$, where $\vec{r}$ is the position operator, $|1\rangle$ is the initial state, and $|2\rangle$ is the final state. We

will thus be evaluating integrals of the form $\int \psi_1^* \vec{\boldsymbol{r}} \psi_2 \, d^3\vec{\boldsymbol{r}}$, and a necessary (but not sufficient) condition for these integrals to be non-zero is if the integrand contains a component that is totally symmetric with respect to the C_{3v} point group operations. Because we already know how states $|1\rangle$ and $|2\rangle$ transform from doing the group theoretic analysis, and we know the components of $\vec{\boldsymbol{r}}$ transform as (E, E, A_1) according to Table 2.2, we can figure out the symmetry of the integrands as follows: multiply, element by element, the rows of the character table (Table 2.2) corresponding to the symmetry of each term in the product, and then take the dot product of the result with the A_1 row of the character table. If it is non-zero, an optical transition between those two states might occur.

To show this more explicitly, let us consider a transition from the $m_s = 0$ sublevel of $^3A_2$ to the $m_s = 0$ sublevel of ^3E. This is a possible transition because it would preserve the spin projection. Now we evaluate the symmetry of the matrix elements for each of the x, y, and z components of the vector $\vec{\boldsymbol{r}}$. For x and y, we have $A_1 \otimes E \otimes E$, and multiplying these rows of the character table yields (1,1,1,1,1,1) × (2,-1,0,2,-1,0) × (2,-1,0,2,-1,0) = (4,1,0,4,1,0), and dotting this with (1,1,1,1,1,1) yields $1\times4\times1 + 2\times1\times1 + 3\times0\times1 + 1\times4\times1 + 2\times1\times1 + 3\times0\times1 = 10 \neq 0$, where we have explicitly included the degeneracy factors of each class of operator. Thus, optical transitions between these states, for the electric field polarized along the x and y axes, are not immediately forbidden by symmetry (and they in fact do occur—to E_x orbitals when polarized along the x-axis and E_y orbitals when polarized along the y-axis). However, for electric field polarized along the z-axis, we have $A_1 \otimes A_1 \otimes E$, and consulting the character table and repeating the above process, we find that the resultant matrix element does not contain the irreducible representation A_1 and hence must be equal to zero.

It is important to understand the spin-orbit coupling of the NV center to gain at least a first order understanding of the optically-induced spin polarization and spin detection, as it is the spin-orbit coupling which gives rise to intersystem crossing between the singlet and triplet states. When the spin and the orbital angular momentum of an isolated system are coupled, the total angular momentum (or the rotational symmetry of the total state) is still conserved, even though the spin or orbital angular momentum (or rotational symmetry of the spatial/spin parts of the wave function) may change as angular momentum oscillates between the two types. This is why we wrote the wave function of each state in terms of the overall rotational symmetry, including spin and spatial parts, as it becomes immediately apparent (for example, from Fig. 2.5) where possible transitions could cause a triplet/singlet crossing. In Fig. 2.5, we see that the $m_s = \pm1$ sublevels of the excited state include a state with A_1 character, which can couple to the A_1 singlet level by spin-orbit coupling, assisted by symmetric vibrations in order to conserve energy (and total angular momentum) [39].

A more complete understanding of the optically-induced spin polarization must take into account the electron-vibration interaction and asymmetric vibrations,

which allow additional intersystem crossing channels, as detailed in [40]. However, thermal averaging of the levels shown in Fig. 2.5 produce an effective 5-level system as in Fig. 2.7, which provides an adequate understanding of the optically-induced spin polarization and detection for the purposes of the current work. For the most up-to-date empirical data regarding the intersystem crossing rates between the different levels, see Table I of [41].

Optically-induced spin polarization and optical spin detection

As described in the previous section, the symmetry of the NV center gives rise to a particular electronic level structure. Due to details of the interactions between the electronic levels, such as spin-orbit coupling, the spin of the NV can be both polarized and read out optically. In this section we explain the link between the level structure and the optically-induced spin polarization and optical spin detection mechanisms.

The concept of spin polarization can be understood by analogy to the case of a ferromagnet in an external magnetic field. In Fig. 2.6(a), arrows indicate the orientation of the magnetic domains of a hypothetically unpolarized piece of ferromagnetic material. The magnetic domains spontaneously form because of an exchange interaction that favors parallel spins [42]; however, in the absence of an applied magnetic field, there is little net magnetization because magnetic domains spontaneously form as a way of relaxing the total stored energy. In (b), after the application of a magnetic field pointing to the right, magnetic domains align along the magnetic field (both by growth of magnetic domains pointing along the field, not illustrated, and by rotation of the magnetic moments of the domains, illustrated), and we say that the ferromagnetic material is polarized.

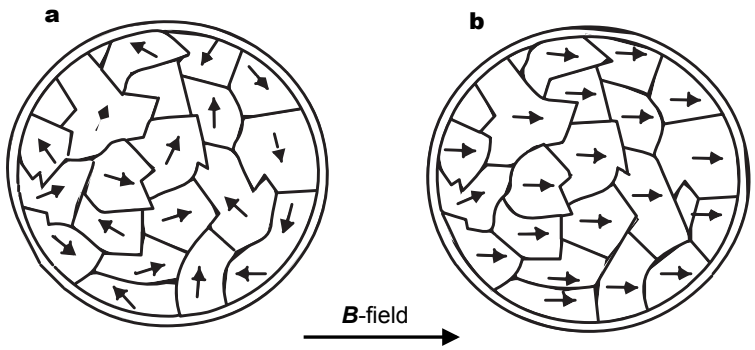

Figure 2.6: Ferromagnet domains aligning in an applied magnetic field. **a**, before field is applied. **b**, after field is applied. Adapted from [43].

A similar polarization effect is observed for a nitrogen-vacancy center spin (which polarizes along the diamond <111> axis rather than along an external magnetic field) under continuous optical excitation. In Fig. 2.7, we show a simplified

five-level model of the NV electronic level structure. This model contains enough detail to explain the essential dynamics of the optically-induced spin polarization and optical detection, abstracting the complexity of the full group-theoretic model shown in Fig. 2.5. Note the spin-conserving optical dipole transitions between the electronic ground state $^3A_2$ and the first excited electronic state ^3E. There is also a non-radiative transition from the $m_s = \pm 1$ spin states of ^3E to the intermediate singlet states. Although there is a non-zero probability of the $m_s = 0$ spin state of ^3E to decay through the intermediate singlet states, this probability is about 7 times lower than for $m_s = \pm 1$ [41], so it is not indicated in Fig. 2.7. As we explain below, it is this asymmetry in decay paths between the spin states that gives rise to the optically-induced spin polarization and optical spin detection. Note that the singlets decay to all spin sublevels of the $^3A_2$ ground state non-selectively.

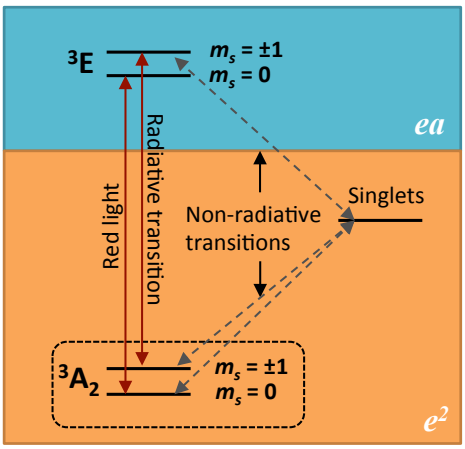

Figure 2.7: A simplified version of the NV level structure with transitions necessary for explaining the essential dynamics of optically-induced spin polarization and optical detection.

In Fig. 2.8 we show how the initially unpolarized spin becomes polarized in the presence of optical excitation. In panel (a), two spin population subsets of the ground state are represented: spins in the $m_s = 0$ spin sublevel are represented by a light circle, while spins in the $m_s = \pm 1$ spin sublevel are represented by a dark circle. This situation represents what happens in thermal equilibrium. Given that the splitting between the two spin sublevels is roughly 3 GHz, the Boltzmann factor is roughly unity ($2\pi\hbar \cdot 3\ \text{GHz} \ll kT \approx 2\pi\hbar \cdot 6\ \text{THz}$), hence the spin population is equally split over all three triplet sublevels. After applying optical excitation, in (b) we see that the spin populations end up in the excited electronic state, and that the (electric dipole) transition has preserved the spin orientation of the NVs. While the $m_s = 0$ spin sublevel decays directly to the $m_s = 0$ spin sublevel of the ground state, the $m_s = \pm 1$ sublevel can decay through the intermediate singlet states (c). This

causes the majority of the spin population to transfer into the $m_s = 0$ sublevel (d) after repeated optical cycling.

It is also possible to understand the difference in fluorescence intensity of the spin sublevels, i.e., the optical spin detection mechanism, by examining the level structure, as shown in Fig. 2.9. The white circle, representing population in the $m_s = 0$ spin sublevel, can decay only radiatively, thus it will fluoresce brighter (by ~30%) than the $m_s = \pm 1$ sublevels, which can decay both radiatively and non-radiatively.

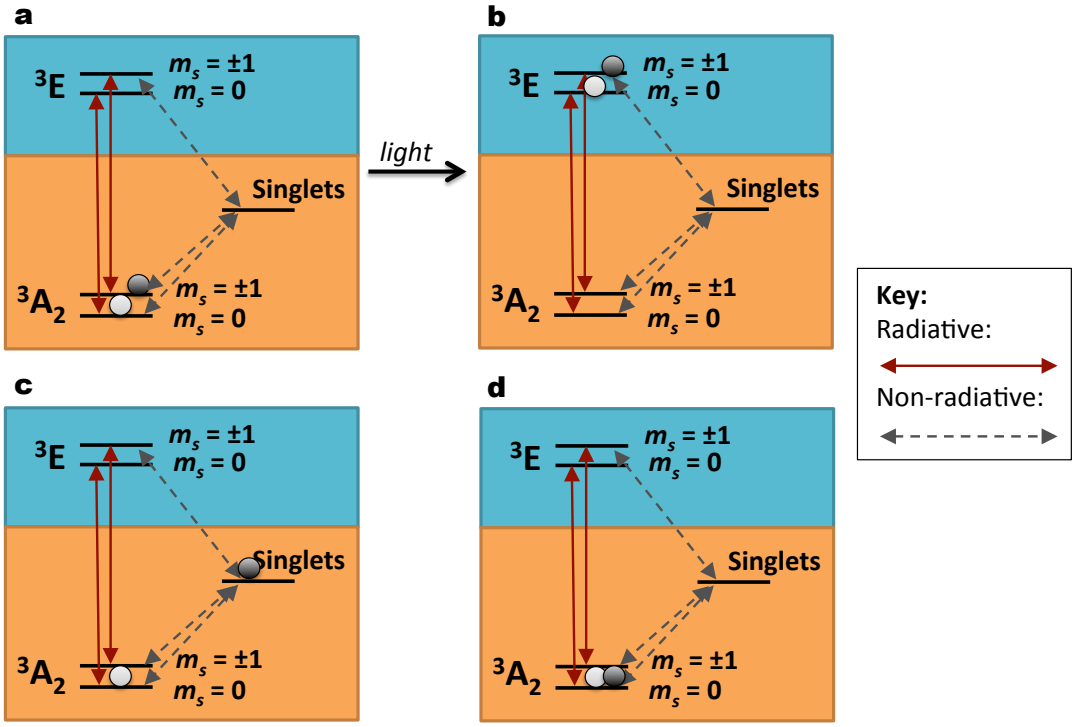

Figure 2.8: The NV spin polarization cycle. **a**, Unpolarized spin population represented by light and dark circles (this is the equilibrium state at room temperature). **b**, After absorbing a photon, each spin state is excited into the corresponding spin state of the first excited electronic state, conserving spin orientation. **c**, The $m_s = 0$ spin sublevel decays directly to the $m_s = 0$ spin sublevel of the ground state, while the $m_s = \pm 1$ spin sublevel can decay to the intermediate singlet states. **d**, Upon repeated optical cycling, the spin population transfers into the $m_s = 0$ spin sublevel.

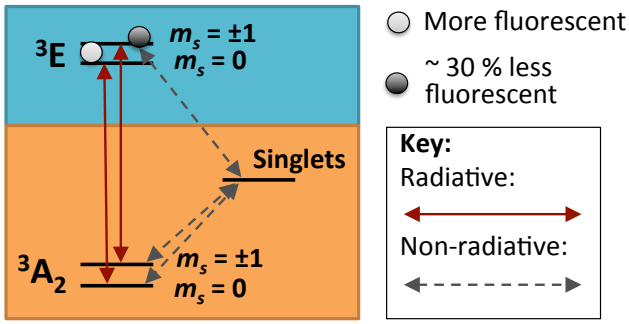

Figure 2.9: Spin-dependent fluorescence intensity is a result of the $m_s = 0$ spin sublevel decaying only radiatively and the $m_s = \pm 1$ sublevel decaying both radiatively and non-radiatively.

Spin polarization vs. optical excitation intensity

It is possible to model the spin polarization as a function of optical pump intensity. To do this we need three pieces of information: the NV's optical cross-section σ, the spin relaxation time T_1, and the branching ratio for the different spin decay paths as in Fig. 2.9, which will quantify how much spin polarization is generated per optical cycle. These pieces of information are summarized in the following table:

Table 2.8: Spin polarization modeling parameters.

Parameter	Symbol	Value	Reference
Optical cross-section	σ	10^{-16} cm^2	[44]
Spin relaxation time	T_1	1.2 ms	[45]
Probability of transferring from state 0 to state ±1 per optical cycle	P_{12}	0.08	[46]
Probability of transferring from state ±1 to state 0 per optical cycle	P_{21}	0.034	[46]

Assuming an optical intensity I in W cm^{-2}, and photon energy in Joules of hc/λ, the number of photons received per unit time by a given NV center is $1/t_{\text{phot}} = I\sigma\lambda/hc$. Given the probabilities of transferring from state $m_s = 0$ to state $m_s = \pm 1$ per optical cycle, we can work out the continuous rates that correspond to these processes as follows. If we assume that the cumulative probability distribution for the transfer from one state to the other follows an exponential law with rates r_{12} and r_{21}, then the following equations hold:

$$P_{12} = 1 - \exp\left(-r_{12} t_{\text{phot}}\right), \text{ and}$$
$$P_{21} = 1 - \exp\left(-r_{21} t_{\text{phot}}\right). \qquad (2.4, 2.5)$$

Now, let us express the relative proportion of spin population in states $m_s = 0$ and $m_s = \pm 1$ with the quantity $\rho_1 - \rho_2$, where ρ_1 and ρ_2 could (for example) represent the diagonal entries of a density matrix describing the full state. We postulate the following rate equation:

$$\frac{d(\rho_1 - \rho_2)}{dt} = 2r_{21}\rho_2 - 2r_{12}\rho_1 - \frac{\rho_1 - \rho_2}{T_1}. \qquad (2.6)$$

The above equation essentially states that the time rate of change of the relative spin population depends on three terms: the rate at which population from ρ_2 is transferring to ρ_1 (and vice versa), and the spin relaxation between the two states. Solving Eq. 2.6 for the steady state condition, combined with the fact $\rho_1 + \rho_2 = 1$, we get:

$$\rho_1 = \frac{2r_{21} + \frac{1}{T_1}}{2r_{21} + 2r_{12} + \frac{2}{T_1}}, \qquad (2.7)$$

which, when combined with Eqs. 2.4 and 2.5 and with the values for P_{12} and P_{21}, gives:

$$\rho_1 = \frac{0.83 + \frac{t_{\text{phot}}}{T_1}}{1 + 2\frac{t_{\text{phot}}}{T_1}}. \qquad (2.8)$$

Note that this equation is consistent with saturated spin polarizations ($t_{\text{phot}} \to 0$) of $\rho_\infty \approx 80\%$ [46]. The spin polarization relative to saturation and taking into account the equilibrium spin polarization 0.5 is thus:

$$\text{Fractional spin polarization} = \frac{\rho_1 - 0.5}{\rho_\infty - 0.5}, \qquad (2.9)$$

which we plot in Fig. 2.10 as a function of optical intensity by combining the information in Table 2.8 with Eq. 2.8.

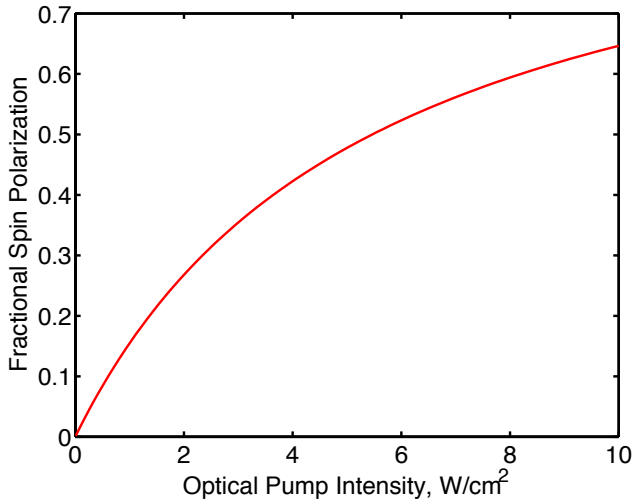

Figure 2.10: Fractional spin polarization vs. optical pump power.

It is interesting to note the high level of NV spin polarization achievable by optical pumping as compared to the amount of nuclear spin polarization generated in a clinical MRI machine. Specifically, consider the case of protons in a B_0 = 1.5 T magnetic field, a typical field strength for clinical MRI. The gyromagnetic ratio of a proton is $\gamma/2\pi$ = 42.577 MHz T^{-1}. Spin polarization is generated in thermal equilibrium as a slight excess number of spins relax along the applied magnetic field. The Boltzmann factor for proton spins antiparallel to the field vs. proton spins parallel to the field is $\exp(-\hbar\gamma B_0/kT)$. At room temperature this factor is approximately 0.99999, indicating that there is a net nuclear spin polarization of 10 parts per million. This spin polarization is about five orders of magnitude smaller than the maximum possible NV spin polarization of ~80%. MRI still has plenty of sensitivity, at least for anatomical imaging—tissue is primarily made up of water, and there are 55 moles of water per liter (1000 g/liter divided by 18 g/mol) or 110 moles of protons per liter of water. However, for molecular imaging with exogenous contrast agents, the quantity of material detected is so much smaller than for anatomical imaging, so the sensitivity must be correspondingly higher. For example, the first iteration nanodiamond imaging system has a sensitivity of about 1 mM of carbon atoms, assuming a 1 mm^3 voxel and 1 Hz measurement bandwidth (as discussed in "Measurement of sensitivity")—so the material concentration that a nanodiamond imaging system can sense is at least 7 orders of magnitude smaller than for an MRI system.

The high sensitivity of NV-based imaging relative to MRI stems partly from the high NV spin polarization that can be generated optically. However, optical detection of the NV spin state is much more sensitive than the inductive detection of precessing spins used in MRI. Even for micro-sized versions of MRI, the weakness of nuclear magnetism limits the detection sensitivity to voxels of well over a micrometer on a side [47], [48]. Such voxels already contain ~10^{11} protons,

whereas it is straightforward to detect the spin state of an individual NV optically [49].

There are a couple of other key distinguishing factors between nanodiamond imaging and MRI that need emphasis. First, nanodiamond imaging is concerned with detecting *electron* spin, rather than *nuclear* spin. The gyromagnetic ratio of an electron (roughly equal to that of the NV) is 657x the gyromagnetic ratio of a proton. Thus, the "response" of the NV to external magnetic fields will be that much greater, resulting in potentially higher spatial resolution than for MRI. However, resonance linewidth is also an important factor in determining spatial resolution, as broad linewidths typically limit spatial resolution. For example, a linewidth $\Gamma = 1/T_2$ will have a spatial resolution of $\Delta x = \Gamma/\gamma G$ in a magnetic field gradient G. The linewidths of NVs in nanodiamonds ($\Gamma/2\pi \sim$ MHz) [20] are much broader than typical proton linewidths in biological tissue ($\Gamma/2\pi \sim$ tens of Hz) [50]. Second, because NV spin polarization is generated optically, there is no need for the large superconducting magnet used in MRI to polarize the nuclear spins. This greatly reduces the cost of a nanodiamond imaging system as compared to an MRI system.

The NV optically-detected magnetic resonance powder lineshape

When performing an optically-detected magnetic resonance (ODMR) experiment on nanodiamonds containing NVs, the NVs will be exposed to a static magnetic field $\boldsymbol{B_0}$ with a given magnitude and direction, a microwave magnetic field $\boldsymbol{B_1}$ with given magnitude, direction and frequency, and an optical field. We can start to develop an understanding of the ODMR lineshape of NVs in nanodiamond powder by first analyzing the NV Hamiltonian, solving for the eigenstates of the time-independent part, then using the Bloch equations for a two-level system (see, for example, [51]) to analyze the microwave-induced transitions between the time-independent Hamiltonian's eigenstates. Then, because an ensemble of nanodiamonds is actually comprised of a large number of individual nanodiamonds with crystalline axes arbitrarily oriented, we must sum up the contribution of lineshapes from each possible orientation.

We start with a discussion of the NV spin Hamiltonian in Eq. 2.10. The two most important terms to include for the purposes of our discussion are the Zeeman interaction and the zero-field splitting. The Zeeman interaction represents the energy of the NV's magnetic dipole moment in an external magnetic field, while the zero-field splitting refers to the splitting between the spin sublevels of the NV's ground state that exists even in the absence of an external magnetic field. This splitting, which arises from spin-spin coupling, would not be expected in the case of a spherically symmetric system where the spin-spin coupling would average to zero. However, because C_{3v} symmetry breaks spherical symmetry into axial (z) and transverse (lateral or x, y) components, the spin sublevels will have definite C_{3v} axial or lateral symmetry, and in general will have different energies. In particular, the NV has a splitting of $D = 2\pi\hbar\cdot 2.869$ GHz between the $m_s = 0$ (axial symmetry) and the $m_s = \pm 1$ (lateral symmetry) spin states. In addition, strain along the x- or y-axes

will distort the C_{3v} symmetry of the NV and cause the m_s = ±1 levels to split further (and form superpositions with definite x or y symmetry). The amount of strain splitting is captured by the term E, which is on the order of a few megahertz for the nanodiamonds used in the experiments described in this thesis.

The NV Hamiltonian combining zero-field splitting (first two terms) and the Zeeman interaction (final term) is shown in the following equation:

$$H = DS_z^2 + E\left(S_x^2 - S_y^2\right) - g\mu_B \boldsymbol{B} \cdot \boldsymbol{S}, \tag{2.10}$$

where g is the Landé g-factor of the NV (≈ 2), $\boldsymbol{B}$ is the external magnetic field, and μ_B is the Bohr magneton (see [52] for an example discussion of spin Hamiltonians). $\boldsymbol{S} = (S_x, S_y, S_z)$ is a vector of the Pauli matrices for spin-1:

$$\begin{aligned} \boldsymbol{S} &= \left(S_x, S_y, S_z\right) \\ &= \left(\frac{1}{\sqrt{2}}\begin{pmatrix} 0 & 1 & 0 \\ 1 & 0 & 1 \\ 0 & 1 & 0 \end{pmatrix}, \frac{1}{\sqrt{2}}\begin{pmatrix} 0 & -i & 0 \\ i & 0 & -i \\ 0 & i & 0 \end{pmatrix}, \begin{pmatrix} 1 & 0 & 0 \\ 0 & 0 & 0 \\ 0 & 0 & -1 \end{pmatrix}\right). \end{aligned} \tag{2.11}$$

The next step in our analysis of the NV ODMR lineshape is to find the energy levels and eigenstates of the NV Hamiltonian. The energy levels for a single NV depend on the relative orientation of the NV axis with the applied magnetic field. The NV axis ($\hat{z}$-axis) is set by the zero-field splitting term D and corresponds to the <111> direction in the diamond crystal. For magnetic fields $\boldsymbol{B_0} \ll D/g\mu_B \approx$ 0.1 T (2.8 GHz), to a first approximation we can neglect the portion of $\boldsymbol{B_0}$ that is perpendicular to the NV axis and only include the projection along the NV axis. That is, the shift in energy levels for the m_s = ±1 sublevels will be given by $\pm g\mu_B |\boldsymbol{B_0}| \cos\theta$, where θ is the angle between the NV axis and $\boldsymbol{B_0}$. A plot of the energy levels (actually, the transition frequency for 0→+1 and 0→-1 transitions) as a function of θ is shown below, in Fig. 2.11, for $|\boldsymbol{B_0}|$ = 30 G.

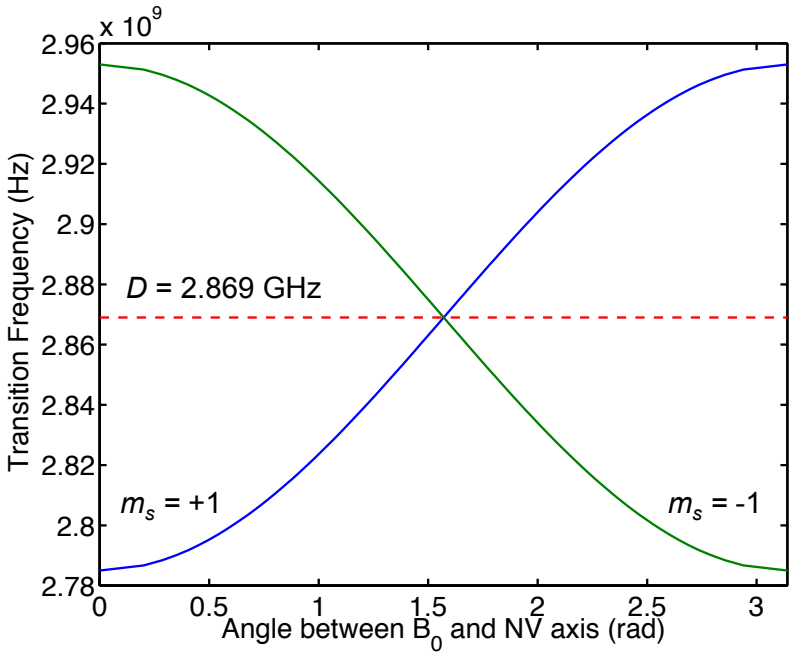

Figure 2.11: NV energy levels as a function of angle with respect to a 30 G field (first approximation), illustrating the cosine projection of the field along the NV axis, with center frequency given by D = 2.869 GHz. "Transition Frequency" refers to the frequency of the 0→+1 and 0→-1 transitions.

From Fig. 2.11, one can deduce that for a number of nanodiamonds with angle θ in the range $\theta \in [\theta_0, \theta_0 + d\theta]$, the energy levels of these nanodiamonds will appear in a range $\omega \in [\omega_0, \omega_0 + d\omega]$ with $\omega_0 = (D \pm g\mu_B|\boldsymbol{B_0}|\cos\theta_0)/\hbar$, and $d\omega = \left|\frac{d\omega}{d\theta}\right|_{\theta=\theta_0} d\theta = g\mu_B|\boldsymbol{B_0}|\sin\theta\, d\theta/\hbar$. For nanodiamonds randomly oriented in solid angle, the probability of finding nanodiamonds within a given range $\theta \in [\theta_0, \theta_0 + d\theta]$ is $p_\Theta(\theta_0)d\theta = \sin\theta\, d\theta/2$; thus, $p_\omega(\omega_0)d\omega = p_\Theta(\theta_0)\left|\frac{d\theta}{d\omega}\right|_{\theta=\theta_0} d\omega = \hbar d\omega/2\, g\mu_B|\boldsymbol{B_0}|$. That is, in nanodiamond powder, the probability is uniform for finding spin transitions with energy in the range $D \pm g\mu_B|\boldsymbol{B_0}|$, at least to first order.

A plot of the first-order calculation of NV energy levels as a function of magnetic field strength is shown in Fig. 2.12. In (a), we see the NV energy levels for the magnetic field directed along the z-axis for a single NV. In (b), we consider the case of nanodiamond powder, which contains an ensemble of NVs at random orientations with respect to the applied magnetic field. Here, the energy levels for one randomly oriented NV will appear between the two extreme frequencies in (a); we illustrate the uniform distribution of energy levels between the two extreme frequencies by use of a gradient.

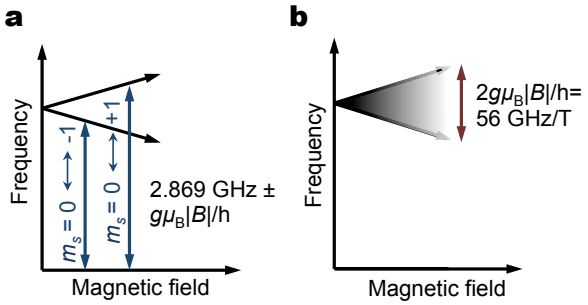

Figure 2.12: NV spin transition frequencies in a magnetic field. **a**, Transition frequencies for a single NV; the magnetic field is along the NV axis. **b**, Transition frequencies for an ensemble of NVs in nanodiamond powder. The magnetic field is randomly oriented with respect to a given NV within the ensemble, thus the transition frequencies for a given NV will be somewhere in between the two extreme frequencies depicted in **a**.

Notice the $1/|\boldsymbol{B_0}|$ dependence of the probability of energy levels being within a certain range. This dependence implies that the number of possible microwave transitions at the center frequency of 2.869 GHz decreases inversely with the magnetic field strength. It also helps explain why the point-spread function of the imaging system has a $1/|\boldsymbol{r}|$ dependence in a magnetic gradient $\boldsymbol{G}$, i.e. $\boldsymbol{B_0} = \boldsymbol{G} \cdot \boldsymbol{r}$. However, in order to fully understand the point-spread function, we must do more in-depth calculations of the NV energy levels that take into account strain in the nanodiamonds and the full quantum-mechanical solution to the time-independent Hamiltonian. As will be seen, these additional details describe the observed anti-crossing between the $m_s = \pm 1$ states as well as the blue-shift of the center of the anti-crossing from 2.869 GHz with increasing magnetic field. Even without taking into account this anti-crossing and blue-shift, the probability for a microwave transition is not quite uniform with frequency: there is a decreased transition amplitude around 2.869 GHz because the NVs at that frequency are oriented perpendicular to the applied magnetic field, and if the microwave field is also perpendicular to the applied magnetic field, there may be a part of the microwave field that is parallel to the NV spin axis and thus not be able to induce a transition.

We can proceed by solving for the energy levels of the full Hamiltonian without strain ($E = 0$). Results of this calculation are shown below in Fig. 2.13 for the case $|\boldsymbol{B_0}| = 30$ G, where the angle between the magnetic field and the NV's axis varies from 0 to π.

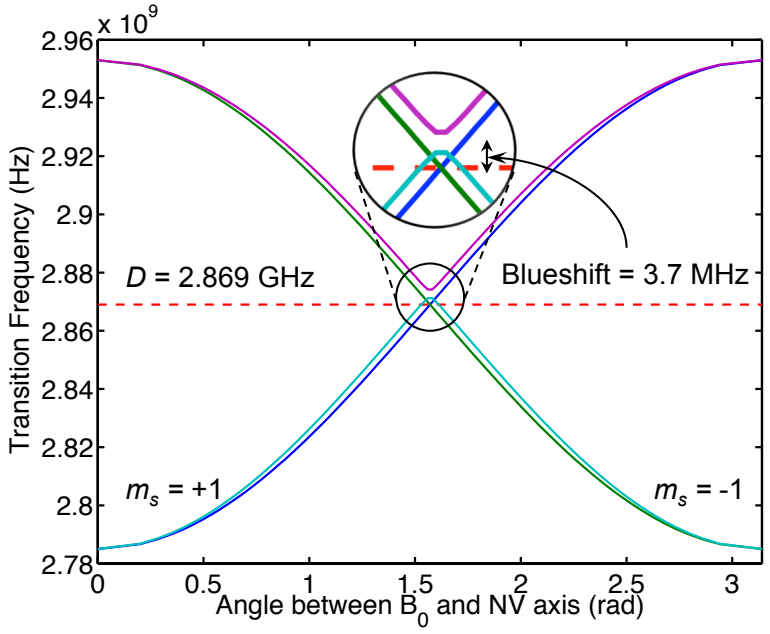

Figure 2.13: The NV's energy levels (relative to the energy of $m_s = 0$) as a function of angle, calculated by solving the full Hamiltonian. Included are the simple estimates of the NV energy levels from Fig. 2.11, as well as the results of the full calculation. Inset: anti-crossing, and blue-shift of anti-crossing from the simple case.

Note the presence of an anti-crossing between the lower branch (antisymmetric combination of $m_s = +1$ and $m_s = -1$, transforms as $\hat{y}$) and upper branch (symmetric combination, transforms as $\hat{x}$). This anti-crossing blue-shifts with applied magnetic field, and is an important factor in determining the nanodiamond imaging point-spread function. The addition of strain creates an anti-crossing even at zero applied magnetic field, and as we will see in Chapter 5: Discussion, this limits both image contrast and resolution.

The interaction of a two-level quantum system with a radiation field

In order to understand the lineshape further it is instructive to do a basic analysis of the interaction of a two-level quantum system with a radiation field, yielding the Bloch equations (see [51], [53]). A prototypical two-level system is shown below in Fig. 2.14, with states $|1\rangle$, $|2\rangle$ and corresponding energy levels E_1 and E_2, in the presence of a time-harmonic magnetic field with frequency ω.

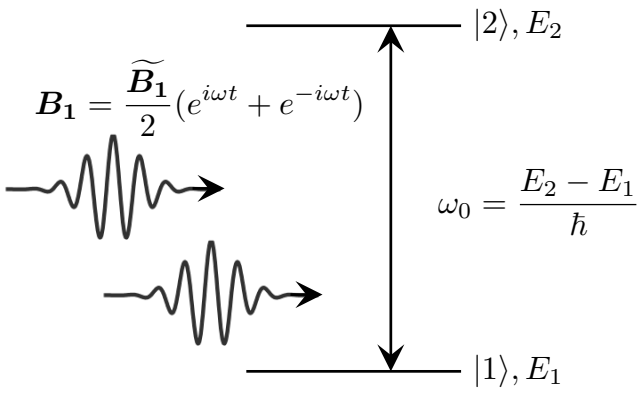

Figure 2.14: A prototypical two-level system in a time-harmonic magnetic field.

The most general pure quantum state of a single two-level system can be described by the wavefunction $\psi = a|1\rangle + b|2\rangle$, but because we are dealing with an ensemble of systems being probed together, we must use the density matrix formalism to completely capture the behavior. Thus, we take $\rho = \psi\psi^*$, and $\rho_{11} = |a|^2, \rho_{22} = |b|^2, \rho_{12} = \rho_{21}^* = ab^*$, where the subscript refers to the index in the 2x2 matrix ρ.

The density matrix evolves according to the density matrix formulation of the Schrödinger equation,. We can derive this by taking the Hermitian conjugate of the Schrödinger equation ($H\psi = i\hbar\frac{\partial\psi}{\partial t}$) and recalling that the Hamiltonian is Hermitian so equal to its conjugate transpose, giving us $\psi^* H = -i\hbar\frac{\partial\psi^*}{\partial t}$. Thus,

$$\frac{\partial\rho}{\partial t} = \frac{\partial}{\partial t}\psi\psi^* = -\frac{i}{\hbar}H\psi\psi^* + \frac{i}{\hbar}\psi\psi^* H = -\frac{i}{\hbar}[H, \rho]. \qquad (2.12)$$

The total Hamiltonian consists of the time-independent part H_0 and the time-dependent part H_1: $H = H_0 + H_1$. Let us assume that the time-dependent part is the magnetic dipole interaction as in Eq. 2.10, $H_1 = g\mu_B \boldsymbol{B_1} \cdot \boldsymbol{S}$, and that the states $|1\rangle$ and $|2\rangle$ are the energy eigenstates of the time-independent part. Taking note that H_1 is responsible for causing transitions between the states, we ignore terms $\langle 1|H_1|1\rangle$ and $\langle 2|H_2|2\rangle$, which we assume are small relative to the inter-state energy, and also oscillate quickly relative to the rate of transitions between states. We can evaluate each matrix element of Eq. 2.12 separately, to obtain

$$\begin{aligned}\frac{\partial\rho_{21}}{\partial t} &= -\frac{i}{\hbar}[H_0 + H_1, \rho]_{21} \\ &= -i\omega_0\rho_{21} - \frac{i}{\hbar}(\rho_{11} - \rho_{22})H_{1,21} \\ &= -i\omega_0\rho_{21} + i\gamma\boldsymbol{B_1} \cdot \boldsymbol{S_{21}}(\rho_{11} - \rho_{22})\end{aligned} \qquad (2.13)$$

and

$$\begin{aligned}\frac{\partial \rho_{11}}{\partial t} &= -\frac{i}{\hbar}[H_0 + H_1, \rho]_{11} \\ &= -\frac{i}{\hbar}(\rho_{21} - \rho_{21}^*)H_{1,12} \\ &= i\gamma \boldsymbol{B_1} \cdot \boldsymbol{S_{12}}(\rho_{21} - \rho_{21}^*)\end{aligned} \tag{2.14}$$

where we've substituted in the transition frequency $\omega_0 = (E_1 - E_2)/\hbar$, as well as the definition of H_1. Note we can arbitrarily choose the phases of eigenstates $|1\rangle$ and $|2\rangle$ so we choose them to make $\boldsymbol{S_{12}}$ real and thus equal to $\boldsymbol{S_{21}}$. Due to the normalization condition of the wavefunction, $\rho_{11} + \rho_{22} = 1$, we have

$$\frac{\partial}{\partial t}(\rho_{11} - \rho_{22}) = 2i\gamma \boldsymbol{B_1} \cdot \boldsymbol{S_{12}}(\rho_{21} - \rho_{21}^*). \tag{2.15}$$

So far, we have not included the effects of dephasing of the ensemble or of relaxation to an equilibrium population. These terms are easily included phenomenologically and can be incorporated by the parameters T_2 and T_1, respectively, into Eqs. 2.13 and 2.15:

$$\frac{\partial \rho_{21}}{\partial t} = -i\omega_0 \rho_{21} + i\gamma \boldsymbol{B_1} \cdot \boldsymbol{S_{21}}(\rho_{11} - \rho_{22}) - \frac{\rho_{21}}{T_2} \tag{2.16}$$

and

$$\begin{aligned}&\frac{\partial}{\partial t}(\rho_{11} - \rho_{22}) \\ &\quad = 2i\gamma \boldsymbol{B_1} \cdot \boldsymbol{S_{12}}(\rho_{21} - \rho_{21}^*) - \frac{(\rho_{11} - \rho_{22}) - (\rho_{11} - \rho_{22})_0}{T_1}.\end{aligned} \tag{2.17}$$

These constitute the so-called "Bloch" equations for a two-level system because they are identical in form to the Bloch equations used to describe magnetic resonance [51].

We next introduce the slowly-varying amplitude σ such that $\rho_{21}(t) = \sigma_{21}(t)e^{-i\omega t}$, and we solve for the steady-state condition (i.e., vanishing time-derivatives). We assume $\boldsymbol{B_1} = \widetilde{\boldsymbol{B_1}} \cos \omega t = \widetilde{\boldsymbol{B_1}}\left(e^{i\omega t} + e^{-i\omega t}\right)/2$, define the Rabi frequency $\Omega = g\mu_B \widetilde{\boldsymbol{B_1}} \cdot \boldsymbol{S_{21}}/2\hbar$, define $\Delta N = (\rho_{11} - \rho_{22})$, and drop counter-rotating terms (terms that oscillate at ±2ω). Eq. 2.16 yields:

$$\sigma_{21} = \frac{-\Omega \Delta N}{\omega - \omega_0 + \frac{i}{T_2}}, \tag{2.18}$$

which, when plugged into Eq. 2.17, yields

$$\frac{\Delta N - \Delta N_0}{\Delta N_0} = \frac{4\Omega^2 T_1 T_2}{1 + (\omega - \omega_0)^2 T_2^2 + 4\Omega^2 T_1 T_2}. \qquad (2.19)$$

Estimating the lineshape

We now turn to estimating the powder lineshape of the NV's optically-detected magnetic resonance. In the previous section, we calculated the change in equilibrium population for an ensemble of identical two-level systems interacting with an oscillating magnetic field; this change was summarized in Eq. 2.19. When translating this equation to the situation of optically detected magnetic resonance of an ensemble of nitrogen-vacancy centers in nanodiamond powder, there are many additional considerations to take into account. We must first recall that the equilibrium spin population given by ΔN_0 is *not* the thermal equilibrium population. Rather, it is the steady-state spin population in the presence of the optical excitation field, where optical spin pumping competes with thermal spin relaxation. Thus, the value used for T_1 in Eq. 2.19 should be replaced by the time it takes for the NV to relax to its steady-state value of polarization, which can be calculated as

$$\frac{1}{T_1} = \frac{1}{T_{1,\text{ spin relaxation}}} + \frac{1}{T_{\text{pump}}}, \qquad (2.20)$$

with T_{pump} referring to the time it takes to reach $(1 - e^{-1})$ of the total optically-induced spin polarization.

With this change, Eq. 2.19 could then represent the shape of the optically-detected magnetic resonance for an ensemble of NVs, but only if they were identically oriented with respect to an external magnetic field. In addition, it is only representative of a single transition, say $m_s = 0$ to $m_s = 1$, assuming the $m_s = -1$ was detuned enough from the $0 \rightarrow 1$ transition to not interact with the microwave field. The difference in spin population described by Eq. 2.19 can be measured by observing the change in fluorescence as a function of microwave frequency. Because the $m_s = \pm 1$ states fluoresce more dimly than the $m_s = 0$ state by about 30%, and at steady state the microwaves can at best equalize the spin population between the two states of a transition, we expect at most a 15% change in fluorescence for a completely saturated microwave transition. This assumes that we have fully polarized the spins optically, otherwise the actual change in fluorescence will be a fraction of the 15%, given by the fraction in spin polarization as calculated from Eq. 2.8.

Equation 2.19 only corresponds to one particular situation in the ensemble of NVs to be measured. We must take into account the full ensemble of variations: the strain (E in the Hamiltonian) of the nanodiamonds will vary according to a

particular probability density function $p_E(E)$, and the NV axes will be randomly oriented with respect to both the microwave and magnetic fields. (Figure 2.15 below illustrates the summing up of transitions occurring in nanodiamonds with <111> axis at an angle θ with respect to the external magnetic field.) Finally, because we have a three-level system with a shared lower level (m_s = 0) we cannot simply add the contributions to the lineshape from transitions to different upper levels, as the transitions interact via the lower level.

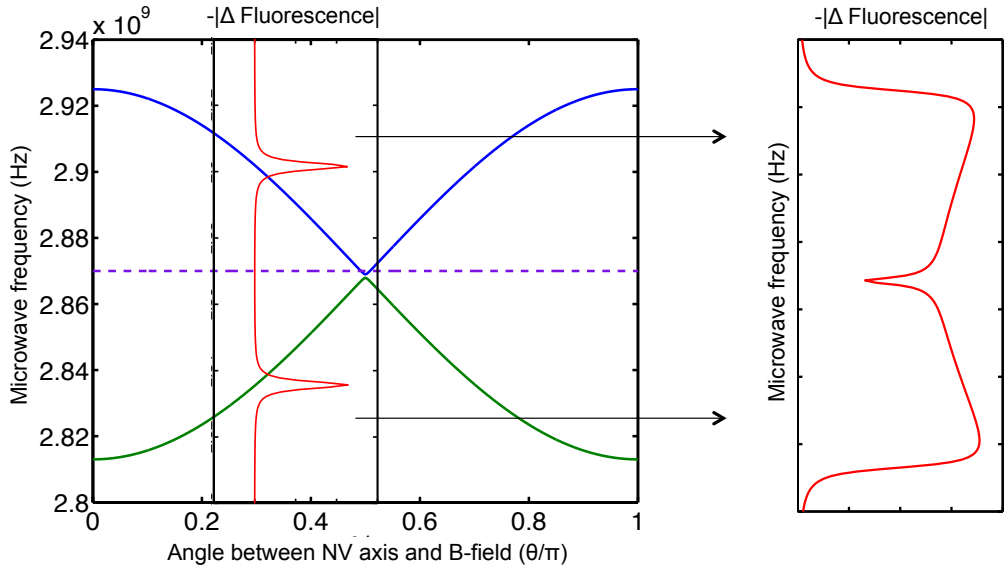

Figure 2.15: Creating the ODMR lineshape from individual NV transitions. The nanodiamonds, and hence the NV axes, are randomly oriented in space with respect to the external magnetic field. The lower and upper lines of the graph on the left represent the NV transition center frequencies as a function of the angle θ between the NV axis and the external magnetic field. For a given angle, two transitions occur that are detectable as decreases in NV fluorescence centered at each NV transition frequency. One must sum over all angles in the nanodiamond ensemble to calculate the change in fluorescence of NVs in nanodiamond powder as a function of microwave frequency, right.

Let us assume our $\boldsymbol{B_0}$ and $\boldsymbol{B_1}$ axes are known and fixed in the lab frame. For a given member of the ensemble, we obtain three states (with three corresponding energy levels) when solving the Hamiltonian. Call them $|0\rangle$, $|1\rangle$ and $|2\rangle$, with $|0\rangle$ consisting primarily of the m_s = 0 state and $|1\rangle$ and $|2\rangle$ consisting of superpositions of the m_s = ±1 states. Label their eigenenergies as E_0, E_1, and E_2, respectively, such that there are two transitions we are addressing: $\omega_1 = (E_1 - E_0)/\hbar$, and $\omega_2 = (E_2 - E_0)/\hbar$. Then, calculate the Rabi frequency for each transition:

$$\Omega_i(E,\alpha,\beta,\gamma) = \frac{g\mu_B}{2\hbar}\langle 0|\widetilde{\boldsymbol{B}}_1 \cdot \boldsymbol{S}|i\rangle, \tag{2.21}$$

with $i \in \{1,2\}$ referring to the state number, and α, β, and γ referring to the Euler angles rotating the NV relative to the $\hat{z}$-axis of the lab frame (note: here γ doesn't refer to gyromagnetic ratio). Armed with this information, we calculate the lineshape for one of the transitions per Eq. 2.19:

$$h_i(\omega,E,\alpha,\beta,\gamma) = \frac{4\Omega_i^2 T_1 T_2}{1+(\omega-\omega_i)^2 T_2^2 + 4\Omega_i^2 T_1 T_2} \tag{2.22}$$

and combine the two transition lineshapes together:

$$h(\omega,E,\alpha,\beta,\gamma) = f(h_1,h_2). \tag{2.23}$$

We use $f(h_1(\omega),h_2(\omega)) = \max(h_1(\omega),h_2(\omega))$, a "winner-takes-all" paradigm for selecting which transition out of the two is favored at a given frequency, justified by the fact that we are well into saturation ($4\Omega^2 T_1 T_2 \gg 1$) and both transitions share the $m_s = 0$ level.

Finally, the ensemble lineshape is calculated by averaging over the strain distribution and over the Euler angles:

$$h(\omega) = \int_\gamma \int_\beta \int_\alpha \int_E h(\omega,E,\alpha,\beta,\gamma) p_E(E)\, dE \frac{d\alpha}{2\pi} \sin\beta \frac{d\beta}{2} \frac{d\gamma}{2\pi}. \tag{2.24}$$

We can model the strain distribution as a Gaussian:

$$p_E(E) = \frac{1}{\sqrt{2\pi\sigma_E}} \exp -\frac{(E-\mu_E)^2}{2\sigma_E^2}. \tag{2.25}$$

We now have all the tools necessary to calculate the expected ODMR powder lineshape for NVs, with given magnetic field and microwave field orientations. We use the parameters summarized below in Table 2.9, which have been varied by hand to produce the best qualitative fit to measured data.

Table 2.9: Parameters used to estimate the NV ODMR powder lineshape. All parameters were selected to produce the best qualitative fit with the measured data (i.e., a quantitative optimization was not done, but could potentially be adapted to this framework).

Parameter	Symbol	Value
Mean strain value	μ_E	4 MHz
Standard deviation of strain value	σ_E	2 MHz
Spin-lattice relaxation time	T_1	0.5 ms
Spin-spin relaxation time	T_2	0.7 μs
Microwave field strength	$\|\boldsymbol{B_1}\|$	0.1 G

The measured ODMR data is obtained using a modified version of the experimental apparatus as described in Chapter 3: Imaging . Essentially, a 2x2 mm square of double-sticky tape covered with 10 μg of 100 nm nanodiamonds was prepared. The double-sticky tape was illuminated with red light at ~620 nm and an optical intensity of ~1 W cm^{-2}. Microwaves were applied via a ~12 mm square loop that surrounded the piece of double-sticky tape, and the microwaves were chopped at 379 Hz. The modulation in fluorescence was measured synchronously as a function of microwave frequency (from 2.819 to 2.919 GHz in 1 MHz steps) and magnetic field (from -40 G to 40 G in 1 G increments), for the cases of magnetic field parallel to microwave field and magnetic field perpendicular to microwave field.

We show the results of our estimation in the following figures and compare them to measured data. The measured data is shown first in Fig. 2.16, both as an intensity plot (a,b) and as a stacked plot as magnetic field is increased to 40 G (c,d). Several features of note are apparent from these plots. First, their "X"-like character can be explained by the presence of transitions at (almost) all frequencies between the two extreme frequencies that occur when the NV axis is aligned with the magnetic field, as in Fig. 2.12(b). Second, the anti-crossing between the $|X\rangle$ and $|Y\rangle$ levels (symmetric and anti-symmetric superpositions of $m_s = 1$ and $m_s = -1$) both increases in size and blue-shifts with increasing magnetic field. Finally, at the center frequency, the ODMR amplitude decays more quickly with increasing magnetic field for the case in (b) (with B_0 perpendicular to B_1), versus the case in (a). The geometry of the first apparatus described in Chapter 3: Imaging Method and Apparatus is such that when used to image 2D projections of nanodiamond within pieces of chicken breast, the magnetic field is also perpendicular to the microwave field, thus giving us the sharpest point-spread function.

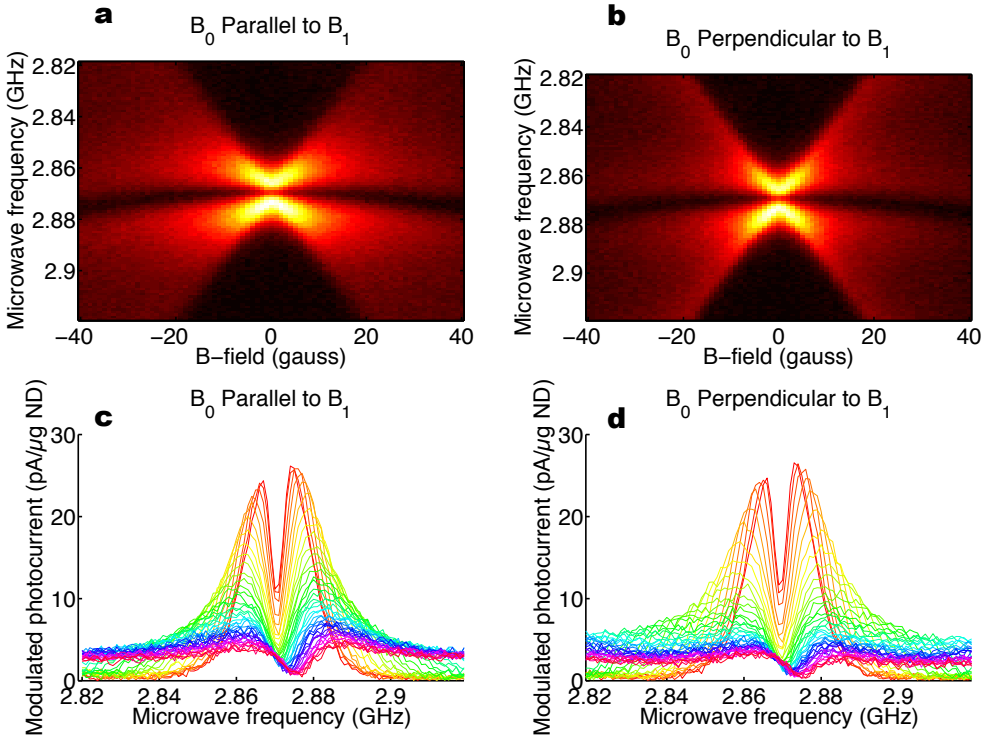

Figure 2.16: Measured ODMR data. (a), magnetic field (B_0) parallel to microwave field (B_1). (b), magnetic field perpendicular to microwave field. (c) and (d), same as (a) and (b), except presented as stacked plots. The vertical axis corresponds to the portion of the photocurrent modulated by the magnetic resonance, expressed in terms of picoamps of photocurrent per microgram of nanodiamond. Note the increasing blue-shift of the anti-crossing as the magnetic field increases.

In Fig. 2.17 we show the results of the simulated ODMR data, over the same frequency range as in Fig. 2.16, and for magnetic fields in 1 G increments from -100 G to 100 G. The simulated data was qualitatively matched to the measured data by varying the parameters in Table 2.9, running the simulation again, and comparing the results across a range of magnetic fields as in Fig. 2.18. Although only qualitative optimization was done, in theory a quantitative optimization could have been performed, for example by calculating the gradient of the squared error between the model output and the measured data with respect to the model parameters, and then performing an optimization via conjugate gradient descent.

Again, note that the anti-crossing between $|X\rangle$ and $|Y\rangle$ increases in width with increasing magnetic field, and that there is a substantial blue-shift of the anti-crossing. The substantial blue-shift of the anti-crossing leads to the following behavior at 2.869 GHz as the magnetic field is increased from 0 G: first, the amplitude decreases as approximately $1/B_0$, then increases as the anti-crossing

shifts away from 2.869 GHz, and finally continues to decrease as $1/B_0$. The different shapes of the ODMR response for case (a) and case (b) of Fig. 2.17 also correspond to the shapes as in the measured data: case (a) appears stretched in the horizontal direction relative to case (b), which appears stretched more vertically, implying a steeper drop-off of signal with increasing magnetic field. The simulations capture this difference in behavior for when B_0 moves from parallel to B_1 to perpendicular to B_1, even though the same set of simulation parameters was used in both cases.

A final point to note is that because the simulations compute and sum up lineshapes for a finite number of nanodiamond orientations with respect to the magnetic field axes, there is some streaking that occurs in the ODMR lineshape at extreme magnetic fields as the individual nanodiamond orientations become resolvable. This is simply an artifact of the computational procedure, and it also shows up in the plots of Fig. 2.18 as "wiggles" at high magnetic fields.

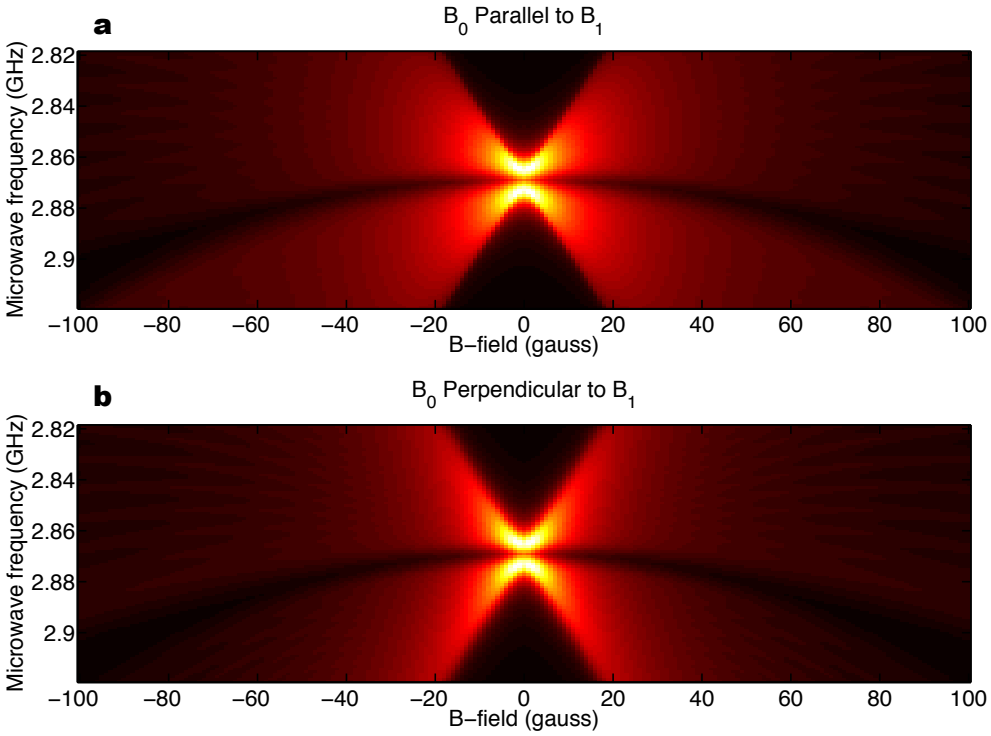

Figure 2.17: Simulated ODMR data, up to ±100 G. (a), magnetic field (B_0) parallel to microwave field (B_1). (b), magnetic field perpendicular to microwave field. Horizontal striations appear at more extreme magnetic fields due to the finite number of nanodiamond orientations simulated.

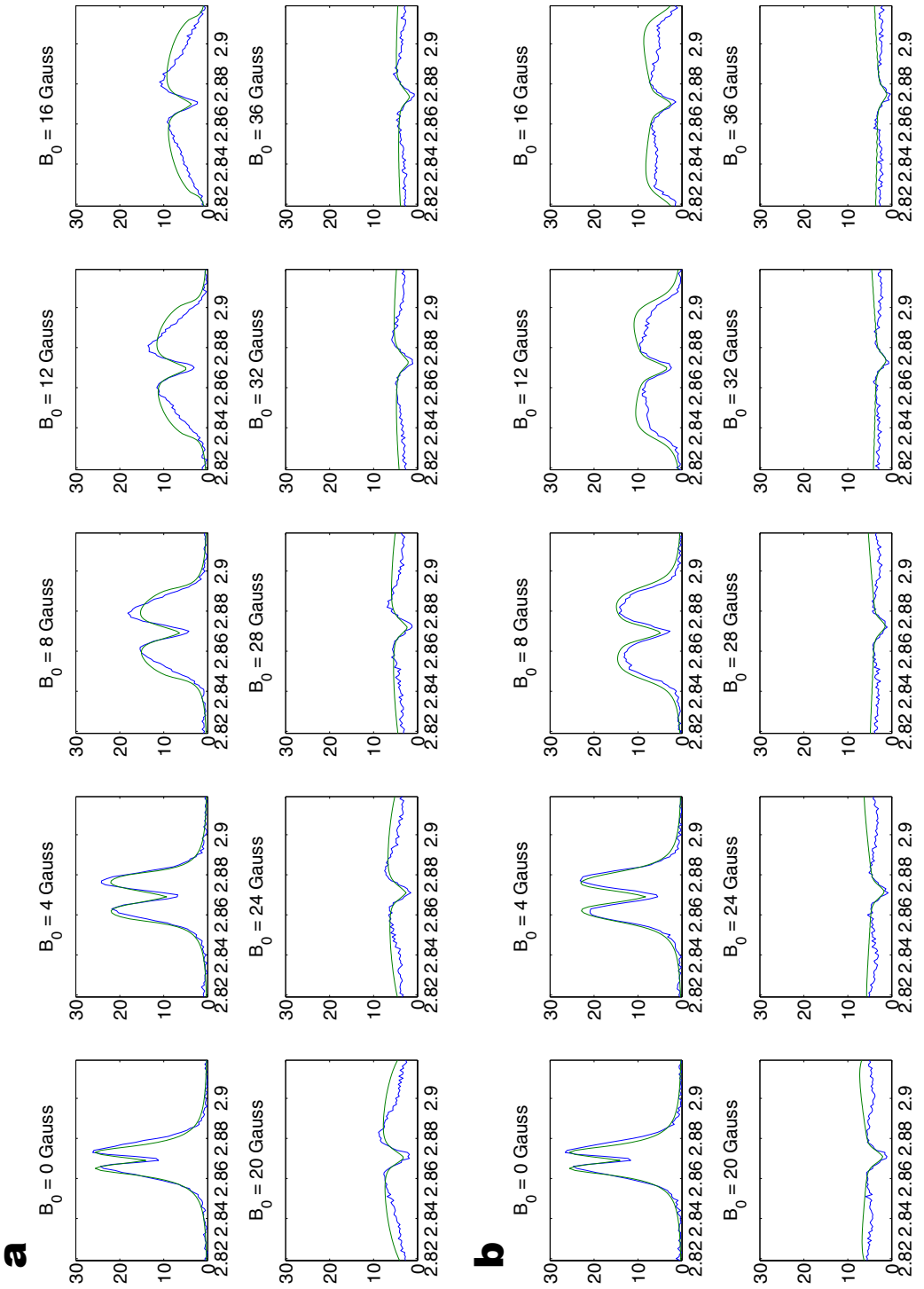

Figure 2.18: Measured ODMR data (blue) compared to simulated (green). **a,** Magnetic field ($\boldsymbol{B_0}$) parallel to microwave field ($\boldsymbol{B_1}$). **b,** Magnetic field perpendicular to microwave field. Horizontal axes represent microwave frequency in GHz; vertical axes represent picoamps of modulated photocurrent per microgram of nanodiamond.

Chapter 3: Imaging Method and Apparatus

Chapter Summary

We start with a general overview of the technique of nanodiamond imaging that includes more technical detail than was present in the introduction. We then go into details of the two imaging systems that were built, including how to generate a field-free line, how to scan the field-free line across the sample, design details of the optical subsystems and custom electronics, and the issues solved by the second system such as enlarging the restricted field-of-view of the first system.

Overview of the imaging technique

Critical to the functioning of nanodiamond imaging are the NV's properties of optically-induced spin polarization and optical spin detection; to summarize from the last chapter, the electronic ground state of the NV is a spin triplet, with a zero-magnetic-field splitting of 2.869 GHz between the $m_s = 0$ and the $m_s = \pm 1$ sublevels (Fig. 2.7). The NV spin is pumped into the $m_s = 0$ sublevel upon optical excitation, because the intermediate singlet states decay preferentially to the $m_s = 0$ sublevel (Fig. 2.8). Furthermore, because the $m_s = \pm 1$ can decay non-radiatively while the $m_s = 0$ decays only radiatively, $m_s = \pm 1$ fluoresces more dimly than $m_s = 0$ (Fig. 2.9). Microwaves resonant with the spin transitions mix the spin sublevels, and by placing a magnetic field along the NV axis (Fig. 2.12a), the ±1 spin sublevels split relative to each other at a rate of 56 GHz T^{-1} (approximately equivalent to the Zeeman splitting of a free electron). In nanodiamond powder, transitions at all frequencies between the two extreme frequencies occur because of the random orientation of individual nanodiamonds with respect to the magnetic field (Fig. 2.12b).

As described in the introduction, nanodiamond imaging is essentially imaging via optically-detected electron spin resonance (ESR). In our particular version of imaging with optically-detected ESR, we make use of a magnetic field-free point (or field-free line) where only those NVs near the field-free point are resonant with a microwave field at 2.869 GHz. After optical pumping of the NV spins into the bright $m_s = 0$ sublevel, the microwaves mix the spin sublevels, causing an observable decrease in fluorescence for those NVs at the field-free point (Fig. 3.1). This decrease in fluorescence is proportional to the nanodiamond concentration at the field-free point. By sweeping the field-free point across an organism (as Fig. 3.2, which demonstrates one way to obtain the imaging point-spread function) and tracking the changes in fluorescence, a quantitative map of the nanodiamond concentration as a function of position is obtained.

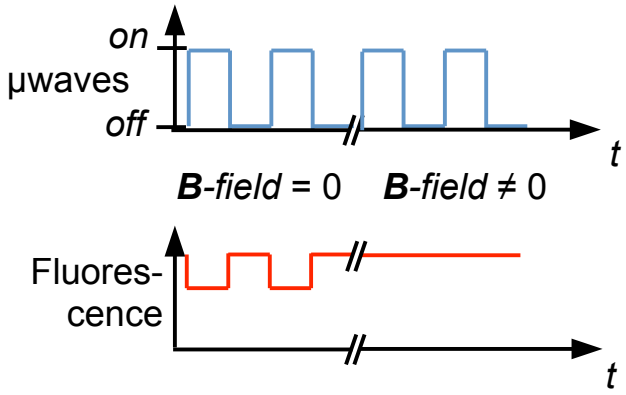

Figure 3.1: Microwave-modulated fluorescence. Under optical excitation, chopping 2.869 GHz microwaves produces a synchronous modulation in fluorescence at the chopping frequency, but only in the absence of a magnetic field.

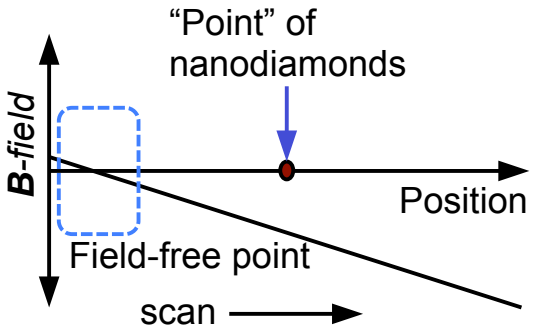

Figure 3.2: Field-free point scan. Scanning a field-free point across a point of nanodiamonds with microwaves on and tracking the fluorescence yields the imaging point-spread function.

To image a 2D slice or a 3D volume of the nanodiamond concentration within an organism, we can scan the field-free point across it in two or three dimensions. Two-dimensional projections of the nanodiamond concentration can be obtained by scanning a field-free line across the sample volume, and projections from different angles can be combined into a 3D image using a standard reconstruction algorithm, as in computed tomography. Forming a 3D image in this way will generally lead to higher SNR in the same measurement time than 3D scanning of a field-free point, because the measurement is multiplexed (i.e., information pertinent to many voxels is sampled at once).

The use of a field-free point or line, as inspired by *x*-space magnetic particle imaging [54], distinguishes this kind of spin resonance imaging from traditional MRI. As described in Chapter 1: Introduction, MRI relies on the coherent precession of

spins, within a magnetic gradient, across the sample volume. In nanodiamond imaging, the 2.869 GHz zero-field splitting of the triplet levels acts as an effective magnetic field directed along the diamond's <111> crystalline axis. The orientation of this effective magnetic field relative to any applied gradient is arbitrary, therefore there is an uncertainty in the precession frequency of the various NV spins. However, the advantage of working at the field-free point is the resonance frequency only depends on the crystal field and is thus independent of the nanodiamond orientation. The gradient that surrounds the field-free point smears out the resonance, but that is acceptable because it does so predictably.

In fact, the first iteration of the nanodiamond imaging concept included a method of imaging very similar to MRI. A gradient would be applied across the whole sample with the precession of the NV spins assumed to be coherent. Applying a $\pi/2$ pulse to convert precession phase into an optically-detectable spin population difference would enable the sampling of the NV-nanodiamond distribution in Fourier space, so an image could be obtained with an inverse Fourier transform. This coherent imaging method could have been achieved with very strong microwave excitation pulses (for broadband excitation) and spin echo sequences that eliminated the inhomogeneous broadening due to the random orientation of the nanodiamonds with respect to the magnetic field. However, such strong microwave fields would only have been practical for the smallest fields of view, for example over a single cell, and we hoped to do organism-scale imaging.

The second iteration of the imaging method was to apply a gradient across the subject, and rather than looking at the response to coherent microwaves at one particular frequency, we would perform an incoherent microwave absorption measurement across a range of frequencies. The NV ensembles at lower magnetic fields would have narrower ODMR lineshapes, and those at higher magnetic fields would have wider lineshapes (Fig. 2.12 offers an explanation for this). By looking at the width of the lineshape, one could infer the location of the nanodiamonds projected into one dimension along the magnetic gradient. If nanodiamonds were present at multiple locations along the gradient, one could look at the overall ODMR signal as a function of frequency and decompose it into a sum of contributions from nanodiamonds at individual locations. By rotating the gradient around the sample in two or three dimensions, the nanodiamond distribution could be reconstructed tomographically. However, this problem is rather ill-posed—the lineshape does not vary significantly with position—and the nanodiamonds that have the widest lineshape are measured with a low signal-to-noise ratio, because the signal scales as 1/(lineshape width).

The third, and current, iteration of the nanodiamond imaging concept incorporates the idea of a field-free point or line. By using a field-free point or line, the raw data shows a close visual correspondence with the actual nanodiamond distribution, so no complicated inversion of the imaging system is needed to have visually useful data. Using a field-free line yields quicker scan times for producing

2D projection images than scanning through the whole volume with a field-free point. Also, due to multiplexing, it yields a higher SNR for the 3D images.

First Apparatus Overview

The different subsystems necessary for the imaging system are thus:

1) A magnetics subsystem that generates and scans the field-free line
2) Optical excitation subsystem
3) Fluorescence detection subsystem
4) Microwave excitation subsystem
5) Signal acquisition, processing, post-processing and display

A schematic overview of the first imaging system is shown in Fig. 3.3, with details presented in the following sections. Briefly, a red LED attached to a current source provides stable optical excitation at 610 nm to 630 nm and generates $\sim$1 W cm^{-2} of red light at the sample. Fluorescence is detected by a single photodiode; note that positional information about the nanodiamonds is completely encoded into the fluorescence intensity and not spatially resolved at the detector. Four permanent magnets in a cylindrical quadrupolar arrangement create a field-free line at the center of a 1 T m^{-1} gradient, for 2D projection imaging along the $\hat{z}$-axis. The line can be shifted relative to the sample via a dipolar arrangement of electromagnets in the x- and y- axes to form images with a 1 cm^2 field of view. The microwaves are modulated at 379 Hz, and the corresponding change in fluorescence is synchronously detected.

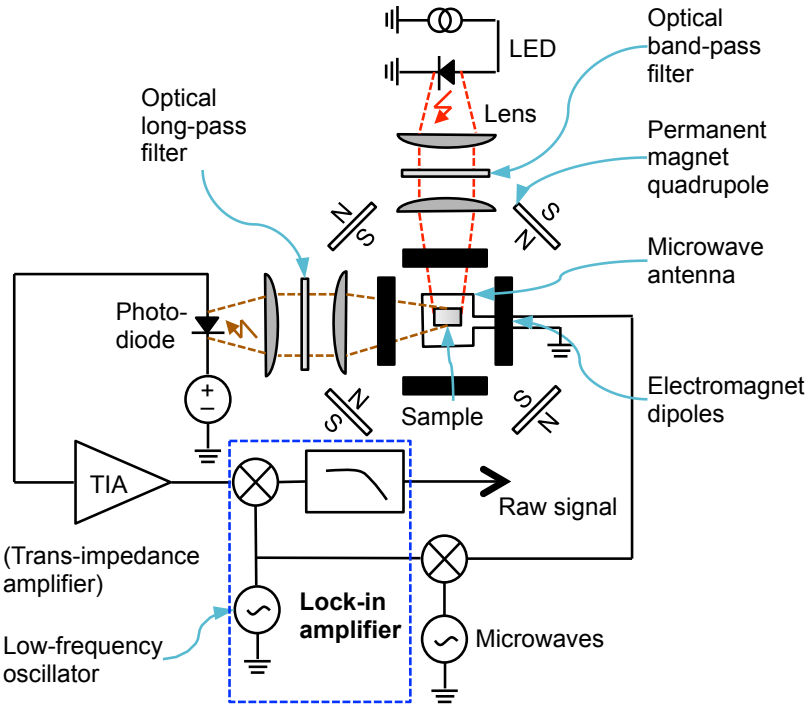

Figure 3.3: A schematic of the nanodiamond imaging system.

Magnetics

The objective of the magnetics subsystem is to create the magnetic null (field-free point or field-free line) necessary for spatially resolving the nanodiamonds, and to raster the null across the imaging system's field of view. A convenient theoretical framework for understanding the magnetic field patterns within nanodiamond imaging is the multipolar expansion, where cylindrical coordinates are used to describe the field-free line, and spherical coordinates are used to describe the field-free point.

The lowest order term that generates a magnetic null is the quadrupole term. Because higher order terms decay more rapidly from the field source, the quadrupole term is a very close representation of the magnetic field across the field of view of the imaging system, and higher order terms are generally not needed to describe the behavior of the imaging system. The dipole term, representing a constant magnetic field, causes the null generated by the quadrupole term to shift across the field of view. We can put this into a more rigorous mathematical framework with the following derivation.

One of the Maxwell's equations is the divergence-free condition of the magnetic field, equivalent to stating the absence of magnetic monopoles:

$$\nabla \cdot \mathbf{B} = 0. \tag{3.1}$$

In a source-free region ($\nabla\times\mathbf{B} = 0$) that is also simply connected, we can define a magnetic scalar potential, $\mathbf{B} = -\nabla\Phi$. When combined with Eq. 3.1, we see that our scalar potential satisfies the Laplace equation:

$$\nabla^2\Phi = 0 \tag{3.2}$$

which in 2D cylindrical coordinates has the solution

$$\Phi(r,\phi) = \sum_{n=-\infty}^{\infty} A_n e^{in\phi} r^n \tag{3.3}$$

for points interior to a cylindrical boundary, and in spherical coordinates has the solution

$$\Phi(r,\theta,\phi) = \sum_{l=0}^{\infty}\sum_{m=-l}^{l} A_{lm} r^l Y_{lm}(\theta,\phi) \tag{3.4}$$

for points interior to a spherical boundary [55]. The Y_{lm} are spherical harmonics. In Eqs. 3.3 and 3.4, n and l refer to the multipole expansion number, where 0 is monopole, ±1 (1) is dipole, ±2 (2) is quadrupole, etc.

As an explicit example, let us consider the quadrupole field in cylindrical coordinates, which corresponds to the field-free line of our imaging system. In our imaging system, the field-free line extends along the $\hat{x}$-axis, so we choose a coordinate system in the $\hat{y}\hat{z}$-plane, where $y = r\cos\phi$ and $z = r\sin\phi$. Taking the $n = \pm 2$ terms of Eq. 3.3, we have

$$\begin{aligned}\Phi_{FFL} = \frac{G}{4}\left(e^{i2\phi}r^2 + e^{-i2\phi}r^2\right) &= \frac{G}{2}r^2\cos 2\phi \\ &= \frac{G}{2}r^2(\cos^2\phi - \sin^2\phi) \\ &= \frac{G}{2}(y^2 - z^2),\end{aligned} \tag{3.5}$$

where we've used the fact that the field must be real and so equal to its complex conjugate to introduce the single real coefficient G, the gradient of the magnetic field magnitude in T m^{-1}. The magnetic field is thus $\mathbf{B}_{\mathrm{FFL}} = -\nabla\Phi_{\mathrm{FFL}} = -Gy\hat{y} + Gz\hat{z}$, and is illustrated in Fig. 3.7b, although rotated 45° with respect to the derivation presented here. Note that the field magnitude increases linearly away from the field-free line:

$$|\mathbf{B}_{\mathrm{FFL}}| = \sqrt{\mathbf{B}_{\mathrm{FFL}}\cdot\mathbf{B}_{\mathrm{FFL}}} = Gr. \tag{3.6}$$

The dipole field is given by the $n = \pm 1$ terms of Eq. 3.3, thus:

$$\mathbf{B}_{\text{dipole}} = -\nabla\left(\frac{B}{2}e^{i\phi}r + \frac{B}{2}e^{-i\phi}r\right) = -B\hat{y}, \qquad (3.7)$$

and of course, without loss of generality, we can consider arbitrary rotations of the dipole field within the $\hat{y}\hat{z}$-plane. In this particular example, the location of the field-free line is the point at which the sum of the dipole and quadrupole fields is zero: $\mathbf{B}_{\text{FFL}} + \mathbf{B}_{\text{dipole}} = \mathbf{0} \Rightarrow y = -B/G\,, z = 0$. Similar results can be obtained for the dipole and quadrupole fields in spherical coordinates.

The design objective of the magnetic field subsystem was to create these quadrupole fields, either in spherical or cylindrical coordinates, and to apply dipolar shift fields. Initially, the plan was to generate both quadrupole and dipole fields using electromagnets, and the design consisted of a pair of coils on each axis ($\hat{x}$, $\hat{y}$, and $\hat{z}$), all of the same size as in Fig. 3.4. Electromagnet coils, used to raster the field-free line across the sample, were wound on aluminum spools machined to interlock with ThorLabs lens tube construction. Coil dimensions were chosen to both interface with the ThorLabs lens tubes used for the optical subsystem and to keep the coils as close as possible to the sample volume (for the strongest magnetic fields), while allowing enough room for a reasonable amount of copper to minimize Joule heating from the electromagnet current. Pieces of Kapton tape were cut using a laser cutter to cover the surfaces of the spools that contact the magnet wire, insulating the wire from the spools and preventing shorts. All electromagnets were wound by hand-turning the spool on a lathe and clamping the wire between two pieces of wood in the tool-stock to tension it. 196 turns of 24 gauge copper magnet wire were wound on each spool in a 14 layer x 14 turns per layer configuration (see Fig. 3.5 for an example). Care was taken to ensure that adjacent turns and layers were neatly packed. Wire thickness was chosen to be thick enough to wind by hand, yet thin enough to keep the current required from the power supplies reasonable and at a voltage that would be readily available. The (cold) resistance of each coil was approximately 2.1 Ohms, such that a readily available high-current 5V power supply could be used to provide current to all coils. Such a power supply could deliver a maximum of about 12 W to each coil.

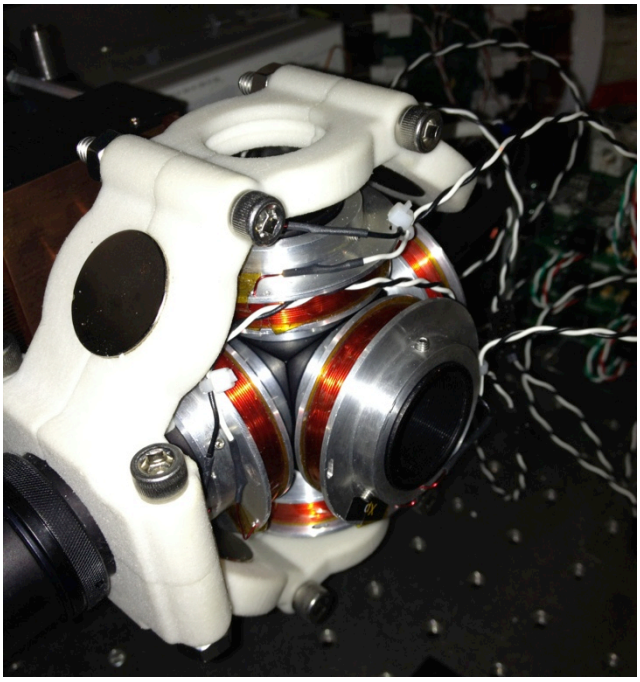

Figure 3.4: An isometric view of the apparatus showing the geometry of the electromagnets and the permanent magnets. Because the permanent magnets in this figure create a field-free line, the pair of coils that sits on the axis of that line is not used. If a field-free point geometry were used, all six coils would be utilized.

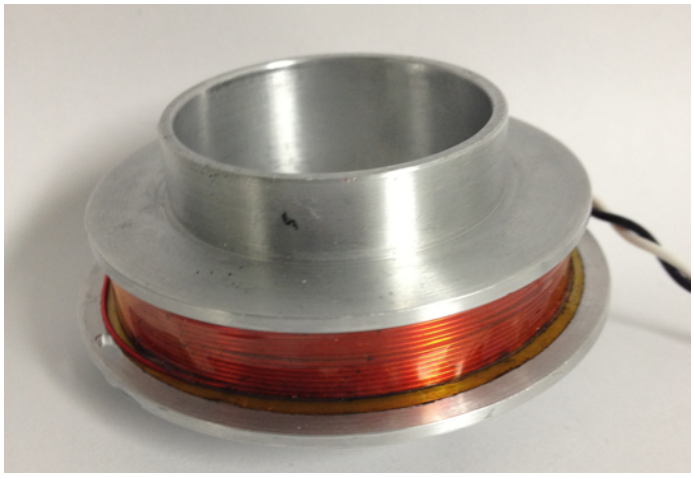

Figure 3.5: A single magnet spool showing a close-up of the windings and the insulating Kapton tape layer.

The coils were far enough away from the sample volume such that the magnetic field had strong dipole and quadrupole moments within the sample volume, but very little octopole moments or above. To check that the designed

electromagnet layout would provide the desired field, a 2D axisymmetric simulation was run in COMSOL for a pair of the designed electromagnets along one axis. Each electromagnet was approximated with one rectangular turn of copper that had the same outline in cross-section as a 14x14 grid of 24 gauge wire, approximately 8 mm x 8 mm. The current density within the one turn was set such that the total current was 196 A, equivalent to putting 1 A of current through 196 (14x14) turns of wire. One simulation was run with the currents oriented in the same sense for each coil (producing a dipole field along the axis) and another was run with the currents oriented in the opposite sense (producing a spherical quadrupole field). The mesh was refined sufficiently in the region corresponding to the sample volume for accurate interpolation on a Cartesian grid.

The results of the simulation are plotted in Fig. 3.6. Throughout the sample volume, the on-axis magnetic field (having only an on-axis component due to symmetry) created from the dipolar current configuration (equal currents running with the same sense through each coil) is roughly constant: it varies from 20.5 G A^{-1} to 22 G A^{-1}, with the deviation due to higher-order multipole terms. The quadrupolar current configuration produced a magnetic field that increased (roughly linearly) in magnitude in every direction outward from the central null, located at the center of the sample volume. The components of the field correspond to those of $\mathbf{B}_{\mathrm{FFP}} = G_0(x/2, y/2, -z)$, with G_0 = 14 G A^{-1} cm^{-1} (at least close to the central null, where terms of higher order than the quadrupole are negligible).

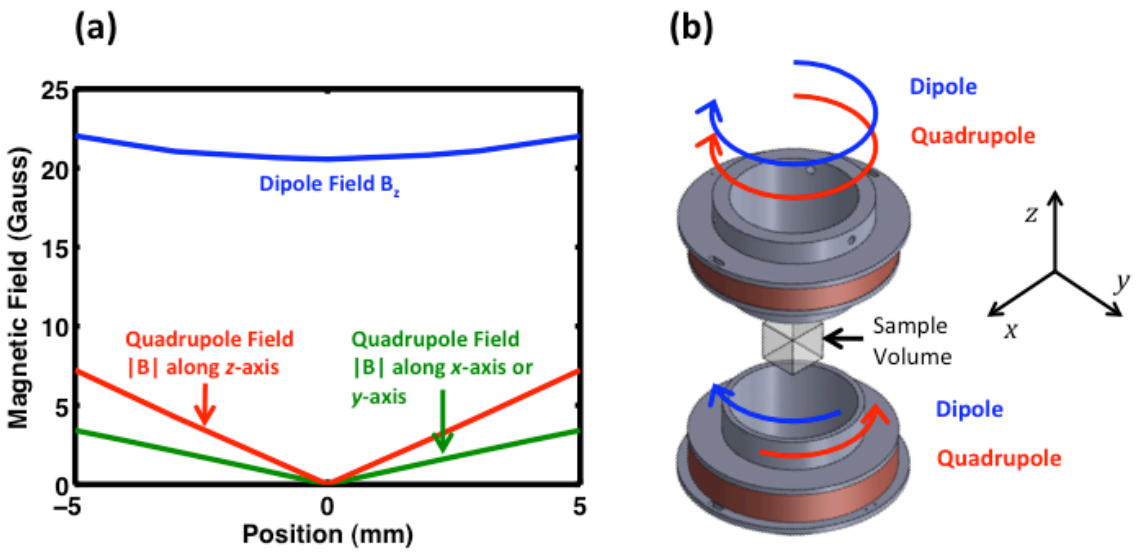

Figure 3.6: Magnetic field between a pair of electromagnets. (a) A plot of the dipole field along the axis of a pair of electromagnets (current flowing in the same sense in each coil), across the extent of the sample volume. Also plotted is the norm of the quadrupole field (current flowing in opposite sense in each coil) along the coil's axis and perpendicular to it. The perpendicular component is one-half the axial component. (b) The pair of electromagnets relative to the sample volume.

During the first imaging experiments, it was discovered that the spatial resolution was not as high as expected given the strength of the magnetic field gradient. This was due to inhomogeneous broadening of the NV spin transitions caused by strain in the nanodiamonds. Retrofitting the apparatus with permanent magnets increased the strength of the magnetic field gradient, thereby increasing the spatial resolution. (Because the permanent magnets were used to create the quadrupolar magnetic field, the entire capacity of electromagnets was used to create the dipolar shift fields.) A magnetic field-free line along the $\hat{x}$-axis was generated by four 1"Ø x 3/8" neodymium magnets (K&J Magnetics SD06-OUT) as in Figs. 3.7 and 3.4. Note that due to the 45° rotation of the permanent magnets relative to the electromagnets (chosen so the permanent magnets do not block the optical system), the electromagnets along the $\hat{y}$-axis move the field-free line along the $\hat{z}$-axis and vice versa. The white arms were designed in SolidWorks, and they are divided into four pieces across two mirror planes to facilitate insertion and clamping of the permanent magnets as well as clamping to the lens tube system. The arms were fabricated with a 3D printer via a layer-by-layer method of spraying water onto a mixture of cornstarch and Plaster-of-Paris, and they were subsequently impregnated with epoxy to increase durability.

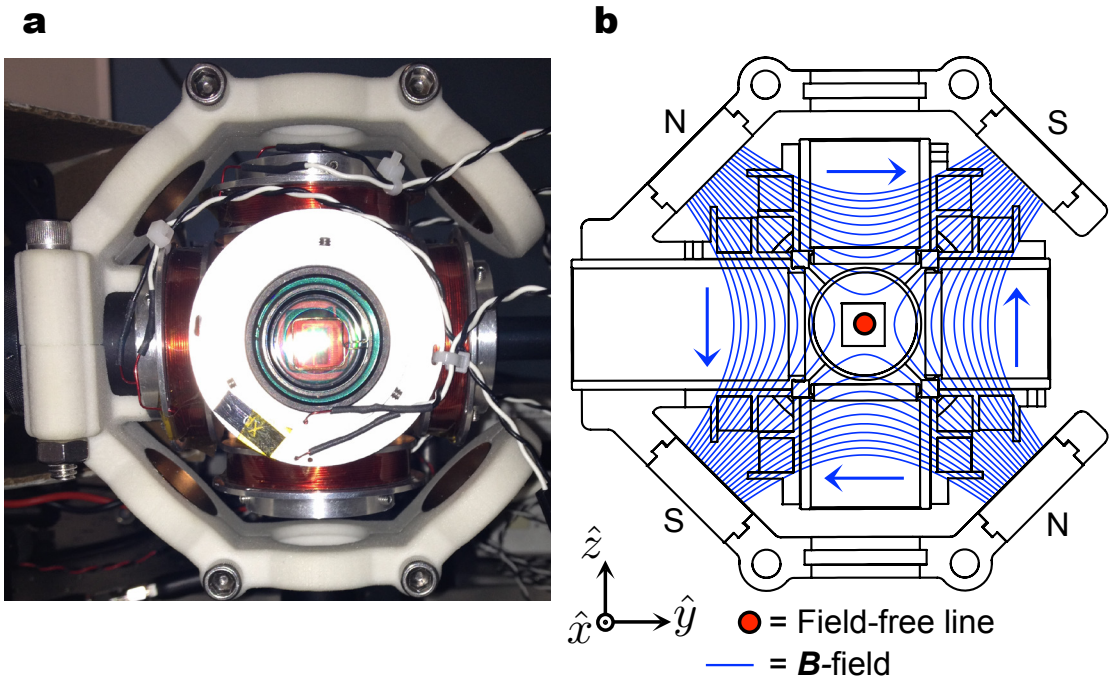

Figure 3.7: Nanodiamond imaging apparatus. **a,** Photo of apparatus. Permanent magnets are held by the white arms; electromagnet coils (copper wire) are visible as well. **b,** cross-sectional drawing of apparatus showing orientation of permanent magnets. The square in the middle is the 1 cm x 1 cm field of view.

An experiment was carried out to verify the strength of the permanent magnet quadrupole gradient. The field-free line (FFL) extended along the $\hat{x}$-axis, and the z-component of the magnetic field, B_z, was measured at several points along the $\hat{y}$-axis with a gaussmeter. Similarly, the y-component of the magnetic field, B_y, was measured at several points along the $\hat{z}$-axis. The results, depicting both $|\partial B_z/\partial y|$ and $|\partial B_y/\partial z|$, are shown in Fig. 3.8. The measurements were meant to extend across the imaging system's field of view in both dimensions perpendicular to the FFL. Across all measurements, the average gradient was 94 G cm^{-1}, or 0.94 T m^{-1}.

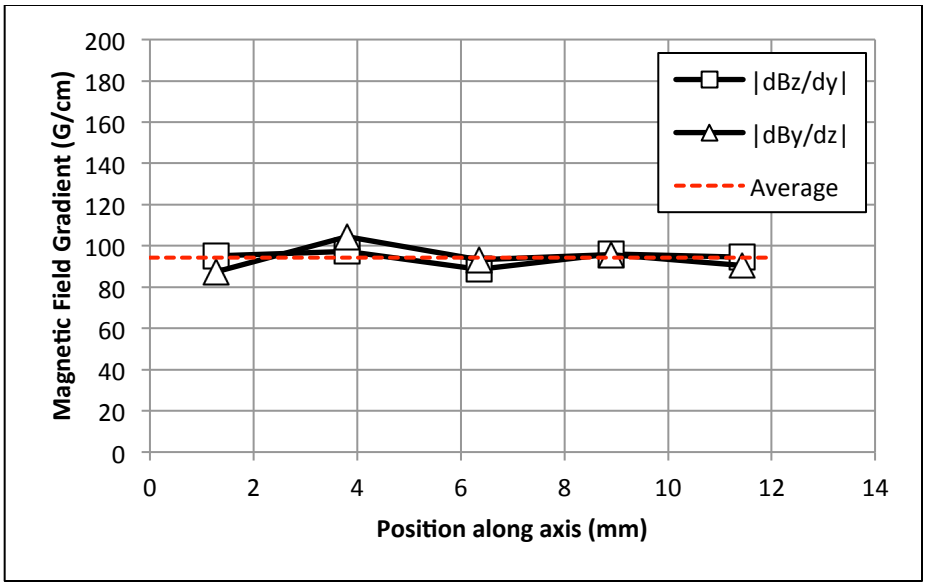

Figure 3.8: Results of the measurement of magnetic field gradients $|\partial B_z/\partial y|$ and $|\partial B_y/\partial z|$ along the $\hat{y}$- and $\hat{z}$-axes, respectively, for the permanent-magnet field-free line geometry. The field-free line extends along the $\hat{x}$-axis. The average gradient strength is 94 G cm^{-1}, or roughly 1 T m^{-1}. The middle measurement point corresponds roughly to the coordinate origin, or the center of the imaging system's field of view.

Note that it may be desirable to have an adjustable magnetic gradient, which could be accomplished with permanent magnets by adjusting the distance from the magnets to the sample, or could also be implemented with only electromagnets by varying the strength of the quadrupole term. An adjustable gradient would enable imaging with a variable spatial resolution. This would be useful for rapidly searching within the field of view for isolated points of nanodiamonds, for example by the method of bisection. That is, if a small isolated spot(s) of nanodiamonds is known to exist, the field of view can be divided into four pixels (for 2D imaging) or eight voxels (for 3D imaging). The pixel or voxel producing the highest signal is further divided, and this process is repeated. In a field of view with N pixels or voxels, the scanning time to find a single pixel/voxel containing nanodiamonds is reduced from N to $4 \log_4 N$ for 2D imaging or $8 \log_8 N$ for 3D imaging. For practical applications, a significant number of the pixels or voxels may contain nanodiamonds. To find the maximum potential speed-up at an arbitrary level of image sparsity, replace N in the expressions above by the fraction N/N_{diamond}, where N_{diamond} is the number of pixels or voxels containing nanodiamonds.

Optics

In the first imaging system, optical excitation was provided by a heatsink-mounted red LED (Luminus CBT-120, HK flux bin, R4 wavelength bin—619 to

623 nm) that was driven at 18.0 A through a 10 mH inductor (Hammond 195J20). (Note the NV optical transition saturates around 10^6 W cm^{-2} [14], so for this imaging technique the fluorescence will effectively scale linearly with the excitation intensity.) The excitation light was collimated with an aspheric condenser (Thorlabs ACL2520-A) and band-pass–filtered (Semrock FF01-615/45-25) to remove light that overlapped with the NV fluorescence, and then focused onto the sample with a lens (Thorlabs LA1422-A). (See Fig. 3.17 for an example of the excitation optics used for the second imaging system; they are similar to those used for the first system, which are not shown.) All optics were placed in Thorlabs lens tubes, and black-flocked paper (Protostar FBR-01) covered all exposed surfaces of the lens tube interiors to minimize the propagation of scattered out-of-band light through the interference filters. In order to ensure that the bulk of the LED excitation occurred at energies above the NV's zero-phonon line, we plotted the LED output as a function of current from 1 A to 18 A in Fig. 3.9. This plot was used to choose the proper band-pass (BP) filter for excitation and long-pass (LP) filter for fluorescence emission. Filter data was obtained from Semrock and took into account the nonparallel nature of the rays, even after the collimating lens, due to the finite source size.

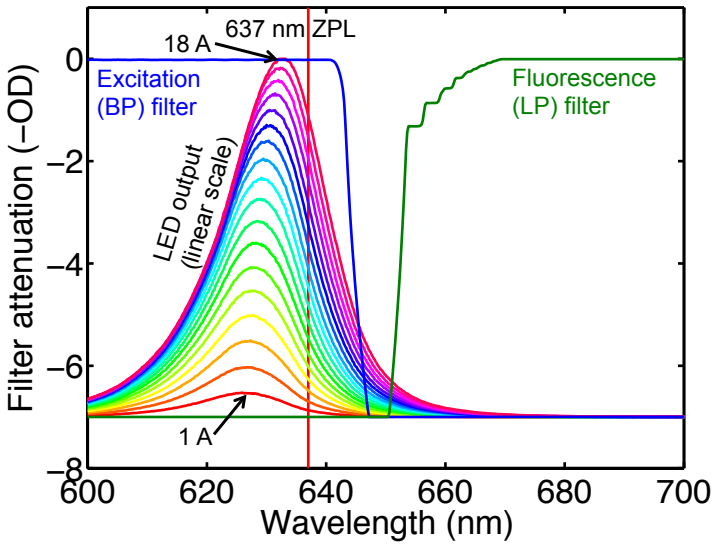

Figure 3.9: Plot showing the LED emission versus current, on a linear scale, from 1 A to 18 A. The 637 nm zero-phonon line (ZPL) of the NV is indicated (compare with room-temperature NV absorption spectrum in Fig. 1.4b). The filter attenuation data was obtained from Semrock and is the average log-transmission for the chosen filters, averaging over an 8° half-angle for the excitation and a 20° half-angle for emission.

The detection stage must record changes in fluorescence across the NV fluorescence band throughout the imaging procedure. Any combination of optical

elements may be used with the goal of maximizing light collection from the NV fluorescence and minimizing collection of all other light. In the first imaging system, fluorescence emission was collected at a 90° angle to the excitation, providing some geometrical isolation from the excitation. Light was collected through a first filter stage consisting of a condenser lens (Thorlabs ACL2520-B), a long-pass filter (Semrock LP02-664RS-25), and a second condenser lens (Thorlabs ACL2520-B) focused down onto an adjustable iris. This was followed by a second filter stage of the same lens/filter/lens combination, and finally focused onto a 10 mm x 10 mm Si photodiode (Hamamatsu S2387-1010R), reverse-biased at 15 V. (See Fig. 3.18a for a drawing of the fluorescence collection optics used in the second system; this is similar to the collection optics used in the first system, except it is only a single stage, and the photodiode amplifier is built into a shielded enclosure.) A front-end preamplifier was built within the lens tube directly behind the photodiode, utilizing a low-noise JFET operational amplifier (Analog Devices ADA4627-1) in a standard transimpedance configuration as in Fig. 3.10a and b. A feedback network of 10 MΩ in parallel with 10 pF was used. With this preamplifier, the detection system was shot-noise limited.

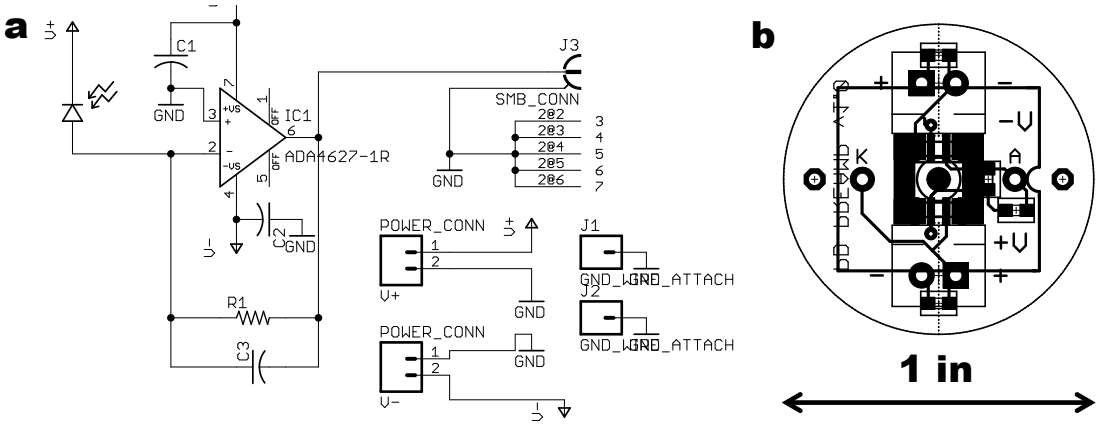

Figure 3.10: Photodiode circuit schematic and board. (a), standard transimpedance configuration with low-noise JFET input op-amp, Analog Devices ADA4627-1. (b) circuit board layout on Ø1" circle used to fit inside lens tube. Large black rectangle is photodiode outline; photodiode has a 10 mm x 10 mm active area.

In general, the fluorescence detector can be any sort of photoelectric detector, such as a photodiode operating in linear or avalanche mode, or a photomultiplier tube. It must introduce an acceptably low amount of system noise, its bandwidth must be great enough to encompass the measurement bandwidth, and the dynamic range must be large enough to measure the small signal modulation on the large DC background with high fidelity. A reverse-biased photodiode is ideal because it satisfies all three of these criteria. Although only a single pixel detector is necessary,

a multi-element detection system could provide extra information about the location of the nanodiamonds that could be used during image reconstruction.

The large DC background consists of excitation light that makes it through the detection stage filters, as well as tissue autofluorescence and fluorescence from imaging system components. Because we are attempting to detect a small time-varying signal on top of this DC background, we must both minimize the background and make it as stable as possible. Minute fluctuations in the background at the same frequency as the microwave modulation (for example from sample vibration) will appear as an additive noise component on top of the signal. Note that in a properly engineered system, the dominant source of noise will be shot noise from the NV fluorescence and background light.

In general, LEDs are preferable to lasers as an excitation source, because the amplitude fluctuations of lasers are significantly larger than those of a current-controlled LED, and these amplitude fluctuations cause variations in the large DC background. LEDs are also much safer to work with than lasers, especially when dealing with optical powers of several watts. However, lasers do offer some advantages. Due to the coherent nature of laser light and the ability to focus laser light to a point, it is easier to couple laser light into fiber optics for light transmission than it is for LED light. It is also easier to send laser light through an interference filter, because the light rays can be made parallel, though the output of a laser is generally monochromatic. The amplitude noise can be dealt with: methods have been developed, such as [56], for subtraction of the fluctuations in laser amplitude by use of a reference photodetector. A feedback loop stabilizes the gain of the subtraction circuit without limiting the bandwidth of the subtraction itself. The subtraction technique can achieve shot-noise–limited performance and is compatible with lock-in measurement techniques.

Electronics

The fluorescence signal must be captured and digitized so it can be processed into an image. In the first system, the output of the photodiode preamplifier was AC-coupled to the input of a low-noise voltage preamplifier (Stanford Research Systems SR560), with the high-pass filter cutoff set at 100 Hz and the low-pass filter cutoff set at 1 KHz. Gain was set to 10^3. The output of the SR560 was digitized at 250 KHz by a data acquisition (DAQ) card (National Instruments PCIe-6321).

A key part of the electronics in a nanodiamond imaging apparatus is the microwave subsystem. In general, the microwave subsystem consists of a microwave generator, possibly a modulator, a radiator, and any necessary tuning or matching circuitry. High average and instantaneous powers and low phase noise are desired traits of a microwave generator, but these are generally only required if coherent pulsing schemes are to be used, as described in Chapter 5: Discussion. For the first system, microwaves were generated by an analog signal generator (Agilent E8257D) set to 2.869 GHz at +24 dBm output power. The microwaves were

chopped at 379 Hz by a PIN switch (Mini-Circuits ZASWA-2-50DR+) controlled by a digital output of the DAQ. Microwaves were transmitted to the sample via a ~12 mm x 12 mm square loop of 24 AWG solid copper wire, positioned around the perimeter of the sample.

There are other methods of delivering the microwaves to the sample, which may be necessary for larger fields-of-view, when a loop of wire becomes too inductive to pass much current at microwave frequencies. A waveguide or coaxial cable may be used for this, with some kind of radiating structure or antenna at the end, such that the sample sees the far field, e.g. approximating a plane wave. A resonant structure or cavity could be employed to enhance the microwave field. Matching circuitry can be used to match the radiating or resonant element to the impedance of the waveguide or coax.

Electromagnet power supply

A custom programmable bipolar power supply was built to power the first system's electromagnets, and was controlled with the output of an analog output board (National Instruments PCI-6722). Because there are 6 coils that must be driven independently, the power supply had 6 independent voltage-to-current amplifiers, each with a gain of 1 A V^{-1}. The schematic for a single channel is shown in Fig. 3.11. An input BNC connector, X1, connects to the analog output board. Resistor R2 and capacitor C1 form a deglitching circuit to remove sudden jumps in the input voltage. Op amp IC1 tracks the input voltage and adjusts the gate voltage of MOS transistors Q1 and Q2 to provide the proper amount of current to the coil. Resistor R1 is a four-terminal current-sense resistor that senses the current through the coil. Its voltage is amplified by instrumentation amplifier IC2, with a gain of 20 set by R3. The output of IC2 is fed back to the negative input of IC1, to complete IC1's feedback circuit. Capacitor C2 was meant to provide a zero in the feedback network to increase stability, but it turns out it was actually stable without it (and unstable with it) as the phase shifts could not be precisely estimated during the design phase.

Note that when building multichannel magnet power amplifiers like the one shown in Fig. 3.11, many considerations need to be taken into account (this was the third design iteration; these considerations were learned by making mistakes on the first two iterations). First, the resistor R1 must be small for low power dissipation (in this circuit, a 50 mΩ resistor is used)—if the resistor heats up, its resistance changes, effecting variations in the circuit gain of 1 A V^{-1}. For this reason it is also important to choose a resistor with a low temperature coefficient of resistance. Finally, because the resistor is small, it needs to be a four-terminal resistor, so its voltage can be accurately sensed by high-impedance electrodes.

Other considerations relate to the ability to find high-current power supplies at a given voltage. The gauge of wire to wind the magnets should be chosen based on the highest current supply available—higher current means a lower gauge can be

used, and fewer windings are necessary. However, this necessitates high currents running through the traces on the circuit boards, so the traces must be made both thick and wide (see Fig. 3.12 for the board layout of the amplifier; 2 oz. copper was used for the traces). The high currents running through each channel mean that star grounding is especially important, i.e., all the channels must be essentially independent and grounded together at only one point, otherwise they start to interact. Note to make a six-channel amplifier, three boards like the one in Fig. 3.12 were stacked together, and an enclosure was built to support them all, including a fan for forced-air cooling.

Finally, care must be taken to ensure that the amplifier circuit is stable with respect to high-frequency ringing and oscillation. This is because the coil acts as an inductor and resistor in series; at high frequencies, the impedance of the inductive component dominates, causing the current through the coil to lag the voltage by 90°. If the inductance is large enough, this 90° phase shift will combine with the op-amp's internal 90° phase shift at unity gain, turning negative feedback into positive feedback and causing the op-amp output to oscillate. One may object to this analysis by stating that the phase shift internal to the op-amp is due to a capacitor, which has the opposite sign as the phase shift due to an inductor, so the phase shifts should cancel and no oscillation should be seen. However, since feedback is taken off the current through the coil, and the current lags the voltage, both phase shifts are phase lags and they add together.

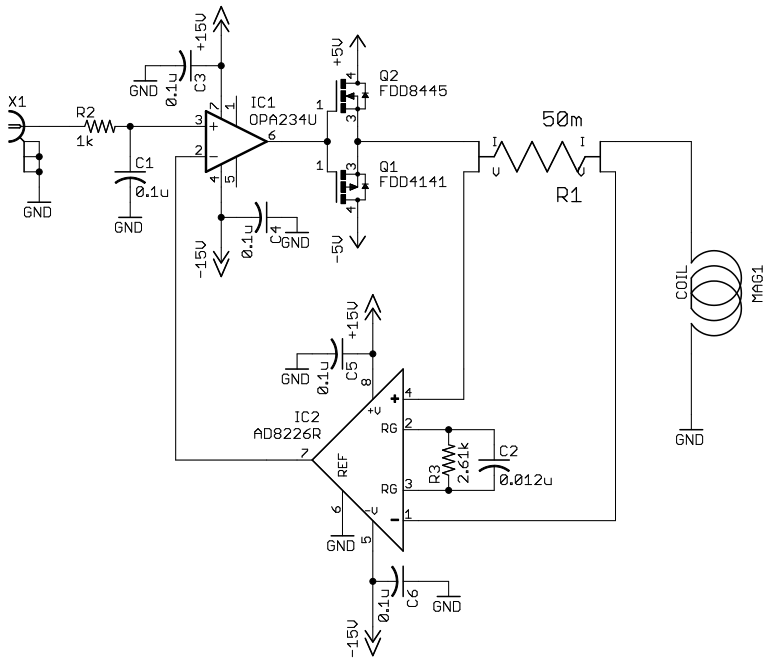

Figure 3.11: Bipolar operational power supply for control of a single magnet current. Provides 1 amp output per volt input.

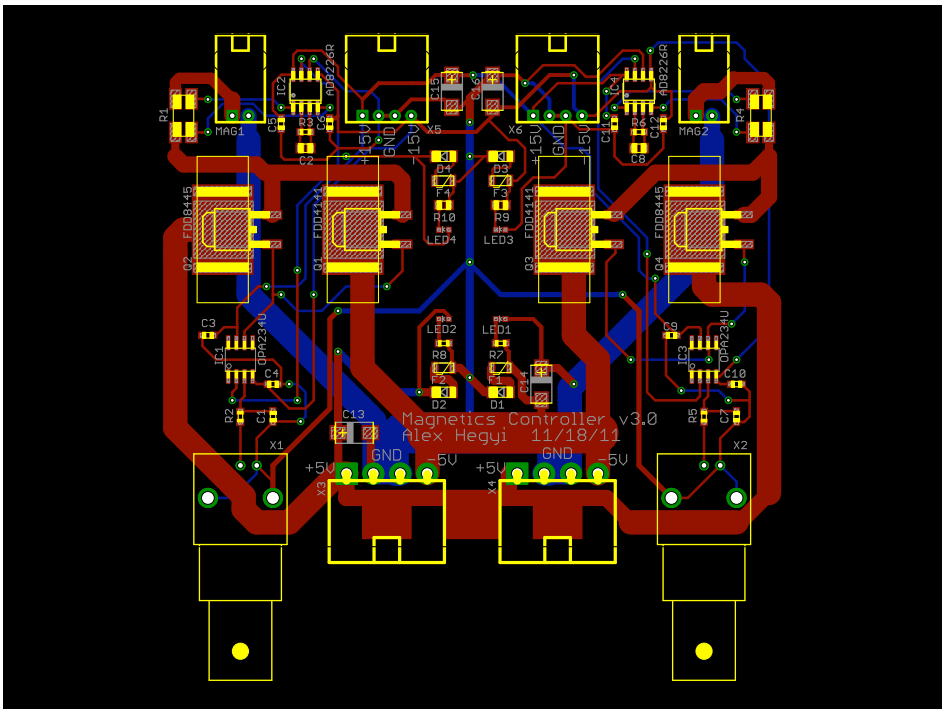

Figure 3.12: Circuit board layout for bipolar operational power supply.

Signal processing

The measurement software was written in LabVIEW. It generates an image by raster-scanning the electromagnet current, thereby moving the field-free line across the field of view, to measure image intensity across a grid of points. At each point in the raster scan, the software executes the following sequence: it samples the output of the low-noise voltage preamplifier at 250 KHz, while chopping the microwaves at 379 Hz. (The change in signal from turning the microwaves on and off is on the order of 0.1%.) Data is recorded for a specified time τ_{meas} and then passed through a series of digital filters: an elliptic 5th order band-pass with a 310 Hz lower cutoff and 450 Hz upper cutoff that attenuates signal far from the modulation frequency, followed by an elliptic 5th order band-stop with a 55 Hz lower cutoff and 65 Hz upper cutoff and an elliptic 5th order band-stop with a 115 Hz lower cutoff and a 125 Hz upper cutoff to suppress 60 Hz/120 Hz line noise. The signal is then digitally mixed with cosine and sine waves with the same frequency as the microwave chopping frequency (379 Hz), to obtain the signal's X and Y (or in-phase and quadrature) components, respectively. Six copies of the resultant signals are concatenated and then filtered by a 4th order IIR Butterworth low-pass filter with a cutoff frequency of $1/(2\tau_{meas})$ Hz, pass-band ripple of 1 dB, and stop-band attenuation of 60 dB. The concatenation is to account for the rise-time of the filter, and care is taken to ensure that the phase of each signal to be concatenated is the same at its beginning and end. The X and Y components are combined into a polar representation of the signal (i.e., R and θ), and the last N samples of each signal are

averaged ($N = \tau_{meas} * 250$ KHz) to obtain the image intensity at a particular field-free line location. The process is repeated for each point in the image.

New apparatus vs. old apparatus

We describe the second iteration imaging system here, which was built to overcome the limited field of view of the first imaging system. The first imaging system had a 1 cm x 1 cm field of view and scanned a field-free line over that field of view using electromagnets on both axes. For the new system, we included the ability to scan over an arbitrary length in one dimension and up to 3 cm in another dimension.

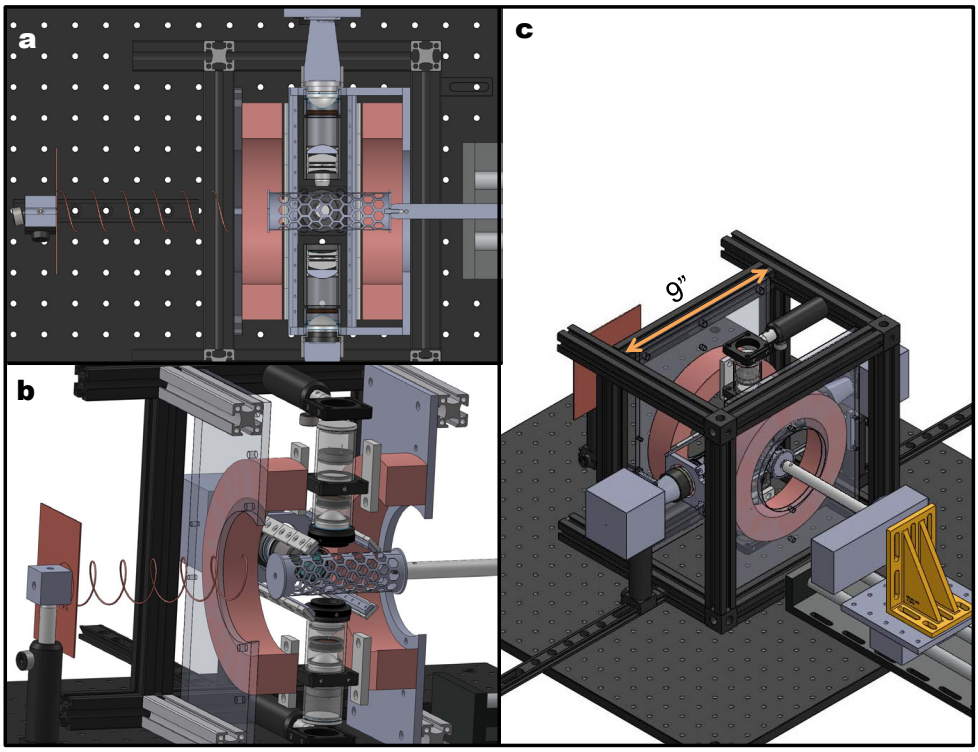

Figure 3.13: Second apparatus design. (a) Top view cutaway. (b) Ortho view cutaway. (c) Ortho view 2.

The imaging system as designed is shown in Fig. 3.13. A photograph of the new imaging system as built is shown in Fig. 3.14 with a corresponding schematic diagram in Fig. 3.15. A magnetic field-free line is generated along the $\hat{z}$-axis by a cylindrical quadrupolar orientation of permanent magnets (K&J Magnetics BX082CS-N/P), as in the right of Fig. 3.14, with a gradient strength of 1 T m^{-1}. To achieve a larger field of view, the new system scans the sample in the $\hat{x}$ direction (relative to the field-free line) using a stepper-motor–driven translation stage (Produstrial 125943), and electromagnets that are larger and more powerful than in

the first system scan the field-free line in the $\hat{y}$ direction relative to the sample. In addition, a stepper-motor–driven rotation stage (Produstrial 124622) controls the sample rotation about the $\hat{x}$-axis to obtain 2D projection images from various angles.

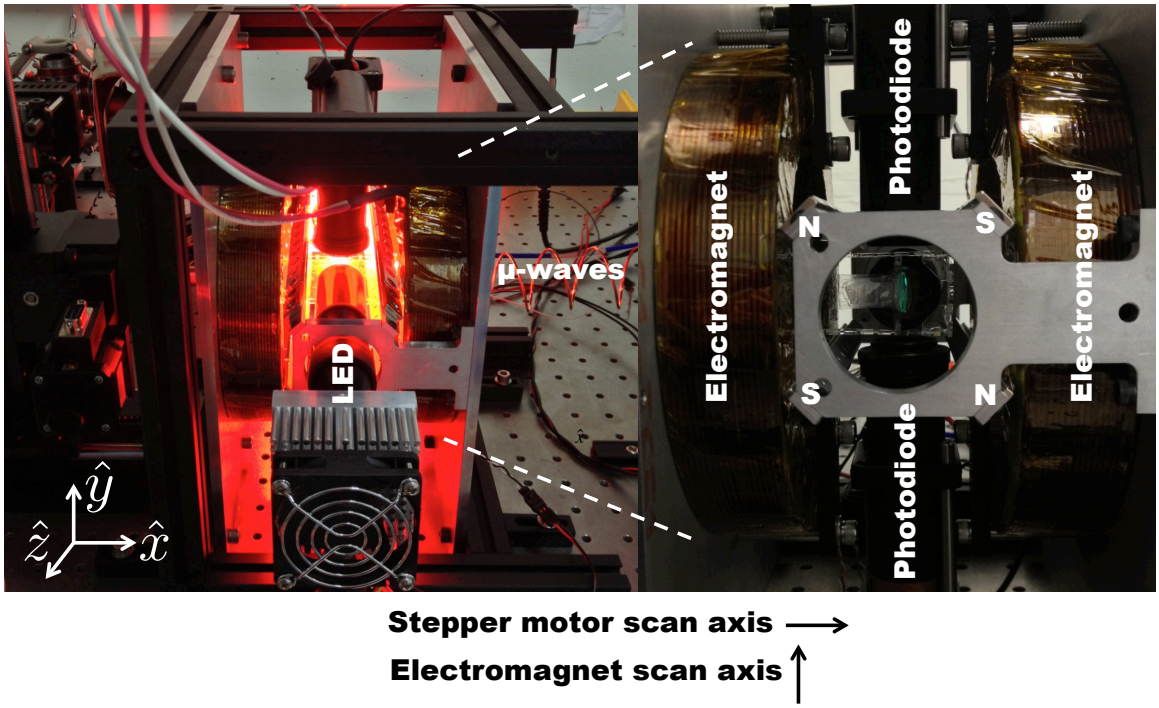

Figure 3.14: The new imaging system left, with LED on, and close-up with LED removed looking down the axis of the field-free line, right. The field-free line exists along the $\hat{z}$-axis, at the center of the four permanent magnets indicated on the right-side close-up. A stepper motor translation stage scans the sample across the field-free line in the $\hat{x}$ direction while the electromagnets scan the field-free line across the sample in the $\hat{y}$ direction. The LEDs and microwaves excite the NVs and the fluorescence is collected via the photodiodes, oriented along $\pm\hat{y}$.

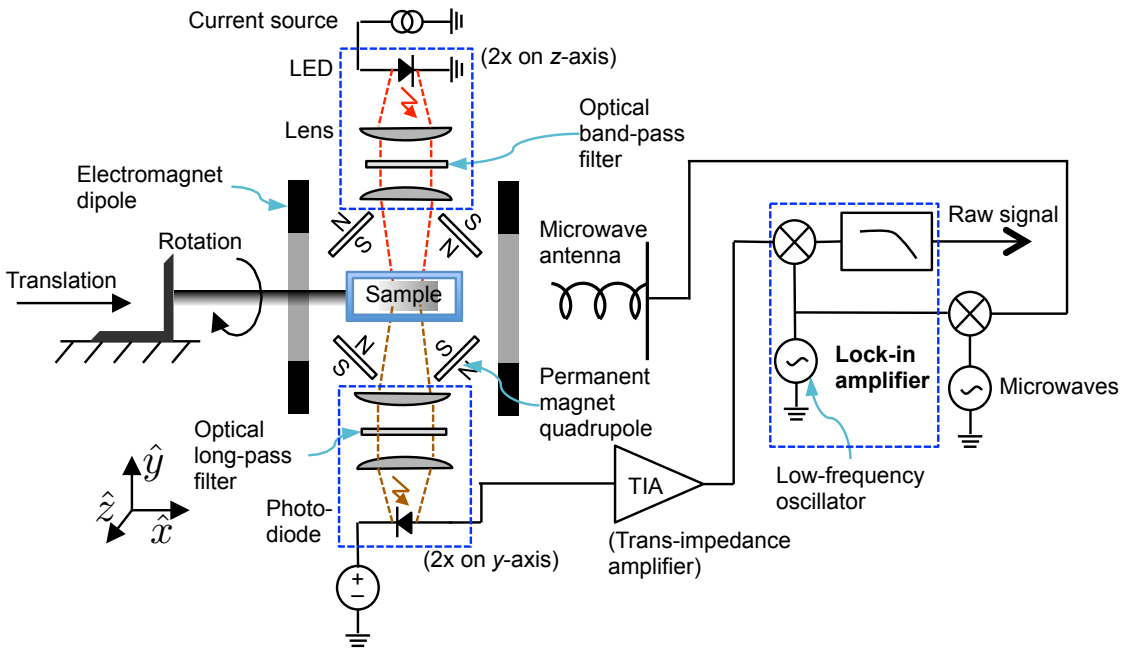

Figure 3.15: Schematic of the new imaging system. Note that there are two LED subsystems, one on either side of the sample along the $\hat{z}$-axis, and two photodiode subsystems, on either side of the sample along the $\hat{y}$-axis. The photocurrent from the photodiodes is amplified by a transimpedance amplifier, and a lock-in-type measurement system modulates the microwaves and synchronously detects the changes in photocurrent (i.e., NV fluorescence) as the sample is scanned in the $\hat{x}$ direction and the field-free line is scanned in the $\hat{y}$ direction.

Compared to the first imaging system, there are many improvements in the magnetics. First, the field-free line is generated by four lines of permanent magnets that extend 7" along the $\hat{z}$-axis with orientation as shown on the right of Fig. 3.14. This extended the length of the field-free line relative to the first system, in which it was generated by four 1" disc magnets in a similar orientation. With a longer field-free line, the point-spread function of the imaging system is less sensitive to the position of a point of nanodiamonds along the $\hat{z}$-axis. Second, the size of the electromagnets was significantly increased and they were placed outside of the permanent magnets, rather than vice versa. By moving the electromagnets further from the field of view, high order multipole terms are attenuated and the field generated by the electromagnets more closely approximates a dipole (constant) field. Although the dipole field points along the axis between the electromagnets (the $\hat{x}$-axis), as one deviates along the $\hat{z}$-axis from $z = 0$, the radial component from the electromagnets (i.e., the component of the field projected into the $\hat{y}\hat{z}$-plane) becomes non-zero. As the field-free line is scanned along the $\hat{y}$-axis, this radial component of the dipole field causes the field-free line to decrease in length, or collapse, about the $\hat{x}\hat{y}$-plane. It is important that the field-free line can be scanned

across the full field of view without collapsing near the periphery, because the collapse of the field-free line (or equivalently, the radial component of the electromagnet field) degrades the resolution of the point-spread function near the periphery of the field of view.

To verify that the field-free line could be scanned sufficiently across the field of view without collapsing, a simulation of the magnetic field magnitude was run as a function of electromagnet current. The results (at 3 A electromagnet current) are plotted in Fig. 3.16. In panel (a), we show the magnetic field magnitude every 5 mm along the $\hat{y}$-axis. The 1 G (0.0001 T) field contour is plotted in red and shown to extend across the sample volume. Although the line starts to collapse as it is scanned along the $\hat{y}$-axis, it still covers the full field-of-view of the imaging system. A contour plot of magnetic field magnitude is shown in panel (b), in the $\hat{x}\hat{y}$-plane.

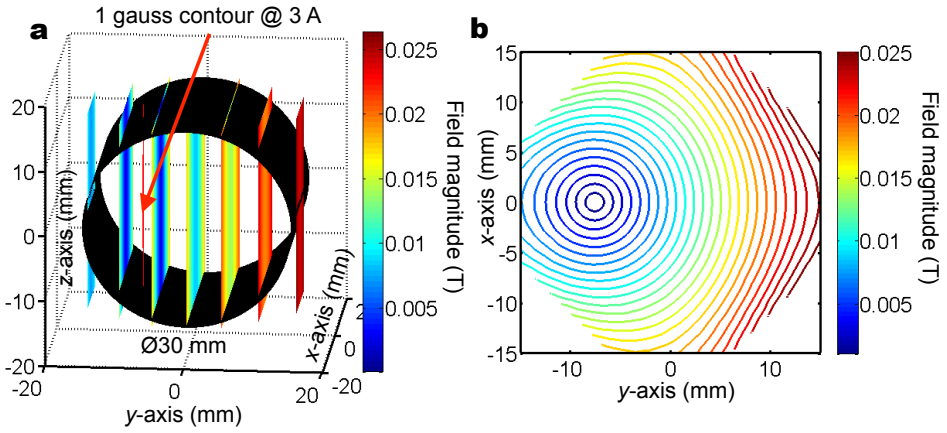

Figure 3.16: Field-free line of Imaging System 2, shifted along $\hat{y}$-axis by 3 A in electromagnets. (a), Black cylinder is 30 mm in diameter and represents volume over which field-free line must be rastered without decreasing in length. The 1 gauss contour is shown in red. This contour decreases in length at higher electromagnet currents, yet still manages to extend across the 30 mm diameter field of view. (b), 2D contour plot of field magnitude at $z = 0$.

The electromagnets were custom-ordered from Custom Coils, Inc. They are wound from 14 AWG square wire and are self-supporting, with a resistance of 1 Ω to take full advantage of the power available from two 20V/20A Lambda EMI BOS/S bipolar operational power supplies, one for each coil.

The second imaging system's optical excitation is provided by two LEDs (Innovations in Optics, 2900A-100-16-F4-N-N LumiBright TA Taper with 22° half angle far field, 12 mm x 12 mm output aperture, 16 die from Bin F4; 615-620 nm, no diffuser and no photosensor), one on either side of the sample and oriented along the $\hat{z}$-axis. The LED excitation optics and excitation spot are shown in Fig. 3.17. Each optical train provides ~2 W optical excitation over a ~12 mm wide by ~25 mm

high area, after collimating (ThorLabs ACL2520-A 20 mm focal length aspheric lens), band-pass filtering (Semrock FF01-615/45-25, 615/45 nm BrightLine® single-band bandpass filter) and focusing through a series of spherical and cylindrical lenses (ThorLabs LA1027-A, LJ1695RM-A, and LK1431RM-A, or f = 35 mm spherical, f = 50 mm cylindrical, f = -75 mm cylindrical, respectively). The axes of the cylindrical lenses are crossed to form the rectangular excitation spot. The lens tube has a threaded section to adjust its length, in case different focusing of the excitation spot is desired.

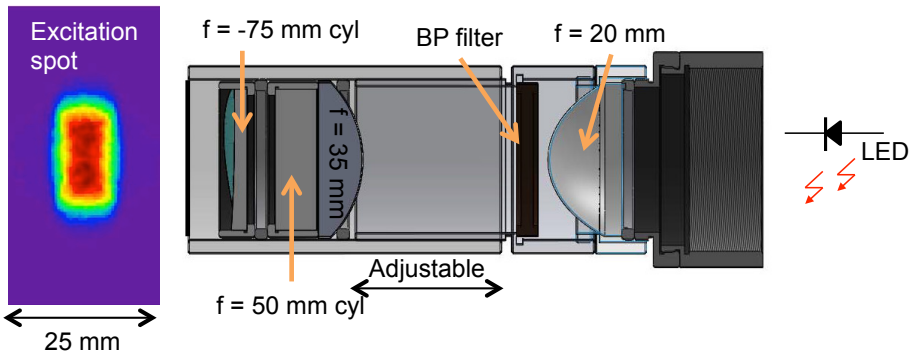

Figure 3.17: Excitation optics for Imaging System 2. In this image, light flows from right to left. The length of the excitation tube is adjustable. The axes of the cylindrical lenses are crossed to produce a rectangular excitation spot, left.

It was found that the low-frequency (~400 Hz) modulation of the microwaves directly caused the LED output to modulate, thus creating a huge feedthrough signal that overwhelmed the detection of the modulated NV fluorescence at the same frequency. Therefore, a resonant circuit was placed in series with the LED and the power supply to suppress low-frequency modulation of the LED light. The resonant circuit was formed with the parallel combination of two 10 µF film capacitors (for low equivalent series resistance or ESR) and a 10 mH inductor (Hammond 195J20). Additional suppression of LED modulation at the signal frequency was accomplished by placing an extra 120 µF of low ESR capacitance in parallel with the output of the power supply.

Fluorescence was collected on either side of the sample along the $\hat{y}$-axis, through the optics shown in Fig. 3.18a: first by collimation through a condenser lens (ThorLabs ACL2520-B), then long-pass filtering (Semrock BLP01-664R-25 664 nm EdgeBasic™ best-value long-pass edge filter), and finally focusing onto a photodiode via an identical condenser lens. The photodiode and preamplifier circuit are identical to the ones used in the first imaging system, as shown in Fig. 3.10. However, as shown in Fig. 3.18b, the photodiode is built into a shielded enclosure made out of copper pipe, with a copper mesh serving as an optically-transparent front window. Capacitive feedthroughs are used for the power connections to the

photodiode amplifier; however, they could not be used for the amplifier's output, as the capacitance was too high and they caused the amplifier to oscillate. A compromise was to solder a 330 pF capacitor as close as possible to the coaxial bulkhead connection at the back of the shielded enclosure. The capacitor blocked most of the microwaves from entering the shielded enclosure, without causing the circuit to oscillate.

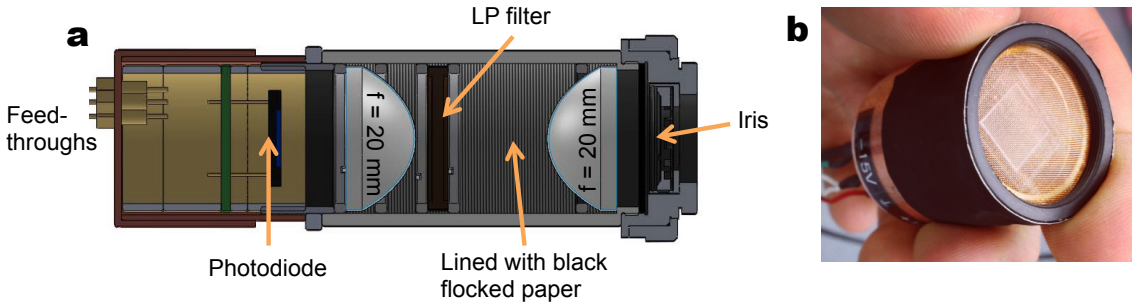

Figure 3.18: (a), Fluorescence collection optics for Imaging System 2. An iris controls the amount of and divergence half-angle of entering light. (b), The photodiode is built into a shielded enclosure, and a light-penetrable copper mesh (sealed to the enclosure on all sides with conductive copper tape) covers the front surface.

The outputs of the transimpedance amplifiers were separately amplified by low-noise voltage preamplifiers (Stanford Research Systems SR560) with the high-pass filter cutoff set at 100 Hz and the low-pass filter cutoff set at 1 KHz, and gain set to 10^3. The outputs of the SR560s were digitized at 125 KHz by a data acquisition (DAQ) card (National Instruments PCIe-6321). Microwaves were generated by an analog signal generator (Agilent E8257D) set to 2.872 GHz and -3 dBm output power (the reason for using 2.872 GHz, rather than 2.869 GHz, is explained in Fig. 4.7). After chopping with a PIN switch (Mini-Circuits ZASWA-2-50DR+) at 406 Hz (the resonance frequency of the LC tank circuit used to suppress excitation intensity fluctuations), the microwaves were amplified by a high power amplifier (Mini-Circuits ZHL-16W-43-S+) to provide ~8 W of microwave power that was directed toward the sample with a homemade helical antenna (6 turns, designed with center frequency at the operating frequency). A LabVIEW program synchronously detected the resulting changes in fluorescence. The program scanned the field-free line relative to the sample by varying the electromagnet current via an analog output board (National Instruments PCI-6722) connected to the magnet power supplies, and by varying the position of the translation stage. One problem with the current setup was the sample was supported at the end of a long cantilever to provide travel room for the translation stage. This turned out to amplify vibrations at the measurement frequency, which modulated the DC

background and appeared as a stochastic feed-through component (additive noise) on top of the signal.

The signal processing details within the LabVIEW program were similar to those used within the first imaging system. At each point in the image, signals from both photodetectors were recorded for a specified time τ_{meas} and then passed through a series of four elliptic 5^{th} order digital filters: a band-pass with a 310 Hz lower cutoff and 450 Hz upper cutoff to suppress signals far from the modulation frequency; a band-stop with a 55 Hz lower cutoff and 65 Hz upper cutoff and a band-stop with a 115 Hz lower cutoff and a 125 Hz upper cutoff to suppress 60 Hz/120 Hz line noise; and finally, a band-pass with a 382 Hz lower cutoff and 430 Hz upper cutoff to further suppress signals far from the modulation frequency. The signal was digitally mixed with cosine and sine waves oscillating at the microwave chopping frequency of 406 Hz to obtain the signal's in-phase and quadrature components, respectively. As before, six copies of the resultant signals were concatenated and then filtered by a 4^{th} order IIR Butterworth low-pass filter with a cutoff frequency of $1/(2\tau_{meas})$ Hz, pass-band ripple of 1 dB, and stop-band attenuation of 60 dB. The last $N = \tau_{meas} * 125$ KHz samples of the low-pass filter output were averaged, and the averages for the X and Y components were combined into a polar representation of the signal (i.e., R and θ), to obtain the image magnitude (and phase) recorded by each photodetector.

Chapter 4: Experiments and Results

In this chapter, we describe the proof-of-principle experiments of nanodiamond imaging, performed with the two different apparatuses.

Sample Preparation

NV-implanted (fluorescent) nanodiamonds (FNDs) were obtained from Prof. Huan-Cheng Chang of the Institute of Atomic and Molecular Sciences, Academia Sinica, Taipei, Taiwan. The details of FND production are explained elsewhere [17], [57]; briefly, synthetic type Ib diamond powder was irradiated with a 40 keV He^+ beam, annealed in vacuum at 800 °C, oxidized in air at 450 °C, and cleaned with a concentrated sulfuric acid/nitric acid treatment, yielding a final nanodiamond diameter of 100 nm and an NV concentration of ~6 ppm. FNDs were washed with distilled, de-ionized water and provided to us as a 1 mg ml^{-1} suspension in water.

A series of phantoms were created out of double-sticky tape covered with nanodiamonds. To make the nanodiamond phantoms, 2 x 2 mm squares of double-sticky tape were cut using a laser cutter. A 5 µl drop of the FND suspension was placed on each square of double-sticky tape and dried by placing it ~20 cm under a heat lamp. Two more additions of FND to each square of tape were made, to yield a 3.75 µg mm^{-2} areal density of FND on the tape. Each square was cut into 4 pieces of roughly 500 µm x 2 mm, and arranged into the various shapes shown in Fig. 4.1a: '+', 'C', 'A', and 'L'. The pieces of double-sticky tape were sealed between two pieces of Bio-Rad optical sealing tape. Pieces of chicken breast were prepared by freezing chicken breast (Trader Joe's Organic) and cutting into 10 mm x 10 mm x 20 mm ingots. An incision was made 5 mm back from the front of each piece and a phantom was inserted into the incision (see Fig. 4.1b).

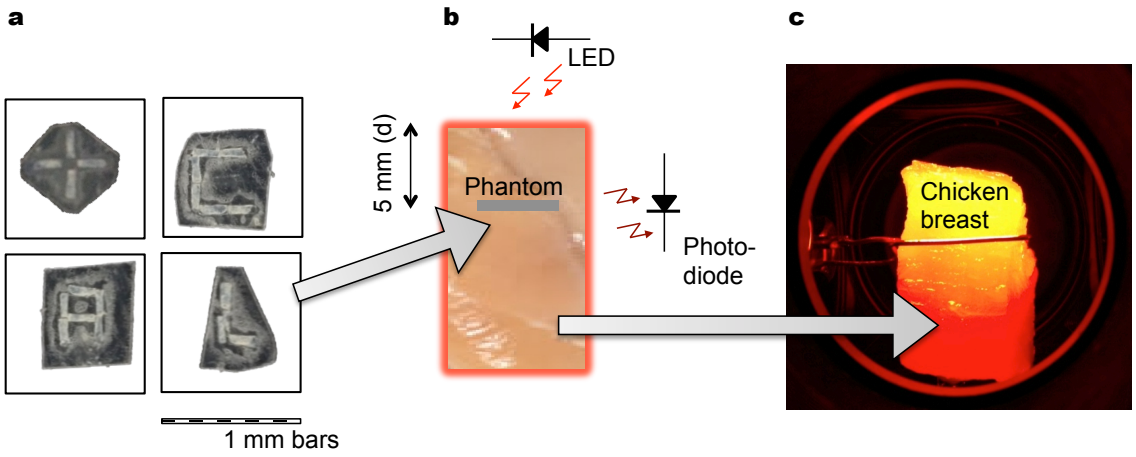

Figure 4.1: Phantoms in chicken breast. **a**, Nanodiamond phantoms made of double-sticky tape and nanodiamonds, shown at the same scale as the rest of the images. **b**, The grey stripe on the piece of chicken breast represents the edge of the phantom, which is placed inside the chicken breast, 5 mm back from the front surface, facing the LED. Fluorescence is collected off to the side. **c,** The actual piece of chicken breast illuminated by the LED.

Imaging

Many images of nanodiamond phantoms inside 1 cm x 1 cm x 2 cm pieces of chicken breast were taken to demonstrate the imaging technique using the first imaging system. For each phantom, image raw data were taken in a 40 x 40 grid over the 1 cm^2 field of view, with a 0.5 s measurement time at each pixel. Shown in Fig. 4.2 are the raw images and deconvolved images of the phantom outside of chicken breast obtained from the imaging system (a), raw and deconvolved images of the phantom under 5 mm of chicken (b; also the situation depicted in Fig. 4.1b), and for the 'L' phantom under 12 mm of chicken (c). Note no change in resolving power with depth, as expected. Also, once inside the chicken breast, a human observer can no longer see the phantoms, so there is some rotation of the phantom relative to the images of the phantoms outside of the chicken. The PSF in Fig. 4.2d is obtained from revolving the PSF in Fig. 4.4. In Fig. 4.2e, we show a line scan through the raw and deconvolved images of the "A" as indicated in Fig. 4.2a, and compare it to a line scan through a model of our phantom (representing a ground truth image) and through a simulated raw image of the phantom model.

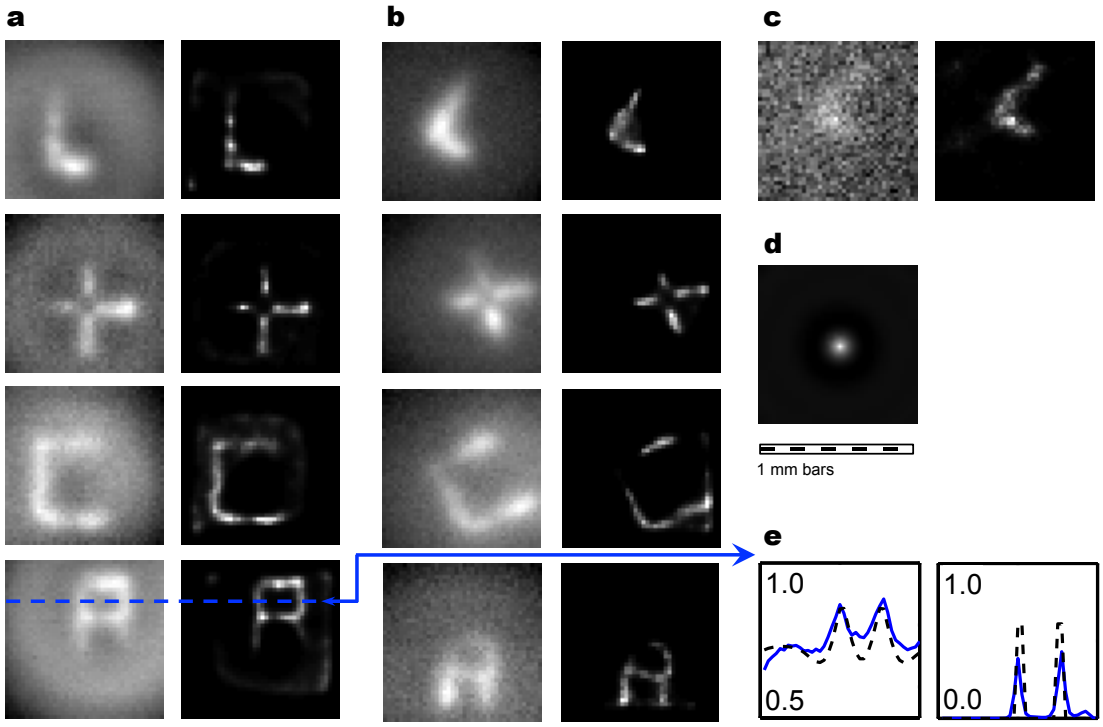

Figure 4.2: A summary of the data from the original nanodiamond imaging apparatus. **a**, The phantoms imaged outside of chicken breast, both before (left) and after (right) deconvolution by the point-spread function. **b**, Same as a but under 5 mm chicken breast. **c**, Image of the 'L' phantom under 12 mm chicken breast, before and after deconvolution. **d**, Point-spread function. All images are shown with a linear grayscale lookup table that spans the full range of the data in each image. **e,** Line scan through the raw image (left) and the deconvolved image (right) of the "A" phantom (solid blue lines); the dashed black line (left) represents the simulated raw image of the phantom, and it was generated by convolving a model of the phantom (dashed black line, right) with the PSF.

Obtaining the point-spread function experimentally

A linear, shift-invariant imaging system can be characterized in terms of a point-spread function. That is, by understanding the image produced by a "test point" of nanodiamonds, we have characterized the imaging system, as long as the image intensity is proportional to the amount of nanodiamonds in the test point, and that the shape of the test point's image does not vary with the test point's position. Although not precisely the case, we assume our imaging system can be represented by a shift-invariant point-spread function measured as described below.

To derive the point-spread function (PSF), a 2 mm x 2 mm piece of double-sticky tape was coated with a 3.75 μg mm^{-2} areal density of nanodiamonds. The piece was cut into four 500 μm wide x 2 mm long strips, and the strips were stacked

on top of one another, to yield a "test object" of 15 μg nanodiamond arranged in a roughly 0.5 mm x 0.5 mm x 2 mm volume. The test object was placed lengthwise into the end of a glass pipette, and introduced into the imaging system such that the long axis was parallel to the field-free line. An image (Fig. 4.3) was taken by scanning 100 x 100 pixels across the 1 cm^2 field of view, with $\tau_{meas} = 1$ s at each pixel, and the magnitude (a) and phase with respect to the microwave modulation (b) were recorded.

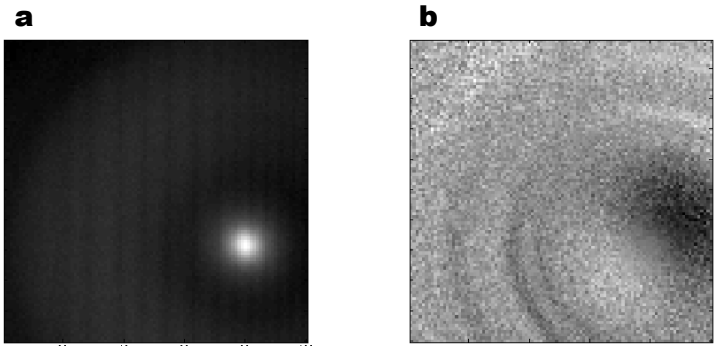

Figure 4.3: Data for determining the point-spread function of the first imaging system. **a,** Magnitude. **b,** Phase.

The microwave feed-through, as described in the next section (Processing of raw data), was subtracted from the image, and the resulting image was deconvolved with a 0.5 mm x 0.5 mm square (the on-axis profile of the test object) to obtain an estimate of the true PSF. The deconvolution was done in MATLAB, using 10 iterations of a Richardson-Lucy algorithm.

Next, the location of the peak value of the resulting data was found, and the data was mapped by bilinear interpolation onto a 2D polar coordinate grid with the origin at the location of the peak value, with grid spacing $\Delta r = 0.1$ mm and $\Delta\phi = 2\pi/300$ rad. For a given radial coordinate, the PSF was summed over the azimuthal coordinate to obtain the PSF as a function of the radial coordinate only (i.e., $\mathrm{PSF}(r) = \Sigma_{\phi_i}\mathrm{PSF}(r, \phi_i)$). Then, a 6th order polynomial, $\mathrm{PolyFit}(x)$, was fit to $\mathrm{PSF}(r)$. The final one-dimensional PSF, shown in Fig. 4.4, is $\mathrm{PolyFit}(|x|)$. To obtain a 2D PSF for deconvolution of the measured data, $\mathrm{PolyFit}(r)$ is sampled on a 40 x 40 grid (same as the measured data) with $r^2 = x^2 + y^2$, and $x_i, y_i \in \{-5.00, -4.75, \ldots, 4.75\}$, i.e., offset in the horizontal and vertical directions by half a pixel such that $r = 0$ at the center of one pixel, as shown in Fig. 4.2d.

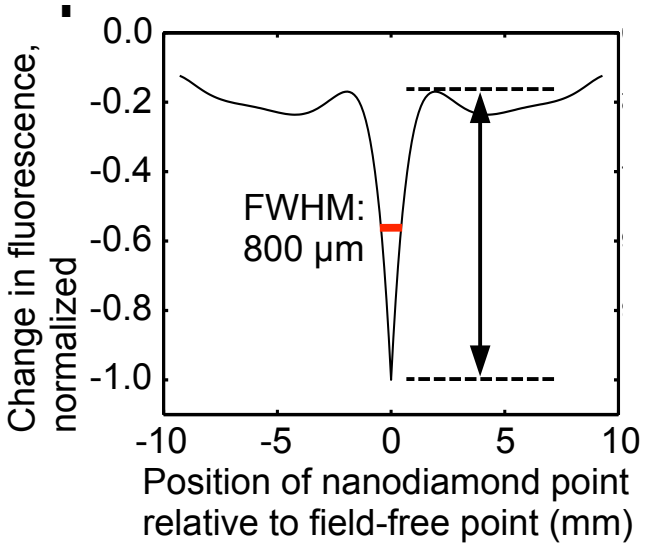

Figure 4.4: Imaging point-spread function. The height of the central peak, indicated by the two dashed lines with a FWHM of 800 μm, is 87% of the full height.

Processing of raw data

For the first experiment, there were two steps involved in going from the raw data to the deconvolved images, including removing a background component and performing the actual deconvolution. Chopping of the microwaves produced a background component in the signal most likely due to the rectification of the chopped microwaves by the photodiode. Since this "microwave feed-through" signal occurred at the same frequency as the signal of interest, it showed up in the raw data as an additive background with a particular magnitude and phase. The magnitude and phase of this background were determined by a measurement of the signal with the LED powered off.

Even though only the magnitude component of the signal was recorded when imaging the phantoms, a vector subtraction could still be performed to find the magnitude of the signal component that excluded the microwave feed-through. If x is the uncorrected image magnitude and b is the magnitude of the microwave feed-through, then the corrected image magnitude y is $y = \sqrt{|x^2 - b^2 \sin^2 \alpha|} - b \cos \alpha$, where α is the phase angle between the microwave feed-through and the hypothetical background-free signal (obtained by subtracting the microwave feed-through from a signal that included both magnitude and phase information). Note the absolute value around the radicand: in the absence of noise, the radicand would always be positive; however, for $x \approx b$, noise occasionally makes the radicand negative. Including the absolute value thus avoids unphysical complex image magnitudes, and does not appear to have an adverse effect on the images.

For each image except the 'L' under 12 mm chicken (Fig. 4.2c), the microwave feed-through was subtracted, and then the image was deconvolved by the PSF shown in Fig. 4.2d. A Richardson-Lucy (RL) algorithm was used to do the deconvolution, as part of DeconvolutionLab [58], an add-on for the ImageJ software package. The stopping point for this iterative algorithm was arbitrarily set to 10,000 iterations. As illustrated in Fig. 4.5, stopping too soon does not allow the algorithm to fully remove the blur from the PSF's wide tails (see Fig. 4.4), yet too many iterations produces a pixelated image due to the noise gain inherent in deconvolution.

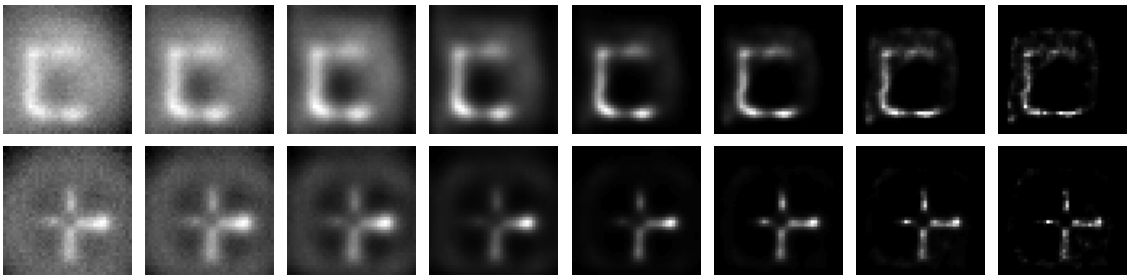

Figure 4.5: Richardson-Lucy deconvolution of images for 'C' and '+' phantoms as a function of the number of iterations.

For the 'L' under 12 mm chicken, no microwave feed-through subtraction was done, as doing so appeared to prevent convergence of the RL algorithm (this may have to do with the low SNR of that particular image). Also, only 1,000 iterations of the RL algorithm were used, so the image would not have too much noise amplification. The 12 mm deep image is included only to demonstrate that it is possible to image that deeply.

Richardson-Lucy will converge to the maximum-likelihood solution for an image corrupted by noise with a variance that follows the image intensity, as it normally does with the shot noise inherent in photon-based imaging. Our images are corrupted by noise that is identically distributed and independent between pixels: the variance of the shot noise of the recorded photons is the same in each pixel, as it depends on the unmodulated fluorescence background, which is constant during the imaging process. Although the RL algorithm can be modified to converge to the maximum-likelihood solution assuming noise with constant variance, the unmodified RL produced satisfactory results.

In addition, to simplify the estimation of the nanodiamond distribution from the recorded image, a shift-invariant PSF was assumed (i.e., it was assumed that the imaging process represented convolution with a PSF) rather than a more general space-varying model. Because convolution doesn't take into account position-

dependent sensitivity, the estimated nanodiamond concentration at a given point will be off by a factor that depends on the sensitivity at that point. Hypothetically, the sensitivity as a function of position can be recorded as calibration data, although in practice (i.e., imaging within an organism), this sensitivity function will differ with each imaging run as it will depend on the anatomy of the organism being imaged. With anatomical knowledge of the organism, perhaps obtained from a separate imaging modality (such as CT), it may be possible to estimate the varying sensitivity within the organism and compensate for it in an image reconstruction.

Measurement of sensitivity

To measure the sensitivity of the first system, a 2 mm x 100 μm piece of double-sticky tape, covered with 250 ng of nanodiamond, was prepared by cutting a ~100 μm sliver off of a 2 x 2 mm piece of double-sticky tape, prepared according to Sample Preparation, above (but using only a single 5 μl drop of nanodiamond solution). This piece of double-sticky tape was placed lengthwise into the end of a glass pipette, which was placed parallel to the field-free line. An image was recorded with the same parameters used to record the image of the PSF, and the microwave feed-through component was subtracted from the resultant image. To estimate the noise, the photodiode preamplifier's output was connected to a lock-in amplifier (Stanford Research Systems SR830) with a 100 ms time constant, selecting the "x-noise" measurement, with the LED on but microwaves off. The peak signal of the image was divided by the noise to get the SNR, which was 9.5 $Hz^{1/2}$. The sensitivity is thus (250 ng)/(9.5 $Hz^{1/2}$) = 26 ng $Hz^{-1/2}$ or 2.2 mM mm^3 $Hz^{-1/2}$, expressed in terms of the concentration of carbon atoms in a mm^3 voxel.

Images from Second Imaging System

Images were also obtained with the second imaging system, as shown in Fig. 4.6 (see the figure caption for the description of the images). The phantoms were constructed by arranging 2 x 2 mm squares of double-sticky tape, coated with 15 μg each of nanodiamond, into patterns as photographed in Fig. 4.6a and Fig. 4.6e. To facilitate arrangement of the squares, a 2 mm square grid was etched onto a piece of Bio-Rad optical sealing tape with a laser cutter; this piece of tape was used to support the double-sticky tape squares. The optical sealing tape was supported by an acrylic mount. The raw images are all recorded with 0.25 mm × 0.25 mm pixels, with 0.5 s of integration at each pixel, and with the microwave frequency set to 2.872 GHz (as opposed to 2.869 GHz, the NV zero-field resonance frequency—the reason for doing this is explained below, in Fig. 4.7). The deconvolved images are obtained from the raw images, using DeconvolutionLab in ImageJ, by applying 1000 iterations of the Tikhonov-Miller algorithm with regularization parameter 1E-4 and with a positivity constraint enforced on the solution.

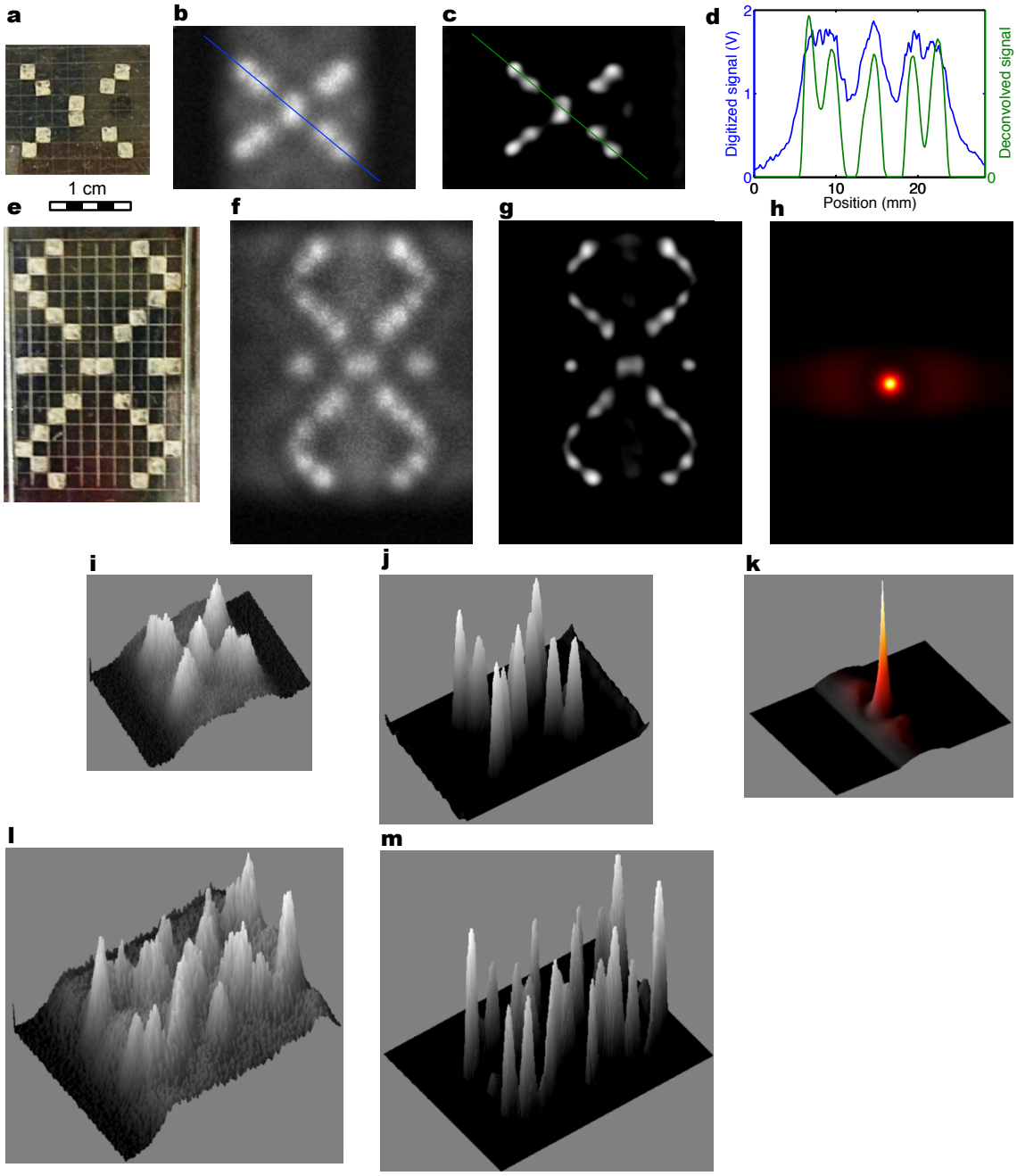

Figure 4.6: Image data from second imaging system. **a, b, i, c, j:** photo of phantom, raw image data, surface plot of data, deconvolved image, surface plot of deconvolved image for phantom in **a**. **e, f, l, g, m:** same, for phantom in **e**. **d,** line scans through images in **b** and **c**. **h, k:** Point-spread function and surface plot of PSF.

The point-spread function of the second imaging system, as shown in Fig. 4.6h and Fig. 4.6k, was obtained directly from ODMR data of the NV-

nanodiamonds. In order to do this, the permanent magnets were removed from the imaging system to separately measure the influence of magnetic field and position-dependent excitation intensity on the PSF. Two squares of nanodiamond-coated double-sticky tape were placed adjacent to each other to make a 4 mm x 2 mm test target. The 4 mm axis of the test target coincided with the major axis of the roughly elliptical LED excitation spot.

Two types of scans were performed to obtain the PSF. The first is illustrated in Fig. 4.7 and consisted of sweeping the magnetic field from -200 G to 200 G and observing the changes in fluorescence. This was done at two different microwave frequencies—2.869 GHz and 2.872 GHz—to show that it is actually advantageous to image with 2.872 GHz microwaves. At 2.872 GHz, the signal strength is 1.72x higher than at 2.869 GHz, yet the spatial resolution is almost the same (1.2 mm vs 1.0 mm FWHM, this time measuring the full height of the PSF rather than the height of the central peak as in Fig. 4.4). Most notably, at 2.872 GHz the PSF does not have the broad tails it has 2.869 GHz. Thus, imaging at 2.872 GHz better preserves the higher spatial frequencies of the nanodiamond concentration during the imaging process. To estimate the profile of the LED excitation spot and include it in the PSF, a second scan was performed by translating the test target across the minor axis of the excitation spot in Fig. 3.17.

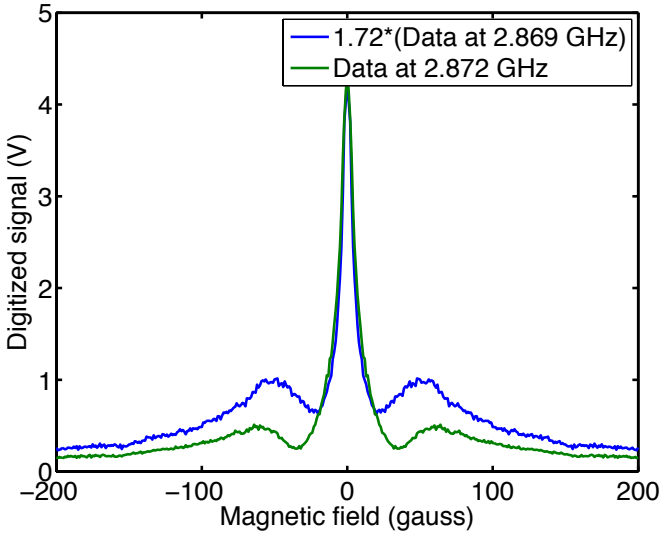

Figure 4.7: ODMR microwave frequency comparison using the second imaging system. Notice that the shape of the data is almost the same in each case, with the exception that the signal at 2.872 GHz is 1.72x the signal at 2.869 GHz, and the bulk of the signal energy is in the central peak at the higher frequency. (These plots have been symmetrized about 0 gauss).

To go from the recorded ODMR data to the PSF, the data from the first scan was used to obtain a plot for ODMR signal versus field magnitude B by averaging values at $\pm B$. A 9th order polynomial was fit to the resultant plot. We assumed that the magnetic field gradient G of the second imaging system was constant (due only to a quadrupole term), so the field magnitude a distance r away from the field-free line was given by $B = Gr$, and the polynomial could be evaluated as a function of r to calculate the dependence of the PSF on the spatially-varying magnetic field.

Next, a 6th-order polynomial was fit to the ODMR data as a function of position of the test target relative to the LED excitation spot. Because the test target had an extent of 2 mm in the scan direction, it was necessary to deconvolve the recorded data with a 2 mm wide "box" (Π-shaped) function to obtain a better estimate of the actual LED profile. This was done by modeling the imaging process as a convolution of the actual LED profile with the profile of the test target. The convolution was modeled as a matrix multiplication, $\boldsymbol{y} = \boldsymbol{A}\boldsymbol{x}$, where $\boldsymbol{y}$ is the result of convolving the actual LED profile $\boldsymbol{x}$ with the box function, and the rows of the matrix $\boldsymbol{A}$ represent shifted copies of the box function. The observed ODMR data $\boldsymbol{b}$ is a noise-corrupted version of $\boldsymbol{y}$, i.e. $\boldsymbol{b} = \boldsymbol{A}\boldsymbol{x} + \boldsymbol{n}$, where the noise vector $\boldsymbol{n}$ consists of independent identically-distributed Gaussian random variables. Finding the maximum likelihood estimate $\boldsymbol{x}^*$ of $\boldsymbol{x}$ is equivalent to solving a non-negative least squares problem, i.e.:

$$\boldsymbol{x}^* = \arg\min_{\hat{\boldsymbol{x}} > \boldsymbol{0}} \|(\boldsymbol{A} + \alpha \boldsymbol{I})\hat{\boldsymbol{x}} - \boldsymbol{b}\|_2 \,. \tag{4.1}$$

A small amount α of the identity matrix $\boldsymbol{I}$ was added to $\boldsymbol{A}$ as a regularization parameter, similar to (though not exactly the same as) Tikhonov-Miller regularization, which helps to bias the solution to the observed data and reduce noise amplification from the deconvolution. This problem was solved in MATLAB using the `lsqnonneg` function.

Finally, the contributions to the point-spread function from the spatially-varying magnetic field and the spatially-varying LED excitation profile were multiplied together and re-interpolated on a grid of the same size as the image to be deconvolved.

Chapter 5: Discussion

Chapter Summary

This chapter begins with a discussion of the resolution of the imaging technique that provides a simple analytical model explaining why the PSF scales as r^{-1} and why the imaging resolution is limited by strain within the nanodiamonds. A discussion of the sensitivity follows, with descriptions of many potential sensitivity improvements, including examples of modified "pulse sequences" that allow faster and/or higher SNR imaging than with the current technique. We discuss issues of light penetration into tissue as well as regulatory limits of human exposure to optical and microwave radiation. We then compare nanodiamond imaging to other techniques and show that it has the potential to combine the high sensitivity of molecular imaging with the high resolution of anatomical imaging. Finally, some discussion is presented regarding the deconvolution process.

Resolution

The resolution of a nanodiamond imaging system depends on the width of the PSF, which varies with the strength of the magnetic field gradient. With a 1 T m^{-1} gradient, the central peak of the PSF (indicated in Fig. 4.4) has a FWHM of roughly 800 μm. The amplitude of the PSF scales roughly as r^{-1}, where r is the distance from the field-free point to a test point of nanodiamonds, because the fraction of nanodiamonds still resonant with the microwaves also scales as this factor (gradient in Fig. 2.12b). Deviations from this scaling primarily come from strain in the nanodiamonds causing inhomogeneous broadening of the zero-field transition (reducing the maximum modulation of the fluorescence achievable with a single microwave frequency), the development of an anti-crossing between the $m_s = 1$ and $m_s = -1$ states with applied magnetic field (causing a pronounced first dip) and a lowering in energy of the $m_s = 0$ state at higher magnetic fields (blue-shifting the anti-crossing above the microwave frequency and increasing the proportion of NV transitions resonant with the microwaves).

To understand the rough $1/r$ scaling of the PSF it is helpful to consider how the optically-detected magnetic resonance (ODMR) lineshape of NVs in nanodiamond powder varies as a function of magnetic field. Note this is a simplification as compared to the full PSF calculation in Chapter 2: Theoretical Background. Let us consider a simplified version of the NV's spin Hamiltonian H, neglecting strain: $H = hDS_z^2$, where h is Planck's constant, D is the zero-field splitting (2.869 GHz) and $\boldsymbol{S} = (S_x, S_y, S_z)$ is the vector of Pauli spin matrices for $S = 1$. We can treat the interaction of the NV with the magnetic field as a perturbation H' to first order, where $H' = -g\mu_B \mathbf{B} \cdot \mathbf{S}$. Since the eigenstates of H are also eigenstates of S_z, only the z component of $\mathbf{B}$, $B_z = |\mathbf{B}| \cos\theta$ where θ is the angle between the NV spin axis and the magnetic field, contributes to first-order shifts in

the NV's energy levels. Thus, we have $E/h = 0$ for $m_s = 0$ and $E/h = D \mp \gamma|\mathbf{B}| \cos\theta$ for $m_s = \pm 1$ ($\gamma = g\mu_B/h$ is the gyromagnetic ratio).

The ODMR lineshape is comprised of an ensemble of NVs that are randomly oriented with respect to the magnetic field, therefore the lineshape should be indicative of spin transitions at frequencies ν within a range of $2\gamma|\mathbf{B}|$ centered at D. The probability density function (PDF) of θ for finding nanodiamonds at an angle $\theta \in [0, \pi]$ is $\sin\theta\,/2$, and using the probability change of variables formula, we see that the NV transitions should be uniformly distributed throughout their frequency range, i.e.:

$$\nu \sim 1/2\gamma|\mathbf{B}|, \nu \in [D - \gamma|\mathbf{B}|, D + \gamma|\mathbf{B}|] \qquad (5.1)$$

As the magnetic field increases, the frequency range increases linearly, but since the number of NVs is distributed across a larger frequency range, the amplitude of the ODMR lineshape decreases correspondingly. This is illustrated by experimental data in Fig. 5.1a, where we show ODMR data of NV-nanodiamonds from 2.819 GHz to 2.919 GHz and -40 gauss to 40 gauss. Note the width of the ODMR lineshape (i.e., a slice at a particular magnetic field) increases linearly with magnetic field, and the amplitude decreases correspondingly. There are a couple deviations from this model worth noting. First, the presence of a finite width at $|\mathbf{B}| = 0$ is due to strain in the nanodiamonds which splits the previously degenerate $m_s = \pm 1$ into two peaks. Also, this anti-crossing between the $m_s = \pm 1$ levels blue-shifts as the magnetic field is increased. (These data were taken with the first imaging system in the same way as the nanodiamond images were formed: by scanning the magnetic field, exciting optically, and looking at changes in fluorescence as microwaves were applied. The data in Fig. 5.1a are the same as the data in Fig. 2.16b.)

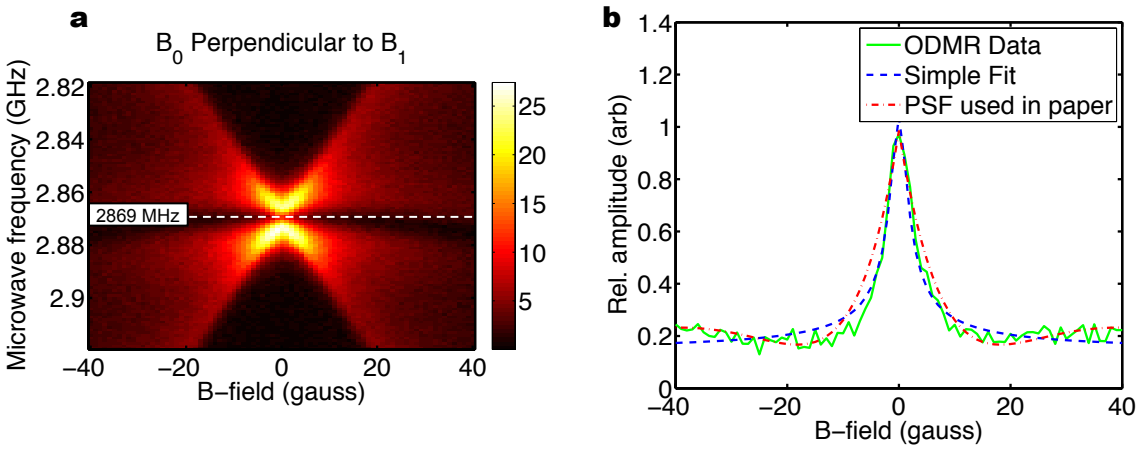

Figure 5.1: ODMR data and associated lineshape. **a**, ODMR data of NV-nanodiamond material. The scale is in terms of modulated photocurrent per quantity of nanodiamond, in pA μg^{-1}, as measured by the first imaging system (this plot is the same as in Fig. 2.16b). A slice through the data at 2.869 GHz is shown in **b** ("ODMR Data") and compared with the simplified fit to a hyperbolic model ("Simple Fit") as well as to the PSF used to deconvolve the images from the first imaging system ("PSF used in paper").

To understand how the imaging point-spread function relates to the measured ODMR data, assume we have a point of nanodiamonds located a distance r from a field-free line. We are in a quadrupolar magnetic field ($\mathbf{B} = Gy\hat{x} + Gx\hat{y}$) so $|\mathbf{B}| = Gr$ at the location of the nanodiamonds, where G is the magnetic gradient in T m^{-1}. Thus the width of the ODMR lineshape (as a function of microwave frequency), found by substituting the above expression for magnetic field magnitude into Eq. 5.1, is approximately $2\gamma Gr$. The PSF, given by the amplitude of the ODMR lineshape at its center frequency, is approximately $1/2\gamma Gr$, elucidating the $1/r$ dependence. However, due to strain, the width of the ODMR lineshape is non-zero at $|\boldsymbol{B}| = 0$ and remains roughly constant until the field magnitude is greater than the strain splitting (expressed in the same units). We can capture this behavior by fitting the width of the ODMR lineshape to a hyperbola, i.e.

$$\text{ODMR lineshape width} = ((2\gamma Gr)^2 + C_1^2)^{\frac{1}{2}}, \qquad (5.2)$$

where C_1 is a constant that represents the strain in the nanodiamonds. Therefore, (PSF amplitude) = 1/(ODMR lineshape width), or

$$\text{PSF amplitude} = \frac{1}{((2\gamma Gr)^2 + C_1^2)^{\frac{1}{2}}} + C_2. \qquad (5.3)$$

Here, C_2 is a constant added to the PSF model to produce a better fit to the actual

PSF, which has an approximately constant offset due to the blue-shifting of the $m_s = \pm 1$ anti-crossing with applied magnetic field.

Equation 5.3 thus represents a simplified mathematical model of the point-spread function. In Fig. 5.1b, we slice through the ODMR data of Fig. 5.1a at 2.869 GHz ("ODMR Data"). This is fitted by our simple hyperbolic model ("Simple Fit"), and also compared to the point-spread function used to deconvolve the images from the first imaging system ("PSF used in paper"). While "Simple Fit" fits the ODMR data well at lower fields, it does not capture how the PSF decreases as it cuts through the anti-crossing and then increases as it reaches the other side of the anti-crossing. "PSF used in paper" does capture this, but it is slightly wider than the ODMR data at low fields, perhaps because it was obtained experimentally from a sample with finite size.

It is also instructive to compare the PSF generated directly from the ODMR lineshape modeling in Chapter 2: Theoretical Background to the measured ODMR data, which we do in Fig. 5.2. Here, "Polynomial PSF fit" represents the PSF used to deconvolve the images from the first imaging system (same as "PSF used in paper" from Fig. 5.1b), "Calculated ODMR fit" is a slice through the ODMR lineshape calculated in Fig. 2.17b at 2.869 GHz, and "Measured ODMR" is the same as "ODMR Data" from Fig. 5.1b. Note that although the blue-shifting of the anti-crossing is captured in the model as shown in Fig. 2.17b, the model does not seem to capture the "dip" in the PSF that this blue-shifting causes. (We have assumed a 1 T m^{-1} gradient to convert magnetic field strength to position.)

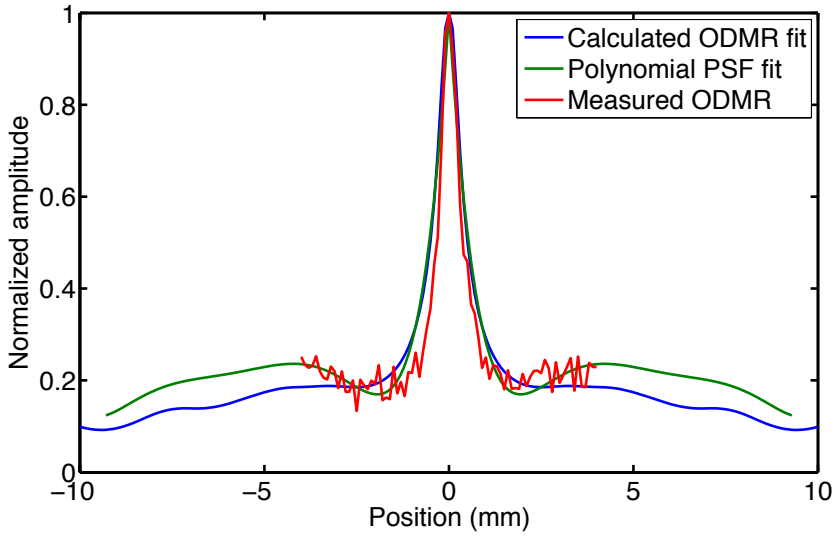

Figure 5.2: Comparison of calculated and measured ODMR (at 2.869 GHz) to PSF used to deconvolve images from first imaging system.

The primary limit to the spatial resolution within a given magnetic field gradient is strain in the nanodiamonds, as captured by the constant C_1 in Eq. 5.3. Note that if this imaging technique were based on sensing a single NV spin transition, strain would only shift the transition away from 2.869 GHz. Because a nanodiamond imaging system senses an ensemble of NV spins with varying strains, the strain causes inhomogeneous broadening of the ensemble of spin transitions. As usual for spin-resonance-based imaging, the resolution scales as $\Delta x \approx \Gamma/\gamma G$; here, Γ is the inhomogeneously-broadened linewidth of the NV transition at zero magnetic field, γ is the gyromagnetic ratio, and G is the magnetic field gradient. If there were no strain, the resolution would be limited by the natural linewidth of the NV spin transition. Of course, increasing the field gradient would increase the resolving power, but we are limited to a field gradient that can be practically applied to non-invasive imaging of a macroscopic living organism.

The random orientation of the nanodiamonds does not degrade the spatial resolution—as stated previously in Chapter 3: Imaging Method and Apparatus, the reason we image with a field-free point is because it has no intrinsic orientation; therefore, the orientation of the nanodiamonds at the field-free point (or line) does not matter. While, in theory, spin-echo-based techniques would eliminate inhomogeneous broadening from strain and other sources, we are limited for the time being to incoherent measurement schemes. This is because we are performing organism-scale imaging with potential clinical application so we are limited in the amount of microwave power we can use.

Sensitivity

The sensitivity of the first imaging system was carefully measured by introducing a known quantity of nanodiamond into the imaging system and scaling the quantity to a signal-to-noise ratio (SNR) of unity. The sensitivity to detect the presence of nanodiamonds at the surface of a tissue sample was measured as 2.2 mM mm^3 Hz$^{-1/2}$, as described in Chapter 4: Experiments and Results under "Measurement of sensitivity". That is, a 2.2 millimolar concentration of carbon atoms in a 1 mm^3 voxel can be detected with an SNR of unity in 1 Hz of measurement bandwidth. This corresponds to a sensitivity of 24 pM mm^3 Hz$^{-1/2}$ in terms of the 100 nm nanodiamonds used in the experiments, or a mass sensitivity of 740 pg of nanodiamonds in 100 s of measurement time. Ideally, the primary noise source of a nanodiamond imaging system is shot noise from the unmodulated background fluorescence; however, significant amounts of noise can be generated by sample vibrations that modulate the background fluorescence at the measurement frequency. While the first imaging system was shot-noise-limited, the second one suffered from vibration-induced noise at a level of approximately 5x the shot-noise limit.

There are many performance enhancements we can expect which would drive sensitivity much higher, more than 7 orders of magnitude in combination. These are summarized in Table 5.1. Most notably, different NV-nanodiamond

synthesis techniques may increase the ratio of NVs to carbon atoms. The nanodiamonds used in the current experiments contain 6 ppm NV, introduced by ion implantation and annealing. It has been shown that sintering detonation nanodiamond may produce up to a 1% (10,000 ppm) concentration of NVs in the nanodiamonds [20]. Also, a bottom-up synthesis of NV-nanodiamond clusters, for example starting with nitrogen-functionalized diamondoids [59], may offer the potential to engineer out the strain in the nanodiamonds which causes inhomogeneous broadening. Doing so would create a sharper PSF by increasing the signal at the center of the PSF and decreasing the width of the PSF. It could also yield a high NV concentration. Further sensitivity enhancements, discussed in detail in the following paragraphs, are expected from pulsing the optical and/or microwave excitation, enhancing the amount of fluorescence collected, time-gating the fluorescence collection, water-cooling the organism to allow a higher optical excitation intensity, and reducing nanodiamond strain (which would also produce higher resolution).

Table 5.1: Factors expected to contribute to the increases in sensitivity of nanodiamond imaging. For each parameter to improve (in italics), two numbers are given in the second column: one indicating a relative or absolute value of the parameter in the experiments with the first imaging system, as well as a reasonable estimate of how much that parameter could be enhanced. Listed in the last column are the projected sensitivity increases due to each expected parameter improvement.

Parameter to improve	Expected improvement	Sensitivity increase
Materials enhancements		
Concentration of NVs in nanodiamond	6 ppm → 10,000 ppm	1,666x
Strain of nanodiamonds	5 MHz → 1 MHz	5x
Taking advantage of dynamics		
Duty factor of light pulsing	100 % → 10 %	10x
Fluorescence modulation depth increase by full spin inversion	50 % → 100 %	2x
Unmodulated background decrease by time-gating fluorescence collection	100 % → 10 %	3.2x
General system optimization		
Improved *light collection efficiency*	100 % → 300 %	1.7x
Increased *optical excitation intensity* (by water-cooling the organism)	100 % → 1,000 %	32x
	Product of possible sensitivity increases ≈	**29,000,000x**

Increases in sensitivity could be generated by modifying the imaging approach from a continuous wave (CW), quasi-static measurement scheme to one that is more dynamic. The CW scheme is the simplest measurement scheme; it is depicted in the timing diagram in Fig. 5.3. Here, the excitation light is left on continuously, while the microwaves are modulated with a 50% duty factor (or amplitude modulated with a sine wave). Since this is a synchronous measurement, the measurement phase is shown to alternate synchronously with the chopping of the microwaves.

The equilibrium spin polarization is the steady-state between the polarization of the spins caused by optical pumping and the natural spin relaxation; therefore, the amount of spin polarization that occurs is a function of the excitation light intensity, as shown in Fig. 2.10. At lower optical excitation intensities—such as those that might be used in practice—where the spin polarization is linear in the excitation intensity, a two-fold increase in optical intensity results in a *four*-fold

increase in signal, and only a $\sqrt{2}$-fold increase in noise. Thus, sensitivity scales as the 3/2 power of excitation intensity: a factor of 1 because of the increased fluorescence modulation caused by the increased spin polarization, and a factor of 1/2 because of the increase in unmodulated background fluorescence.

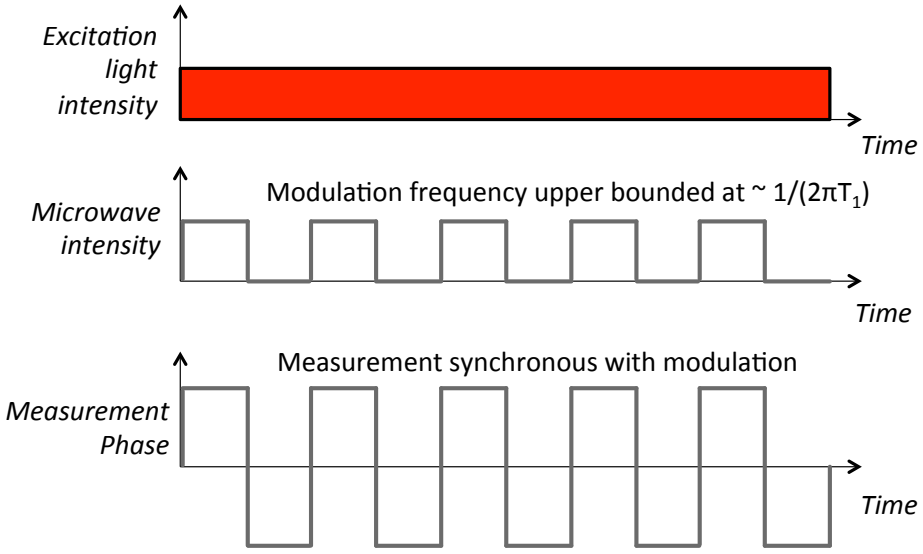

Figure 5.3: Pulsing scheme 1 (CW): The easiest measurement scheme to implement is not technically a pulsed scheme. Rather, it is a continuous (CW) measurement scheme where the excitation is on continuously, and the microwaves are chopped at 50% duty cycle (or amplitude modulated with a sine wave), thereby creating periodic dips in the fluorescence from the NVs present at the field-free point/line. The reversal in measurement phase that is synchronous with the microwave chopping is meant to indicate synchronous detection.

Switching to pulsed optical excitation is one way to increase the sensitivity. For the same optical energy in a measurement cycle, concentrating it in a duty factor $D < 1$ yields an SNR improvement of $1/D$: the higher optical intensity generates a higher spin polarization, enabling a greater modulation depth in the NV fluorescence. That is, we can take advantage of the increase in signal at higher optical excitation intensities without excessive or dangerous heating of the subject by lowering the duty factor. This pulsing scheme is illustrated in Fig. 5.4, whereby a two-fold increase in optical excitation intensity at a 50% duty cycle increases the signal modulation by a factor of 2 yet leaves the total integrated signal constant. Overall, the SNR would increase by a factor of 2.

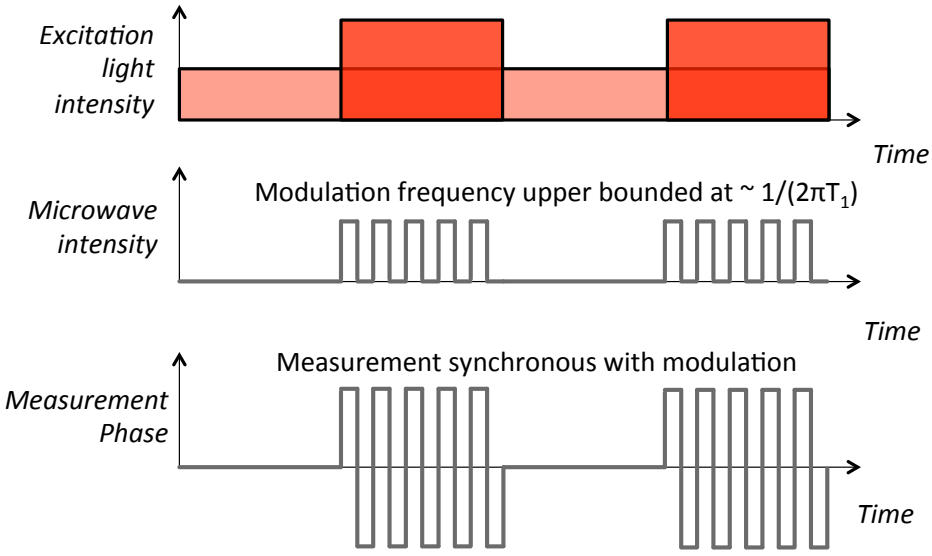

Figure 5.4: Pulsing scheme 2 (CW with reduced duty factor): This pulsing scheme is similar to the CW pulsing scheme except it is run at a duty factor less than 100%, allowing for higher optical intensities. For example, reducing the duty cycle to 50% allows the same amount of light to be collected at twice the excitation intensity. Thus the noise for a given measurement is the same, but the signal can be up to twice as great because of the enhanced spin polarization that results from doubling the excitation intensity.

By appropriately pulsing the microwaves, we can double the fluorescence modulation depth by fully inverting the spin population, as in Fig. 5.5 (for example by adiabatic fast passage [60]). This is in contrast to the CW scheme, where the spin population is merely equalized between brighter and darker states. Here, a strong optical pulse polarizes the NV spins, followed by a longer, weaker pulse that probes the NV spins without inducing significant spin polarization. During the probe pulse, the NV spins within the field-free region are periodically inverted by a series of "π" (inversion) pulses, and changes in fluorescence are measured synchronously with the spin inversions. Using pulsed microwaves allows much faster scanning of the field-free point/line than the previous measurement techniques allowed. This is because we need multiple fluorescence modulations at each location of the field-free point/line, and with a CW technique each period of the modulation cannot be much faster than T_1, the spin relaxation/repumping time from Eq. 2.20. With pulsed microwaves, the fluorescence modulation can be made arbitrarily fast.

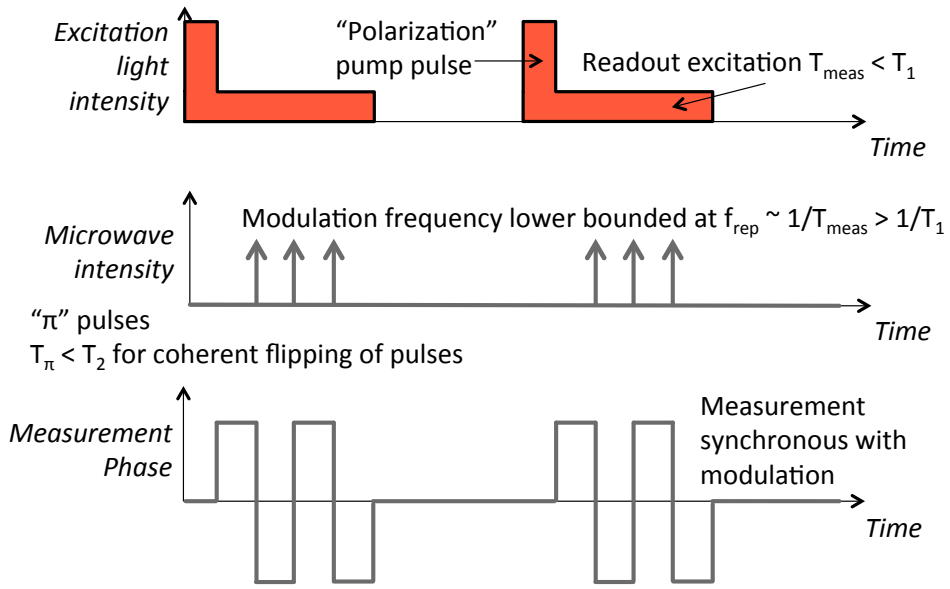

Figure 5.5: Pulsing scheme 3: pulsed spin polarization followed by pulsed microwave inversions. This scheme can potentially image much faster than the previous two pulsing schemes in which the NV spins must be repolarized with each modulation of the microwaves, thereby limiting dwell time at each pixel/voxel to T_1 (Eq. 2.20). Here, a dynamic measurement is performed that first polarizes the NV spins with a brief intense pulse of light, and then monitors the NV spin polarization with a lower optical excitation intensity while the spins are periodically inverted. Due to the low duty factor of the microwaves, a high instantaneous microwave intensity can be used to perform coherent "π" pulses for spin inversion while still maintaining low average microwave power. Signal strength can be up to double that of the previous two techniques because the microwaves invert the spin population from the brighter state to the darker states, rather than just equalizing the spin populations between those states.

Note that any combination of pulsed/CW excitation light as well as coherent and incoherent microwave excitation may be combined into a pulse sequence. However, coherent microwave pulses require the ability to generate high instantaneous microwave powers, such that the microwave Rabi frequency is greater than the decoherence rate; this necessitates the use of costly microwave amplifiers.

Finally, applying time-gated fluorescence collection in combination with pulsed optical excitation would enhance sensitivity because tissue autofluorescence occurs on a shorter timescale than fluorescence of NVs [16], and time-gating the detectors could also prevent excitation light that scattered through the optical interference filters from being measured. Decreasing these unmodulated

background components by a factor α would result in a sensitivity increase of $\alpha^{1/2}$, as the shot noise only decreases with the square root of the background intensity.

Penetration depth into tissue

The main drawback of nanodiamond imaging is the limited depth penetration due to the attenuation of light within tissue. Light penetrates through tissue in the diffusive limit, where the mean scattering rate per cm, μ_s, is much higher than the mean absorption rate per cm, μ_a. The effective attenuation per cm, μ_{eff}, of light into tissue is given by the following equation [15]:

$$\mu_{eff} = \sqrt{3\mu_a\left(\mu_a + \mu_s(1-g)\right)}, \qquad (5.4)$$

where g is an anisotropy parameter that measures how anisotropic the scattering is ($\mu_s(1-g)$ is the reduced scattering coefficient and is a measure of the rate at which a photon propagating through tissue loses all information about its starting direction). Note that although the optical intensity diminishes quickly inside the tissue, light trapping within tissue can theoretically enhance the optical intensity relative to outside the tissue by a factor of up to $2n^2$ [61]. This intensity increase is due to the higher index of refraction $n \approx 1.4$ of tissue relative to air [62] as well as the highly scattering tissue acting as a good reflector of light, analogous to a sheet of white paper. An idealized profile for the optical intensity as a function of tissue depth in a semi-infinite medium is shown in Fig. 5.6:

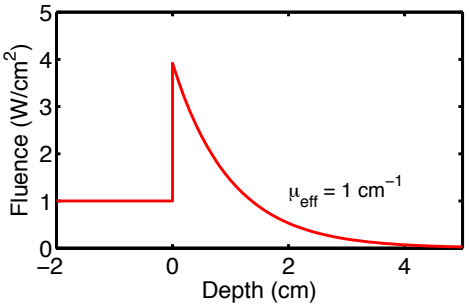

Figure 5.6: Profile of optical penetration into a semi-infinite 1D tissue sample (air/tissue interface is at 0 cm). Note the sharp increase in optical intensity at the air/tissue interface due to light trapping. An effective optical attenuation of 1 cm^{-1} is used, approximately what is calculated for human breast tissue at near-infrared wavelengths [63].

For a uniformly illuminated semi-infinite slab of tissue, the imaging signal attenuates with depth at a rate three times faster than the effective optical attenuation. First, the optical excitation must pass through tissue to excite the NVs and generate fluorescence; furthermore, the NV spin polarization, and hence the

modulation of the fluorescence achievable with the microwaves, is proportional to the optical excitation; finally, the fluorescence also has to escape from the tissue. Despite this rapid attenuation of signal, the range of depth penetration of nanodiamond imaging may make it perfectly suitable to preclinical (small-animal) imaging, which is often done with nude albino mice. Also, nanodiamond imaging may be useful for certain kinds of depth-limited clinical imaging. Chicken breast may be a good surrogate for human breast tissue due to its similar optical properties [64], and since we have already demonstrated imaging at a depth of over 1 cm in chicken breast, with improvements it may be possible to image at depths of 2-3 cm or more.

For clinical applications, we must be cognizant of the legal and safe limits of exposure to high-intensity optical and microwave radiation. We currently use incoherent optical excitation, for which there is no predefined legal limit. A practical exposure limit to incoherent optical excitation would prevent undue heat stress on a subject, and it could potentially rely on a subject's natural avoidance mechanism of thermal stresses [65]. For coherent light at the wavelengths of interest, the FDA sets a strict CW limit at 200 mW cm^{-2} [66]. The pulsed power limits are 1.1 W cm^{-2} $(T_{on}\ \mathrm{s}^{-1})^{-0.75}$ for coherent [66] or 2 W cm^{-2} $(T_{on}\ \mathrm{s}^{-1})^{-0.75}$ for incoherent light [65], for pulses less than 10 s, and with average power not to exceed CW power.

The penetration of microwaves into tissue is also depth-limited, but the optical penetration depth is typically the limiting factor in nanodiamond imaging. Microwaves at 3 GHz will penetrate from 2 to 10 cm into tissue, penetrating furthest into the fattiest tissues [67]. The FCC limit to microwave exposure at 3 GHz is 5 mW cm^{-2}, with an averaging time of 5 minutes [68].

Comparing to existing techniques

For a reference point, it is helpful to make a comparison of nanodiamond imaging to existing imaging techniques. In Fig. 5.7, we attempt to compare nanodiamond imaging (NDI) to several popular imaging techniques on the basis of sensitivity (in terms of minimum detectable mass of imaging agent), resolution, and cost. For existing techniques, there is a clear breakdown into two groups: those with higher resolution but lower sensitivity (labeled "Anatomical"), and those with higher sensitivity but lower resolution (labeled "Molecular"). The current implementation of NDI (a) has higher mass sensitivity than existing anatomical techniques and higher resolution than the molecular techniques. With four orders of magnitude sensitivity improvement (around 0.03% of the identified avenues for improvement), and less than one order of magnitude improvement in resolution—possible by increasing the magnetic field gradient or reducing nanodiamond strain—nanodiamond imaging would rival both molecular imaging in terms of sensitivity and anatomical imaging in terms of resolution. There are also no obvious barriers to low cost; the system is not significantly more complex than an optical imaging system.

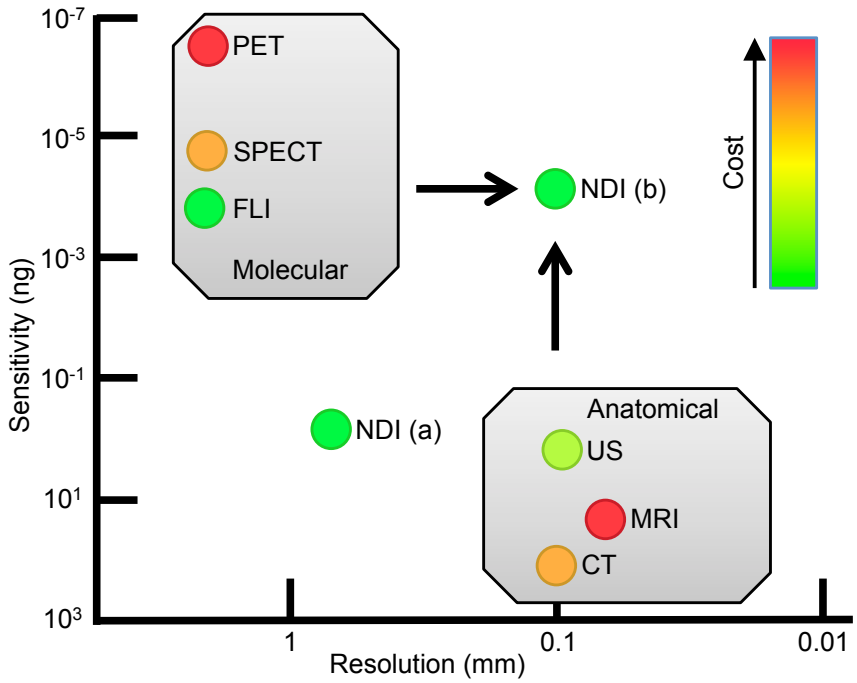

Figure 5.7: Comparison of nanodiamond imaging to existing techniques. Both the current implementation of nanodiamond imaging (NDI (a)) and future implementation (NDI (b), with 0.03 % of potential sensitivity improvements, and reasonable increase in resolution) are compared to popular existing molecular and anatomical imaging techniques, in terms of mass sensitivity, resolution, and cost. FLI: fluorescence imaging; US: ultrasound.

Four references were used in the compilation of Fig. 5.7: Table 1 of Ref. [3], Table 2 of Ref. [69], Table 1 of Ref. [70] and Table 1 of Ref. [71]. For a given imaging modality, the sensitivity was calculated by taking the lowest and highest sensitivities quoted in all four references, and finding the geometric mean. Note that the sensitivities in Ref. [71] are described in terms of quantity (in moles), rather than concentration (in molarity), of contrast agent. Using a reference volume of 1 cm^3 appeared to produce sensitivities consistent with the other references. Only Refs. [70] and [71] were used for CT, and only Ref. [71] was used for US. Although other data were available for US in the other references, they referred specifically to microbubble contrast agents, which can be sensitively detected with US (10^{-12} M) but cannot escape the vasculature. Although we had no data to compare the sensitivity of US in Ref. [71] to, we assumed the 1 cm^3 reference volume still held. Note we discuss some specific similarities and differences to MRI in Chapter 2: Theoretical Background.

To compute the noise bandwidth for direct comparison of the sensitivity of nanodiamond imaging to the sensitivities listed in the references where no noise

bandwidth was given, a measurement time of 100 s was assumed. This gave an equivalent noise bandwidth of 780 μHz for a 24 dB oct^{-1} filter such as in the SR830 lock-in amplifier. To go from concentration of imaging agent to absolute quantity of imaging agent in moles, a voxel volume of 1 mm^3 was assumed. Finally, to go from molar sensitivity to mass sensitivity, a representative molecular weight was chosen for each modality according to Table 5.2, below. Although up to a 29,000,000x sensitivity improvement has been identified for nanodiamond imaging, we only included a 10,000x improvement between NDI (a) and NDI (b) in Fig. 5.7.

Table 5.2: Molecular weights of prototypical contrast agents used to determine the mass sensitivity of each imaging modality (DOTA is a chelator). *For US, the geometric mean of the other molecular weights was used.

Modality	Imaging agent	Molecular weight (g/mol)
CT	iodine	127
MRI	magnevist	938
PET	18-FDG	181
SPECT	DOTA-tris(tBu)ester	573
FLI	IRDye 800CW	1165
US	*	154
NDI	Nanodiamond	12

To find the resolution, for each modality, the geometric mean was taken across the lowest and highest values quoted in each reference (the quoted ranges appeared to include both mouse-scale and human-scale numbers). The color of each data point is a measure of the relative cost, as extrapolated from the information provided in the four references.

Image processing and deconvolution

An advantage of our imaging technique is its transparency: the raw image data reveals the basic structure of the nanodiamond distribution, and tomography or inversion of an imaging system model (in this case, represented by deconvolution) is not required to present the data in a visually useful form. However, deconvolution by the PSF produces an image that is essentially a maximum likelihood estimate of the nanodiamond distribution within the sample. The deconvolution we apply is not to sharpen the image, but mostly just to remove the DC background caused by the "long tails" of the PSF.

Deconvolution is equivalent to solving the inverse problem of calculating the nanodiamond distribution that produced the resulting image. For example, assume that $\boldsymbol{Ax} + \boldsymbol{n} = \boldsymbol{b}$ is an equation that models the imaging system, where $\boldsymbol{x}$ is a vector

representing the nanodiamond distribution over the image field of view, $\boldsymbol{A}$ is the system matrix that represents the transformation of the nanodiamond distribution into a noise-free image, $\boldsymbol{n}$ is added noise, and $\boldsymbol{b}$ is the measured data. The noise vector $\boldsymbol{n}$ is a Gaussian random vector with independent elements, and its variance a function of the unmodulated signal background. The maximum likelihood estimate of $\boldsymbol{x}$—call it $\boldsymbol{x}^*$—is given by the solution to the equation: $\boldsymbol{x}^* = \text{argmin}_{\hat{\boldsymbol{x}}} |\boldsymbol{A}\hat{\boldsymbol{x}} - \boldsymbol{b}|_2$, where $|\cdot|_2$ represents the standard Euclidean (ℓ_2) norm. However, we must enforce the element-wise constraint $\hat{\boldsymbol{x}} \geq \boldsymbol{0}$ to ensure the solution does not include unphysical negative estimates of nanodiamond concentration.

When constructing the system matrix $\boldsymbol{A}$, may factors can be taken into account. A simple system matrix would assume that the system was shift invariant, essentially modeling a convolution. Underlying this assumption are the further assumptions that the excitation intensity, both optical and microwave, and the detection sensitivity, are shift invariant. In addition, for strict shift invariance the microwave field needs to have the same orientation relative to the static magnetic field at all points across the field of view. Otherwise, the point-spread function will vary slightly with the direction of the microwave field relative to the direction of the magnetic field at any given voxel (compare Figs. 2.16a and b). A more complete system matrix would take into account the spatial variations in excitation intensity and detection sensitivity. It is possible to obtain a first-principles derivation of the system matrix by finding the expected ODMR lineshape at each pixel or voxel as in Chapter 2: Theoretical Background.

High-frequency noise-gain is inherent in any deconvolution or system inversion when the forward imaging process attenuates high spatial frequencies, because the inverse process must amplify the attenuated image frequencies. Since the amplitude of the noise that is added by the forward imaging process is roughly independent of spatial frequency, the highest frequency noise is amplified the most. Regularization techniques are used to limit this high-frequency noise-gain. Typically, regularization is added by modifying the argument of the objective function to be minimized, $|\boldsymbol{A}\hat{\boldsymbol{x}} - \boldsymbol{b}|_2$, during a least-squares fit. One type of regularization, known as Tikhonov regularization, constrains the norm of the solution vector by modifying the least-squares problem to $\boldsymbol{x}^* = \text{argmin}_{\hat{\boldsymbol{x}}}(|\boldsymbol{A}\hat{\boldsymbol{x}} - \boldsymbol{b}|_2 + \beta|\hat{\boldsymbol{x}}|_2)$, where β is a positive real number. The extra term $\beta|\hat{\boldsymbol{x}}|_2$ can be interpreted as incorporating prior knowledge of the higher probability of minimum norm solutions. More generally, we can include a term $|\boldsymbol{B}\hat{\boldsymbol{x}}|_2$ where $\boldsymbol{B}$ is a matrix that can be used to weight probabilities of different potential solutions according to the singular vectors and singular values of $\boldsymbol{B}$. For example, $\boldsymbol{B}$ can be used to minimize the presence of sharp "edges" in $\hat{\boldsymbol{x}}$ by structuring it as a difference operator between nearest-neighbor pixels.

To get an idea of the signal-to-noise ratio at different spatial frequencies (independent of deconvolution), we look at the modulation transfer function, or MTF [72]. The MTF can be used to relate the *detection* sensitivity of nanodiamonds,

proportional to the DC signal strength $\hat{m}(0)$, to the *imaging* sensitivity at a particular spatial frequency, proportional to $\hat{m}(f)$. We can define it as follows:

$$\mathrm{MTF}(f) = \left|\frac{\hat{m}(f)}{\hat{m}(0)}\right|, \tag{5.5}$$

where $\hat{m}(f)$ is the Fourier transform of the PSF at the spatial frequency *f*. Thus, the MTF is the magnitude of the Fourier transform of the PSF normalized to its DC magnitude.

The relationship between resolution Δx and spatial frequency is $\Delta x = 1/2f$. As a rule of thumb, deconvolution recovers object features with a resolution no smaller than that corresponding to the highest spatial frequency imaged with an SNR > 1. Below in Fig. 5.8, we plot the MTF for the second imaging system using the PSFs from Fig. 4.7 (assuming a 1 T m^{-1} gradient). From this plot one can see that at 2.872 GHz, there is more energy at higher spatial frequencies relative to DC than there is at 2.869 GHz. We see that at a spatial frequency of 0.5 line pairs per mm, corresponding to a resolution of 1 mm, the MTF is approximately 0.1. That means we need an SNR 10x greater (or more, for higher image quality) to image with a resolution of 1 mm than we do to simply detect the presence of nanodiamonds in a sample. This difference between imaging sensitivity and detection sensitivity is not unique to nanodiamond imaging. Imaging sensitivity is a function of spatial frequency and is related to the imaging system's MTF; all imaging systems act like low-pass filters to some extent. Sensitivity at high spatial frequencies cannot be increased by deconvolution, which amplifies both signal and noise.

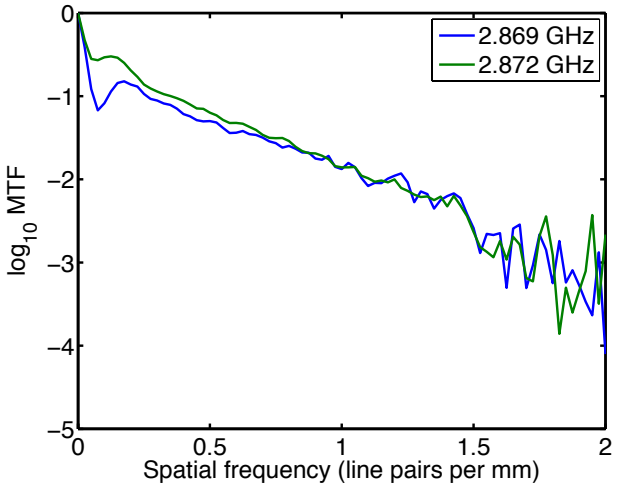

Figure 5.8: Modulation transfer function of PSFs from Fig. 4.7 (assuming a 1 T m^{-1} gradient).

Chapter 6: Conclusion

By combining optical detection with magnetic resonance, nanodiamond imaging achieves high sensitivity and high spatial resolution. It is absent of the complications of ionizing radiation, and the cost should be similar to all-optical imaging. Because of the limit set by optical penetration into tissue, nanodiamond imaging cannot image beyond depths of a few cm. However, it may open up new avenues of investigation for applications where high depth penetration is not required, such as in small-animal imaging [73], [74], tumor margin imaging [75], sentinel lymph node mapping [13], [76], and perhaps mammography.

Another, potentially better, material system might be identified that could be used as an imaging agent in a technique analogous to nanodiamond imaging; there is no reason to restrict this technique to using NV-containing nanodiamonds. An ideal nanoparticle imaging agent would be non-toxic, easy to produce, and easy to biologically functionalize. It must exhibit some form of optically-detected magnetic resonance, such as the optically induced spin polarization and fluorescence-based spin detection of NVs. Long spin relaxation T_1 and spin coherence T_2 times are desired for high levels of spin polarization and narrow spin transition linewidths; the inhomogeneously-broadened linewidth, given by $1/T_2^*$, must similarly be narrow. Ideally, optical excitation and fluorescence would both occur in the near-infrared for greatest tissue penetration. Also, a zero-field splitting significantly smaller than 2.869 GHz would be desired, as this would simplify all aspects of the RF subsystem, from generation and amplification of RF energy to delivering the energy to the subject. Lower frequency RF would also penetrate further into the subject. A breakthrough advance in this technique would be the ability to multiplex, i.e., simultaneously image different imaging agents that are functionalized for different targets. Multiplexing might be accomplished by somehow tuning the zero-field splitting of the spin transitions such that each target is imaged with a separate RF or microwave frequency. Finally, the characteristics of the particles themselves must be reasonably stable.

A potential simplification of nanodiamond imaging would be to do away with microwaves and perform all-optical imaging, still using a field-free point (or line). By relying on the spin-mixing between the NV's brighter and darker spin states that occurs at high magnetic fields [77], those NVs within the field-free point fluoresce brightest and can thus be distinguished from other NVs. However, this approach would significantly degrade the spatial resolution due to the high fields required, and it is not easily amenable to modulation schemes.

As suggested by the potential sensitivity increases of nanodiamond imaging compiled in Table 5.1, there is ample room for improvement of the technique. The primary challenges to achieving these sensitivity improvements are experimental,

and work must be done to either achieve the stated sensitivity improvements or demonstrate what the currently unknown limiting factors are.

References

[1] G. Balasubramanian, I. Y. Chan, R. Kolesov, M. Al-Hmoud, J. Tisler, C. Shin, C. Kim, A. Wojcik, P. R. Hemmer, A. Krueger, T. Hanke, A. Leitenstorfer, R. Bratschitsch, F. Jelezko, and J. Wrachtrup, "Nanoscale imaging magnetometry with diamond spins under ambient conditions.," *Nature*, vol. 455, no. 7213, pp. 648–51, Oct. 2008.

[2] J. R. Maze, P. L. Stanwix, J. S. Hodges, S. Hong, J. M. Taylor, P. Cappellaro, L. Jiang, M. V. G. Dutt, E. Togan, A. S. Zibrov, A. Yacoby, R. L. Walsworth, and M. D. Lukin, "Nanoscale magnetic sensing with an individual electronic spin in diamond.," *Nature*, vol. 455, no. 7213, pp. 644–7, Oct. 2008.

[3] M. L. James and S. S. Gambhir, "A molecular imaging primer: modalities, imaging agents, and applications.," *Physiological reviews*, vol. 92, no. 2, pp. 897–965, Apr. 2012.

[4] T. Ji, A. Mpande, M. C. Muenker, S. Orton, D. Vizard, G. Feke, K. Medeiros, S. Chiang, V. Jacobs, W. McLaughlin, and W. M. Leevy, "A Novel, Near Infrared, Long Stoke's Shift Dye For Applications Ranging From Gels, To Cells, To Living Mice," *Biocompare*, 2009. [Online]. Available: http://www.biocompare.com/Application-Notes/43126-A-Novel-Near-Infrared-Long-Stoke-s-Shift-Dye-For-Applications-Ranging-From-Gels-To-Cells-To-Living-Mice/. [Accessed: 22-Feb-2013].

[5] G. Pratx, C. M. Carpenter, C. Sun, and L. Xing, "X-ray luminescence computed tomography via selective excitation: a feasibility study.," *IEEE transactions on medical imaging*, vol. 29, no. 12, pp. 1992–9, Dec. 2010.

[6] D. Budker, "Diamond nanosensors: The sense of colour centres," *Nature Physics*, vol. 7, no. 6, pp. 453–454, Apr. 2011.

[7] D. D. Awschalom, R. Epstein, and R. Hanson, "The diamond age of spintronics.," *Scientific American*, vol. 297, no. 4, pp. 84–91, Oct. 2007.

[8] I. Aharonovich, A. D. Greentree, and S. Prawer, "Diamond photonics," *Nature Photonics*, vol. 5, no. 7, pp. 397–405, Jun. 2011.

[9] A. Schrand, S. A. C. Hens, and O. Shenderova, "Nanodiamond Particles: Properties and Perspectives for Bioapplications," *Critical Reviews in Solid State and Materials Sciences*, vol. 34, no. 1, pp. 18–74, Jan. 2009.

[10] E. K. Chow, X.-Q. Zhang, M. Chen, R. Lam, E. Robinson, H. Huang, D. Schaffer, E. Osawa, A. Goga, and D. Ho, "Nanodiamond therapeutic delivery agents mediate enhanced chemoresistant tumor treatment.," *Science translational medicine*, vol. 3, no. 73, p. 73ra21, Mar. 2011.

[11] X.-Q. Zhang, R. Lam, X. Xu, E. K. Chow, H.-J. Kim, and D. Ho, "Multimodal nanodiamond drug delivery carriers for selective targeting, imaging, and enhanced chemotherapeutic efficacy.," *Advanced materials (Deerfield Beach, Fla.)*, vol. 23, no. 41, pp. 4770–5, Nov. 2011.

[12] J.-I. Chao, E. Perevedentseva, P.-H. Chung, K.-K. Liu, C.-Y. Cheng, C.-C. Chang, and C.-L. Cheng, "Nanometer-sized diamond particle as a probe for biolabeling.," *Biophysical journal*, vol. 93, no. 6, pp. 2199–208, Sep. 2007.

[13] V. Vaijayanthimala, P.-Y. Cheng, S.-H. Yeh, K.-K. Liu, C.-H. Hsiao, J.-I. Chao, and H.-C. Chang, "The long-term stability and biocompatibility of fluorescent nanodiamond as an in vivo contrast agent.," *Biomaterials*, vol. 33, no. 31, pp. 7802–7794, Aug. 2012.

[14] C.-C. Fu, H.-Y. Lee, K. Chen, T.-S. Lim, H.-Y. Wu, P.-K. Lin, P.-K. Wei, P.-H. Tsao, H.-C. Chang, and W. Fann, "Characterization and application of single fluorescent nanodiamonds as cellular biomarkers.," *Proceedings of the National Academy of Sciences of the United States of America*, vol. 104, no. 3, pp. 727–32, Jan. 2007.

[15] V. Tuchin, *Tissue Optics: Light Scattering Methods and Instruments for Medical Diagnosis*, 1st ed. SPIE Publications, 2000, p. 9.

[16] O. Faklaris, D. Garrot, V. Joshi, F. Druon, J.-P. Boudou, T. Sauvage, P. Georges, P. A. Curmi, and F. Treussart, "Detection of single photoluminescent diamond nanoparticles in cells and study of the internalization pathway.," *Small (Weinheim an der Bergstrasse, Germany)*, vol. 4, no. 12, pp. 2236–9, Dec. 2008.

[17] Y.-R. Chang, H.-Y. Lee, K. Chen, C.-C. Chang, D.-S. Tsai, C.-C. Fu, T.-S. Lim, Y.-K. Tzeng, C.-Y. Fang, C.-C. Han, H.-C. Chang, and W. Fann, "Mass production and dynamic imaging of fluorescent nanodiamonds.," *Nature nanotechnology*, vol. 3, no. 5, pp. 284–8, May 2008.

[18] R. Weissleder, "A clearer vision for in vivo imaging.," *Nature biotechnology*, vol. 19, no. 4, pp. 316–7, Apr. 2001.

[19] V. M. Acosta, D. Budker, P. R. Hemmer, J. R. Maze, and R. L. Walsworth, "Optical magnetometry with nitrogen-vacancy centers in diamond (Supplement)," in

Optical Magnetometry, D. Budker and D. F. Jackson Kimball, Eds. Cambridge University Press, 2013.

[20] P. G. Baranov, A. A. Soltamova, D. O. Tolmachev, N. G. Romanov, R. A. Babunts, F. M. Shakhov, S. V Kidalov, A. Y. Vul', G. V Mamin, S. B. Orlinskii, and N. I. Silkin, "Enormously high concentrations of fluorescent nitrogen-vacancy centers fabricated by sintering of detonation nanodiamonds.," *Small (Weinheim an der Bergstrasse, Germany)*, vol. 7, no. 11, pp. 1533–7, Jun. 2011.

[21] P. Kok and B. W. Lovett, "Materials science: qubits in the pink.," *Nature*, vol. 444, no. 7115, p. 49, Nov. 2006.

[22] T. D. Ladd, F. Jelezko, R. Laflamme, Y. Nakamura, C. Monroe, and J. L. O'Brien, "Quantum computers.," *Nature*, vol. 464, no. 7285, pp. 45–53, Mar. 2010.

[23] M. S. Grinolds, S. Hong, P. Maletinsky, L. Luan, M. D. Lukin, R. L. Walsworth, and A. Yacoby, "Nanoscale magnetic imaging of a single electron spin under ambient conditions," p. 12, Sep. 2012.

[24] C. Shin, C. Kim, R. Kolesov, G. Balasubramanian, F. Jelezko, J. Wrachtrup, and P. R. Hemmer, "Sub-optical resolution of single spins using magnetic resonance imaging at room temperature in diamond," *Journal of Luminescence*, vol. 130, no. 9, pp. 1635–1645, Sep. 2010.

[25] L. P. McGuinness, Y. Yan, A. Stacey, D. A. Simpson, L. T. Hall, D. Maclaurin, S. Prawer, P. Mulvaney, J. Wrachtrup, F. Caruso, R. E. Scholten, and L. C. L. Hollenberg, "Quantum measurement and orientation tracking of fluorescent nanodiamonds inside living cells.," *Nature nanotechnology*, vol. 6, no. 6, pp. 358–63, Jun. 2011.

[26] V. R. Horowitz, B. J. Alemán, D. J. Christle, A. N. Cleland, and D. D. Awschalom, "Electron spin resonance of nitrogen-vacancy centers in optically trapped nanodiamonds.," *Proceedings of the National Academy of Sciences of the United States of America*, vol. 109, no. 34, pp. 13493–7, Aug. 2012.

[27] L. T. Hall, C. D. Hill, J. H. Cole, B. Städler, F. Caruso, P. Mulvaney, J. Wrachtrup, and L. C. L. Hollenberg, "Monitoring ion-channel function in real time through quantum decoherence.," *Proceedings of the National Academy of Sciences of the United States of America*, vol. 107, no. 44, pp. 18777–82, Nov. 2010.

[28] S. Steinert, F. Ziem, L. Hall, A. Zappe, M. Schweikert, A. Aird, G. Balasubramanian, L. Hollenberg, and J. Wrachtrup, "Magnetic spin imaging under ambient conditions with sub-cellular resolution," p. 11, Nov. 2012.

[29] L. M. Pham, D. Le Sage, P. L. Stanwix, T. K. Yeung, D. Glenn, A. Trifonov, P. Cappellaro, P. R. Hemmer, M. D. Lukin, H. Park, A. Yacoby, and R. L. Walsworth, "Magnetic field imaging with nitrogen-vacancy ensembles," *New Journal of Physics*, vol. 13, no. 4, p. 045021, Apr. 2011.

[30] L. T. Hall, G. C. G. Beart, E. A. Thomas, D. A. Simpson, L. P. McGuinness, J. H. Cole, J. H. Manton, R. E. Scholten, F. Jelezko, J. Wrachtrup, S. Petrou, and L. C. L. Hollenberg, "High spatial and temporal resolution wide-field imaging of neuron activity using quantum NV-diamond.," *Scientific reports*, vol. 2, p. 401, Jan. 2012.

[31] R. Igarashi, Y. Yoshinari, H. Yokota, T. Sugi, F. Sugihara, K. Ikeda, H. Sumiya, S. Tsuji, I. Mori, H. Tochio, Y. Harada, and M. Shirakawa, "Real-time background-free selective imaging of fluorescent nanodiamonds in vivo.," *Nano letters*, vol. 12, no. 11, pp. 5726–32, Nov. 2012.

[32] N. Yang and A. E. Cohen, "Optical imaging through scattering media via magnetically modulated fluorescence," *Optics Express*, vol. 18, no. 25, p. 25461, Nov. 2010.

[33] A. Hegyi and E. Yablonovitch, "Molecular Imaging by Optically Detected Electron Spin Resonance of Nitrogen-Vacancies in Nanodiamonds.," *Nano letters*, vol. 13, no. 3, pp. 1173–1178, Feb. 2013.

[34] J. R. Maze, A. Gali, E. Togan, Y. Chu, A. Trifonov, E. Kaxiras, and M. D. Lukin, "Properties of nitrogen-vacancy centers in diamond: the group theoretic approach," *New Journal of Physics*, vol. 13, no. 2, p. 025025, Feb. 2011.

[35] M. W. Doherty, N. B. Manson, P. Delaney, and L. C. L. Hollenberg, "The negatively charged nitrogen-vacancy centre in diamond: the electronic solution," *New Journal of Physics*, vol. 13, no. 2, p. 025019, Feb. 2011.

[36] D. M. Bishop, *Group Theory and Chemistry (Dover Books on Chemistry)*. Dover Publications, 1993, p. 336.

[37] "Diamond Crystallography." [Online]. Available: http://www.e6cvd.com/cvd/page.jsp?pageid=361. [Accessed: 05-Oct-2012].

[38] D. J. Griffiths, *Introduction to Quantum Mechanics (2nd Edition)*. Addison-Wesley, 2004, p. 480.

[39] N. Manson, J. Harrison, and M. Sellars, "Nitrogen-vacancy center in diamond: Model of the electronic structure and associated dynamics," *Physical Review B*, vol. 74, no. 10, Sep. 2006.

[40] N. B. Manson, L. Rogers, and M. W. Doherty, “Optically induced spin polarisation of the NV − centre in diamond: role of electron-vibration interaction,” *Laser Physics*, pp. 1–8, 2010.

[41] Y. Dumeige, M. Chipaux, V. Jacques, F. Treussart, J.-F. Roch, T. Debuisschert, V. M. Acosta, A. Jarmola, K. Jensen, P. Kehayias, and D. Budker, “Magnetometry with nitrogen-vacancy ensembles in diamond based on infrared absorption in a doubly resonant optical cavity,” *Physical Review B*, vol. 87, no. 15, p. 155202, Apr. 2013.

[42] C. Kittel, *Introduction to Solid State Physics*, 8th ed. Hoboken, NJ: John Wiley & Sons, Inc., 2005.

[43] “Dielectric and Magnetic properties of materials,” 2008. [Online]. Available: http://vtuphysics.blogspot.com/2008/07/unit-4.html. [Accessed: 01-Oct-2012].

[44] R. Chapman and T. Plakhotnik, “Quantitative luminescence microscopy on Nitrogen-Vacancy Centres in diamond: Saturation effects under pulsed excitation,” *Chemical Physics Letters*, vol. 507, no. 1–3, pp. 190–194, Apr. 2011.

[45] D. Redman, S. Brown, R. Sands, and S. Rand, “Spin dynamics and electronic states of N-V centers in diamond by EPR and four-wave-mixing spectroscopy,” *Physical Review Letters*, vol. 67, no. 24, pp. 3420–3423, Dec. 1991.

[46] L. Robledo, H. Bernien, T. van der Sar, and R. Hanson, “Spin dynamics in the optical cycle of single nitrogen-vacancy centres in diamond,” *New Journal of Physics*, vol. 13, no. 2, p. 025013, Feb. 2011.

[47] C. L. Degen, M. Poggio, H. J. Mamin, C. T. Rettner, and D. Rugar, “Nanoscale magnetic resonance imaging.,” *Proceedings of the National Academy of Sciences of the United States of America*, vol. 106, no. 5, pp. 1313–7, Feb. 2009.

[48] P. Glover and S. P. Mansfield, “Limits to magnetic resonance microscopy,” *Reports on Progress in Physics*, vol. 65, no. 10, pp. 1489–1511, Oct. 2002.

[49] A. Gruber, “Scanning Confocal Optical Microscopy and Magnetic Resonance on Single Defect Centers,” *Science*, vol. 276, no. 5321, pp. 2012–2014, Jun. 1997.

[50] D. G. Nishimura, *Principles of Magnetic Resonance Imaging*. Stanford, CA: Dwight G. Nishimura, 2010.

[51] A. Yariv, *Quantum Electronics*. Wiley, 1989, p. 676.

[52] "EasySpin: The Spin Hamiltonian." [Online]. Available: http://www.easyspin.org/documentation/hamiltonian.html. [Accessed: 31-Oct-2012].

[53] E. Yablonovitch, "EE 236a Class Notes." University of California, Berkeley.

[54] P. W. Goodwill and S. M. Conolly, "The X-space formulation of the magnetic particle imaging process: 1-D signal, resolution, bandwidth, SNR, SAR, and magnetostimulation.," *IEEE transactions on medical imaging*, vol. 29, no. 11, pp. 1851–9, Nov. 2010.

[55] J. D. Jackson, *Classical Electrodynamics Third Edition*. Wiley, 1998, p. 808.

[56] P. C. D. Hobbs, "Ultrasensitive laser measurements without tears," *Applied Optics*, vol. 36, no. 4, p. 903, Feb. 1997.

[57] C.-Y. Fang, V. Vaijayanthimala, C.-A. Cheng, S.-H. Yeh, C.-F. Chang, C.-L. Li, and H.-C. Chang, "The exocytosis of fluorescent nanodiamond and its use as a long-term cell tracker.," *Small (Weinheim an der Bergstrasse, Germany)*, vol. 7, no. 23, pp. 3363–70, Dec. 2011.

[58] C. Vonesch, R. T. Cristofani, and G. Schmit, "DeconvolutionLab." Biomedical Image Group, École Polytechnique Fédérale de Lausanne, 2009.

[59] J. E. Dahl, R. M. Carlson, S. Liu, and W. Bokhari, "Luminescent heterodiamondoids as biological labels," U.S. Patent US 2005/0019955 A12005.

[60] C. . Hardy, W. . Edelstein, and D. Vatis, "Efficient adiabatic fast passage for NMR population inversion in the presence of radiofrequency field inhomogeneity and frequency offsets," *Journal of Magnetic Resonance (1969)*, vol. 66, no. 3, pp. 470–482, Feb. 1986.

[61] E. Yablonovitch, "Statistical ray optics," *Journal of the Optical Society of America*, vol. 72, no. 7, p. 899, Jul. 1982.

[62] F. P. Bolin, L. E. Preuss, R. C. Taylor, and R. J. Ference, "Refractive index of some mammalian tissues using a fiber optic cladding method.," *Applied optics*, vol. 28, no. 12, pp. 2297–303, Jun. 1989.

[63] H. Key, E. R. Davies, P. C. Jackson, and P. N. Wells, "Optical attenuation characteristics of breast tissues at visible and near-infrared wavelengths.," *Physics in medicine and biology*, vol. 36, no. 5, pp. 579–90, May 1991.

[64] B. B. Das, F. Liu, and R. R. Alfano, “Time-resolved fluorescence and photon migration studies in biomedical and model random media,” *Reports on Progress in Physics*, vol. 60, no. 2, pp. 227–292, Feb. 1997.

[65] “Guidelines on limits of exposure to broad-band incoherent optical radiation (0.38 to 3 microM). International Commission on Non-Ionizing Radiation Protection.,” *Health physics*, vol. 73, no. 3, pp. 539–54, Sep. 1997.

[66] IEC, “IEC 60825-1 Safety of laser products - Part 1: Equipment classification and requirements.” .

[67] “Dielectric Properties of Body Tissues in the frequency range 10 Hz - 100 GHz.” [Online]. Available: http://niremf.ifac.cnr.it/tissprop/htmlclie/htmlclie.htm.

[68] “Evaluating Compliance with FCC Guidelines for Human Exposure to Radiofrequency Electromagnetic Fields (OET Bulletin 65).” Federal Communications Commission Office of Engineering & Technology, 1997.

[69] C. S. Levin, “Primer on molecular imaging technology.,” *European journal of nuclear medicine and molecular imaging*, vol. 32 Suppl 2, pp. S325–45, Dec. 2005.

[70] D. Sosnovik and R. Weissleder, “Magnetic resonance and fluorescence based molecular imaging technologies,” in *Imaging in Drug Discovery and Early Clinical Trials*, vol. 62, P. L. Herrling, A. Matter, and M. Rudin, Eds. Basel: Birkhäuser-Verlag, 2005, pp. 83–115.

[71] M. A. Hahn, A. K. Singh, P. Sharma, S. C. Brown, and B. M. Moudgil, “Nanoparticles as contrast agents for in-vivo bioimaging: current status and future perspectives.,” *Analytical and bioanalytical chemistry*, vol. 399, no. 1, pp. 3–27, Jan. 2011.

[72] T. Knopp, S. Biederer, T. F. Sattel, M. Erbe, and T. M. Buzug, “Prediction of the spatial resolution of magnetic particle imaging using the modulation transfer function of the imaging process.,” *IEEE transactions on medical imaging*, vol. 30, no. 6, pp. 1284–92, Jun. 2011.

[73] R. A. de Kemp, F. H. Epstein, C. Catana, B. M. W. Tsui, and E. L. Ritman, “Small-animal molecular imaging methods.,” *Journal of nuclear medicine : official publication, Society of Nuclear Medicine*, vol. 51 Suppl 1, no. Supplement_1, p. 18S–32S, May 2010.

[74] S. R. Meikle, P. Kench, M. Kassiou, and R. B. Banati, “Small animal SPECT and its place in the matrix of molecular imaging technologies.,” *Physics in medicine and biology*, vol. 50, no. 22, pp. R45–61, Nov. 2005.

[75] M. Patlak, “Nanoimaging devices illuminate tumor margins during surgery.,” *Journal of the National Cancer Institute*, vol. 103, no. 3, pp. 173–4, Feb. 2011.

[76] J. Bonnema and C. J. H. van de Velde, “Sentinel lymph node biopsy in breast cancer,” *Annals of Oncology*, vol. 13, no. 10, pp. 1531–1537, Oct. 2002.

[77] J.-P. Tetienne, L. Rondin, P. Spinicelli, M. Chipaux, T. Debuisschert, J.-F. Roch, and V. Jacques, “Magnetic-field-dependent photodynamics of single NV defects in diamond: Application to qualitative all-optical magnetic imaging,” Jun. 2012.